Theses and Dissertations

4-30-2011

Fatigue and fracture testing and analysis on four engineering materials

Brett Martin Ziegler

Follow this and additional works at: https://scholarsjunction.msstate.edu/td

FATIGUE AND FRACTURE TESTING AND ANALYSIS

ON FOUR ENGINEERING MATERIALS

By

Brett Martin Ziegler

A Dissertation
Submitted to the Faculty of
Mississippi State University
in Partial Fulfillment of the Requirements
for the Degree of Doctor of Philosophy
in Aerospace Engineering
in the Department of Aerospace Engineering

Mississippi State, Mississippi

April 2011

FATIGUE AND FRACTURE TESTING AND ANALYSIS

ON FOUR ENGINEERING MATERIALS

By

Brett Martin Ziegler

Approved:

_____
James C. Newman, Jr.
Professor of Aerospace Engineering
(Major Professor)

_____
Steven R. Daniewicz
Professor and Interim Department Head
of Mechanical Engineering
(Committee Member)

_____
Thomas E. Lacy
Associate Professor of Aerospace
Engineering
(Committee Member)

_____
Rani W. Sullivan
Assistant Professor of Aerospace
Engineering
(Committee Member)

_____
J. Mark Janus
Associate Professor and Graduate
Coordinator of Aerospace Engineering

_____
Sarah A. Rajala
Dean of the James Worth Bagley College
of Engineering

Name: Brett Martin Ziegler

Date of Degree: April 30, 2011

Institution: Mississippi State University

Major Field: Aerospace Engineering

Major Professor: James C. Newman, Jr.

Title of Study: FATIGUE AND FRACTURE TESTING AND ANALYSIS ON FOUR
ENGINEERING MATERIALS

Pages in Study: 120

Candidate for Degree of Doctor of Philosophy

Fatigue and fracture testing and analyses were performed on four engineering materials: a low-strength aluminum alloy (D16CzATWH), a high-strength aluminum alloy (Al7050-T7351), a low-strength steel (A36 steel), and a high-strength steel (9310 steel). Large-crack testing included compression precracked constant amplitude and compression precracked load reduction over a wide range of stress ratios. Single- and multiple-spike overload tests were conducted on some of the materials. Fatigue and small-crack testing were also performed at constant amplitude loading at a constant load ratio on the newly designed single edge notch bend specimen. Using the FADD2D boundary element code, two-dimensional stress analysis was performed on the new specimen to determine the stress intensity factor as a function of crack size for surface and through cracks at the edge notch. Collected fatigue crack growth rate data was used to develop a material model for the FASTRAN strip-yield crack growth code. FASTRAN was used to simulate the constant amplitude and spike overload tests, as well as the small-crack fatigue tests.

The fatigue crack growth simulation results have shown that both low-cycle and high-cycle fatigue can be modeled accurately as fatigue crack growth using FASTRAN and that FASTRAN can be used to accurately predict the acceleration and retardation in fatigue crack growth rates after a spike overload. The testing has shown that the starting fatigue crack growth rate of any load-shedding test has significant influence on load history effects, with lower starting rates yielding lower crack growth thresholds and faster rates. Through inspection of fatigue surfaces, it has been shown that beveling of pin-holes in the crack growth specimens is necessary to ensure symmetric crack fronts and that the presence of debris along the fatigue surfaces can cause considerable crack growth retardation.

DEDICATION

To Jen, Mom, and Dad

ACKNOWLEDGMENTS

TABLE OF CONTENTS

LIST OF TABLES

LIST OF FIGURES

NOMENCLATURE

a	Crack depth in thickness direction for surface cracks
B	Specimen sheet thickness
c	Crack length in width direction for C(T) and ESE(T) specimens, half crack length for M(T) specimens
$CPCA$	Compression precracked constant amplitude loading
$CPLR$	Compression precracked load reduction
$C(T)$	Compact specimen
$\frac{da}{dN}, \frac{dc}{dN}$	Fatigue crack growth rate in a- and c-directions
E	Modulus of elasticity
$EIFS$	Equivalent initial flaw size
$ESE(T)$	Eccentrically loaded, single-edge-notch tension specimen
F	Boundary correction factor, corrects infinite plate solution for finite width geometry
K	Stress-intensity factor
K_{cp}	Compressive stress-intensity factor during precracking
K_F	Elastic-plastic fracture toughness
K_{Ic}	Plane strain fracture toughness
K_{Ie}	Elastic fracture toughness or maximum stress-intensity factor at failure
K_{max}	Stress-intensity factor at maximum applied cyclic load
K_T	Stress concentration factor
m	Configuration and material fracture parameter
$M(T)$	Middle-crack tension specimen
P_{max}	Maximum applied cyclic load
P_{min}	Minimum applied cyclic load
P_o	Crack-opening load

R	Load ratio $\left(\frac{P_{min}}{P_{max}}\right)$
$SEN(B)$	Single edge notch bend specimen
$SEN(T)$	Single edge notch tension specimen
t	Half sheet thickness for surface crack at edge notch
U	Crack-opening function, $(1 - \frac{P_o}{P_{max}})/(1 - R)$
w	Width of specimen for C(T), ESE(T), and SEN(B), half width for M(T)
α	Constraint factor
ΔK	Stress intensity factor range between maximum and minimum cyclic loads
ΔK_{th}	Threshold stress intensity factor range
ΔK_{eff}	Effective stress intensity factor range
$(\Delta K_{eff})_T$	Effective stress intensity factor range at transition from flat to slant crack growth
ρ_{cp}	Compressive plastic zone size
σ_o	Flow stress (average of σ_{ys} and σ_u)
σ_{ys}	Yield stress (0.2% offset)
σ_u	Ultimate tensile strength

CHAPTER 1

INTRODUCTION

It is of vital importance, when designing and analyzing metallic structures, to accurately predict the effects of fatigue and fracture on structural life. Making accurate structural life predictions requires access to accurate, consistent fatigue crack growth data sets collected over a large range in crack growth rates from threshold (10^{-10} m/cycle) to fracture. To ensure uniformity of crack growth testing practices, standards have been developed by members of the engineering community (American Society of Testing and Measures, ASTM). Unfortunately, it has been shown during the past few years that some of these standards produce incorrect, albeit consistent, results. For example, the present practice of using load shedding to generate fatigue-crack-growth-rate data (dc/dN where c is crack length and N is the number of applied loading cycles) in laboratory crack growth specimens, has produced "fanning," an increase in the threshold effective stress intensity range for tests performed at a lower load ratio ($R = P_{min}/P_{max}$), in the near-threshold and threshold regimes. It is the intent of this work to show the benefits of certain testing and preparation techniques, such as compression precracking and pin-hole beveling, that should be used to maximize data quality. Moreover, this work will demonstrate the usefulness of the FASTRAN strip-yield code to accurately simulate fatigue and crack growth test results when a proper material model has been developed.

Fatigue and fracture tests were performed for small cracks in 7050 aluminum alloy and 9310 steel and for large-cracks in D16Cz aluminum alloy, 7050 aluminum alloy, 9310 steel and A36 steel. Small-crack fatigue tests included specimens containing only naturally initiated cracks. Constant amplitude (CA) large-crack tests with crack-growth rate data ranging from threshold to fracture were performed for multiple load ratios (R). Large-crack fatigue crack growth testing also consisted of some spike overload (OL) tests. Stress intensity range (ΔK) and fatigue crack growth rate (dc/dN) data gathered through these tests were used to determine the material properties necessary for modeling crack growth and failure with the FASTRAN life prediction code.

1.1 Fracture Mechanics

Historically, the study of fracture mechanics in metals has been performed in one of two regimes: linear elastic and non-linear [1]. The former is an effective approach for very brittle materials and does not account for plastic flow at the crack tip. The latter is far more complicated, but does account for plastic flow, more accurately simulating ductile fracture.

1.1.1 Linear Elastic Fracture Mechanics

When considering the history of Fracture Mechanics, credit must first be given to Inglis [2] for his work on the effects of holes and sharp corners on stresses in plates in 1913. Inglis presented how an irregular hole (like an elliptical or square hole) in an infinite plate under constant applied stress has a stress concentration at the edge of the

2

hole inversely proportional to the radius of curvature of the hole; for an elliptical hole, the stress concentration is related to the ratio of the semi-minor and semi-major axes. By considering the limit as the semi-minor axis of an ellipse approaches zero, the Inglis solution can be applied to a mathematical crack, i.e., a notch with zero radius of curvature. In 1920 Griffith [3], using the work of Inglis, determined that a flaw in any solid becomes unstable when the change in strain energy for an incremental increase in crack surface area exceeds the free surface energy of the material. With this model, Griffith accurately predicted relationships between failure stress and flaw size in glass specimens; however, the method proved successful for predicting the fracture of brittle solids only. Almost 30 years passed before Griffith's model was modified for successful application to metals.

In the decade following World War II, a group of researchers at the Naval Research Laboratory studied the catastrophic fracture of many Liberty Ships (a result of changing from riveted hulls to welded hulls) [1]. The leader of the fracture mechanics research group, Irwin [4], added an energy dissipation term to the Griffith model to account for plastic flow making the Griffith model applicable to metals . Using a semi-inverse method for sharp crack analysis developed by Westergaard [5] in 1938, Irwin [6] determined that the stresses and displacements near the crack tip could be described by a single parameter related to the energy release rate in 1957. This parameter is called the stress-intensity factor (K) and is the constant from the first-order Taylor series expansion of the stress field at a crack tip. In the same year, Williams [7] completed the same first-order expansion independent of Irwin.

In 1954, Wells [8] determined that square windows and inadequate reinforcement were the cause of two Comet jet aircraft fuselage failures. Winne and Wundt [9] applied Irwin's energy release method to predict the failure of large steam turbine rotors in 1957. However, because linear elastic fracture mechanics (LEFM) is accurate only for cases of limited plastic deformation, predicting the fracture of engineering metallic materials required more accurate methods.

1.1.2 Non-Linear Fracture Mechanics

By 1960, researchers in the field of linear elastic fracture mechanics began to focus on crack tip plasticity. Irwin [10] developed a plastic zone correction factor; and Dugdale [11] and Barenblatt [12] developed more elaborate models based on the yielding of narrow strips of material at the crack-tip. Wells [13] suggested that crack face displacement could be a criterion for predicting fracture. According to Anderson, "When Wells returned to his post at the British Welding Research Association, he attempted to apply LEFM to low- and medium-strength structural steels. These materials were too ductile for LEFM to apply, but Wells noticed that the crack faces moved apart with plastic deformation. This observation led to the development of the parameter now known as the crack-tip-opening displacement (CTOD)" [1]. In 1968, Rice [14] used idealized plastic deformation to determine a new parameter to characterize nonlinear fracture behavior. This parameter was calculated using a line integral evaluated along an arbitrary contour around a crack and called the J-integral. He was able show that the J-integral was equal to the strain energy release rate for linear-elastic behavior. In the same year, Hutchinson [15] and

Rice and Rosengren [16] showed a relationship between the J-integral and the crack-tip stresses in nonlinear elastic materials — proving that the J-integral is a nonlinear corollary to the stress-intensity factor. Shih and Hutchinson [17] provided a mathematical relationship between material toughness, flaw size, and stress using the J-integral in 1976. Later, a fracture design handbook [18] was published by the Electric Power Research Institute based on the Shih and Hutchinson method. Other fracture handbooks have been written based on the methods proposed by Dugdale, Barenblatt, and Burdekin and Dawes (CTOD design curve) [19]. According to Anderson, "Current research tends to result in incremental advances rather than major gains. The application of this technology to practical problems is so pervasive that fracture mechanics is now considered an established engineering discipline" [1].

1.2 Fatigue

Early studies in fatigue were focused on predicting the premature failure of metal parts experiencing cyclic loads. Testing consisted of correlating the fatigue life of a part to different maximum fully-reversed cyclic loads and determining a fatigue limit, the stress level below which the part "never" fails. The approach to fatigue crack growth analysis is more focused on the growth of cracks and other imperfections. Fatigue crack growth testing finds a correlation between the applied stress intensity factor range and the crack growth rate.

1.2.1 Early Fatigue Mechanics

The study of metal fatigue began with an investigation into why railroad axles were failing at loads well below predicted failure loads in the 1840's [20]. According to Stephens et al., "Even then, the elimination of sharp corners was recommended. The word 'fatigue' was introduced in the late 1840's to describe failures occurring from repeated stresses" [21]. In the 1860's, August Wohler performed many rotating bending tests, now considered the first systematic fatigue testing, and developed the S-N table (diagram) and the concept of fatigue limit. Wohler also expressed that the range of stress had greater affect on fatigue life than maximum stress [22]. In the 1870's, Goodman worked on the effects of mean stress on fatigue life.

In 1886, Bauschinger [23] showed how a previous compressive load that caused yielding would alter the subsequent tensile yield stress; this was the first example of the effects of a single inelastic strain reversal on the stress-strain behavior of metals and a starting point for understanding cyclic hardening and softening. Ewing and Humfrey [24], using an optical microscope, documented slip lines, slip bands and the formation of microcracks in metals in the early 1900's. In 1910, Basquin [25] showed the log-log linearity of the S-N diagram. Gough and his associates study the effects of bending and torsion on metal fatigue in the 1920's. In 1924, he published a comprehensive book on the fatigue of metals [26]. The first comprehensive, American book on metal fatigue was published by Moore and Kommers [27] in 1927.

By 1920, Haigh [28] had offered his explanation for the differing responses of fatigue notches in high-strength and mild steel alloys. His explanation included observations of notch strain and the effects of residual stresses that would be later studied by others. The automobile industry adopted shot-peening as a standard practice during the 1930's leading to a marked reduction in the all-too-common failure of metal springs and axles. Work continued on manufacturing practices that would yield compressive residual stresses including Almen [29] and Horger [30], who discussed the advantages of surface rolling in metals.

According to Stephens et al., "During World War II the deliberate use of compressive residual stresses became common in the design of aircraft engines and armored vehicles" [21]. Most metal failures resulted from sharp corners in hatches, cutouts, and welds. By reinforcing holes, rounding corners, and adding riveted joints, most of these failures could be avoided. In 1945, Miner [31] developed the linear cumulative damage criterion, which Palmgren had suggested in 1924. Since then, the Palmgren-Miner linear damage rule has been used extensively in fatigue design and analysis. In 1946, the American Society for Testing and Materials (ASTM) formed the E-09 committee, providing a forum for standards and research in the field of fatigue. The first chairman of E-09 was Peterson [32], who emphasized the fatigue notch factor which accounts for stress concentration factor, the notch, geometry, and the ultimate stress of the material . Peterson published a book of stress concentration factors [33] in 1953 and an expanded version of the same [34] in 1974.

In January 1954, disaster struck when a Comet aircraft (the first jet-propelled passenger plane) crashed into the Mediterranean Sea as a result of a fatigue failure of the pressurized cabin [21]. Although the Comet had been fatigue tested extensively, the testing sequences had begun with loads larger than standard operating loads, resulting in residual stresses that improved the fatigue life of the tested fuselage. All Comet aircraft of this type were removed from service and a new emphasis was placed on attention to maintenance and inspection between flights, a fail-safe approach replaced the common safe-life strategy [21]. The 1950's also saw the creation of the closed-loop servohydraulic test system, allowing for better simulation of realistic load sequences. Irwin's [6] contribution to LEFM during the 1950's would eventually become a staple of the fatigue culture, and the development of the Weibull distribution [35] provided a multi-parameter, probabilistic approach to fatigue life testing.

1.2.2 Modern Fatigue Mechanics

Paris, Gomez, and Anderson [36], in 1961, described the log-log relationship between the fatigue crack growth rate (dc/dN) and the stress intensity factor range (ΔK), defined as the difference between maximum and minimum applied K, giving birth to modern fatigue crack growth mechanics. In 1967, Schijve [37] pointed out the importance of understanding the effects of variable-amplitude loading in predicting aircraft fatigue life. The Silver Bridge failure in Point Pleasant, West Virginia resulted from a cleavage fracture of a crack developed through fatigue and corrosion. According to Stephens et al., "This failure had a profound influence on subsequent design requirements established by

the American Association of State and Highway and Transportation Officials (AASHTO)" [21]. Meanwhile, failures due to brittle fractures in the F-111 aircraft and other U.S. Air Force vehicles influenced the fracture mechanics concepts required in designing the B-1 Bomber in the 1970's [21].

In 1970, Elber [38] demonstrated his fatigue crack closure principle and the importance of an effective stress-intensity factor (ΔK_{eff}) as an effective crack driving force for correlating fatigue crack growth rates. That year, Paris [39, 40] showed that there exists a stress-intensity range threshold below which a crack will not grow. During the 1970's, the U.S. Air Force issued Mil A-83444 defining damage tolerance standards for the design of military aircraft [21]. During the 1980's, it was discovered that small cracks grow more quickly than large cracks with the same driving force. The failure of an Aloha Airlines Boeing 737 in 1988 led to improved maintenance and nondestructive inspection [21]. The recent advances in computer technology have allowed for more full-scale simulation and less testing of individual parts; however, testing is still the only way to determine material properties.

1.3 Testing

All of the testing for this project was performed in the Fatigue and Fracture Laboratory in Walker Hall at Mississippi State University. Some fatigue and crack growth data was attained from the literature or directly from other authors. Tests in this facility were performed with closed-loop servo-hydraulic cyclic loading test frames. Testing was broken in two parts: small-crack testing and large-crack testing. Once any crack dimensions exceeds about 200 microns, the crack is considered a large crack.

1.3.1 Small-Crack Testing

Small-crack testing was performed using a single edge notch bending (SEN(B)) specimen, Figure 1.1(a). The 9310 steel small-crack specimens were chemically polished to remove residual stresses induced by machining. Because the electro-chemical polishing process resulted in undesirable surface irregularities on some of the steel specimens, the aluminum alloy specimens were not electro-chemically polished.

Instead, Al7050 SEN(B) specimens were mechanically polished as part of the machining process. Small-crack lengths along the bore of the notch were monitored with a high-power microscope to generate crack-length versus cycles data. Small-crack specimens were tested from naturally occurring cracks, which formed as a result of the material microstructure. Cycles to failure of each small-crack specimen was plotted against maximum notch stress to develop a stress life (S-N) curve for the high-strength materials.

1.3.2 Large-Crack Testing

The A36 steel large-crack testing was performed on eccentrically loaded single-edge-notch tension (ESE(T)) specimens (Fig. 1.1(b)). Large-crack testing on the D16Cz aluminum alloy, 7050 aluminum alloy and 9310 steel was performed with compact (C(T)) specimens (Fig. 1.1(c)). Before any tests were started, each specimen was polished to produce a mirror finish for optical crack length monitoring, which was performed regularly throughout the tests. Next, a strain gage was placed on the backface of each specimen, making it possible for the computer system to constantly monitor the crack length during mode I testing, see Figure 1.1(c). Every large-crack specimen was compression pre-cracked — cyclic compressive loads were applied to the specimen to initiate a crack at the machined notch. Because of compression precracking, all of the tests began with a sharp crack and not a notch. This cracked specimen was fatigued until a condition of stable crack growth had been achieved, generally two to three times the size of the compressive plastic zone, before the crack growth rate data was considered valid.
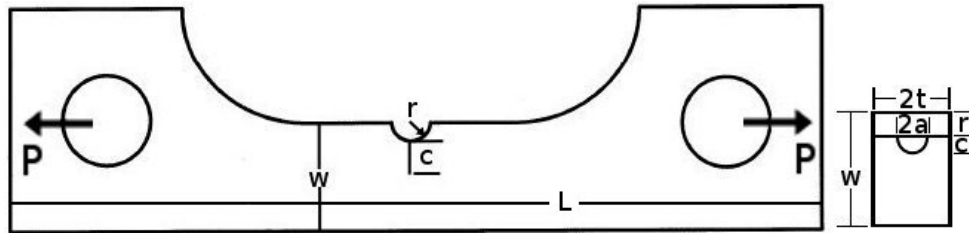
(a) SEN(B) small-crack test specimen
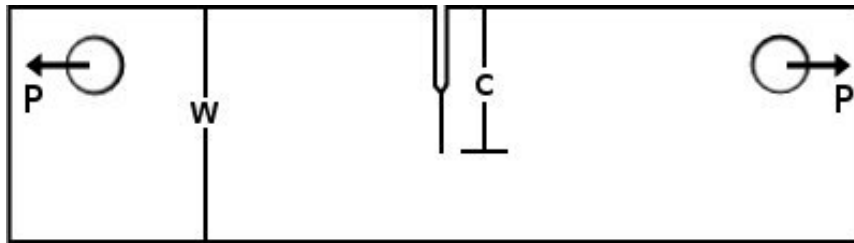
(b) ESE(T) specimen used for A36 steel testing
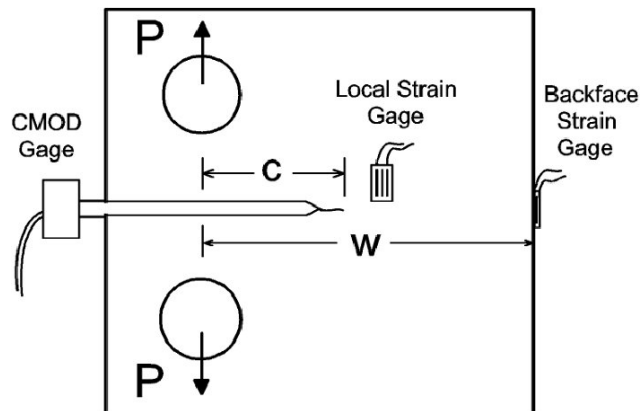
(c) C(T) specimen with CMOD, backface strain,
and local strain gages

Figure 1.1

Specimens used for testing at Mississippi State University

The large-crack testing regimen consisted of standard ASTM load-reduction [41], compression precracking constant amplitude (CPCA), compression precracking load reduction (CPLR), and spike overload (OL) tests. The first large-crack tests to be completed for each material was a CPLR test. CPLR tests are similar to the load reduction tests described by ASTM E-647 [41] with the exception that, because the specimen is compression precracked, load reduction begins at a much lower crack growth rate (dc/dN), resulting in data that has minimal influence associated with plastic (load) history effects. CPLR test data was used to identify a threshold stress-intensity factor range (ΔK_{th}) for beginning a CPCA test. Because ΔK is constantly increasing in a CPCA test, there is minimal influence of load history effects (increasing crack opening load found in load reduction tests) after the crack has grown about three compression plastic zone sizes. CPLR and CPCA fatigue crack growth rate data identifies a more accurate ΔK_{th} value and provided data for the threshold regime, the Paris regime (mid-region), and final fracture. Table 1.1 describes all the testing performed in the present work, including small- and large-crack tests.

Table 1.1

All tests performed as part of the present work

Material	Specimen	Type	Loading
D16Cz	C(T)	CPLR	$R = 0.75$
		CPLR	$R = 0.33$
		CPCA	$R = 0.33$
		CPLR	$R = 0.1$
		CPCA	$R = 0.1$
		Spike-OL	$R = 0.1$, OL=2
Al7050	C(T)	CPLR	$R = 0.1$
		CPLR	$R = 0.7$
		CPLR	$R = 0.9$
	SEN(B)	CA	9 @ $R = 0.1$
A36 Steel	ESE(T)	CPLR	$R = 0.7$
		CPCA	$R = 0.7$
		CPLR	$R = 0.1$
		CPCA	$R = 0.1, 0.7$
		CPCA	4 @ $R = 0.1$
9310 Steel	C(T)	CPLR	$R = 0.95$
		CPLR	$R = 0.9$
		CPLR	$R = 0.7$
		CPLR	$R = 0.5$
		CPLR	$R = 0.1$
		Spike-OL	$R = 0.1$, OL = 2, 2.5
	SEN(B)	CA	16 @ $R = 0.1$

1.3.3 Test Data from Literature

During testing of the D16 aluminum alloy, fatigue crack growth rate data was received from Schijve et al. [42]. This data was collected using the middle-crack tension specimen, M(T), which can be seen in Figure 1.2(a). In order to support the small-crack testing fatigue life data, fatigue data was taken from the the literature. Al7050 fatigue data was taken from *Metallic Materials Properties Development and Standardizations* (MMPDS) [43] and was collected using the open hole (K_T = 3.47) specimen, an M(T) specimen without a saw-cut notch. The 9310 steel fatigue data was taken from Liu et al. [44]. These data were collected using the single-edge notch tension (SEN(T)) specimen, which can be seen in Figure 1.2(b).
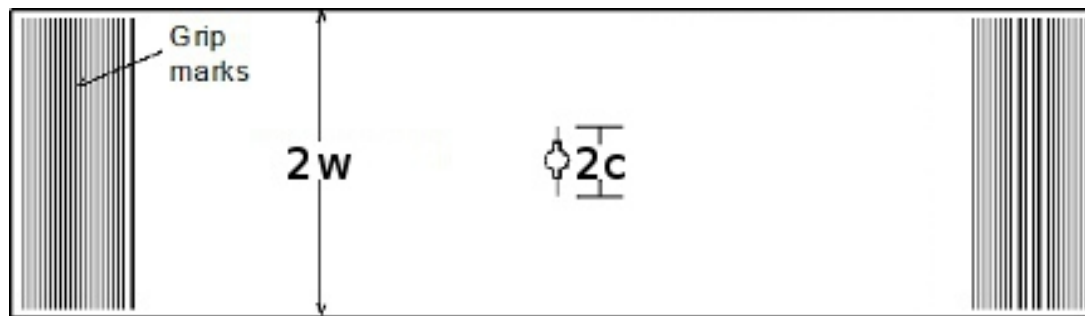
(a) M(T) specimen was used by Schijve et al [42]
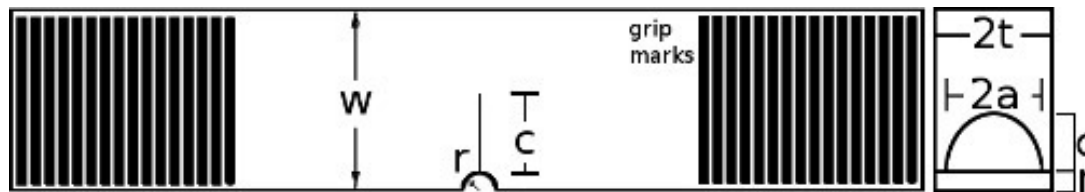
(b) SEN(T) specimen was used to collect data found in Liu et al. [44]

Figure 1.2

Data taken from other authors was gathered using these specimens

1.4 Analysis

The goal of most of the large-crack testing in this work was to generate enough fatigue crack growth data to predict the fatigue crack growth and fracture of structural components made of the same material. Fatigue crack growth analysis and predictions were made using FASTRAN 5.0, a two-dimensional fatigue crack growth simulation program written and maintained by Newman [45]. FASTRAN [45, 46, 47] uses a modified Dugdale [11] model along with modified equations for crack closure based on Elber's crack closure theory [38]. For fracture calculations, FASTRAN employs the Two Parameter Fracture Criterion (TPFC), also developed by Newman [48].

1.4.1 Fatigue Crack Growth

Constant amplitude data were used to determine a relationship between crack growth rate (dc/dN) and stress intensity factor range (ΔK) for each load ratio (R) from threshold to fracture, see Figure 1.3(a). Spike overload test results were used with CA data to determine the tensile constraint factor (α), which allows FASTRAN to account for the three-dimensional state-of-stress effects as a piecewise function of dc/dN. Compliance data gathered with the backface strain (BFS) gage were used to monitor crack lengths and to measure crack-opening loads. The final result, as seen in Figure 1.3(b), is a correlation between dc/dN and ΔK_{eff}. Crack closure analysis was performed on the data from multiple tests over a range of R to produce a unique correlation between effective crack driving force and crack growth rate that is nearly independent of R. A multi-linear (piecewise linear) curve was fit to the ΔK_{eff}-rate data. This relationship was used by FASTRAN

16

to simulate fatigue crack growth life for spike OL large-crack [49] and constant amplitude small-crack tests.

(a) Constant amplitude data   (b) Results of crack closure analysis
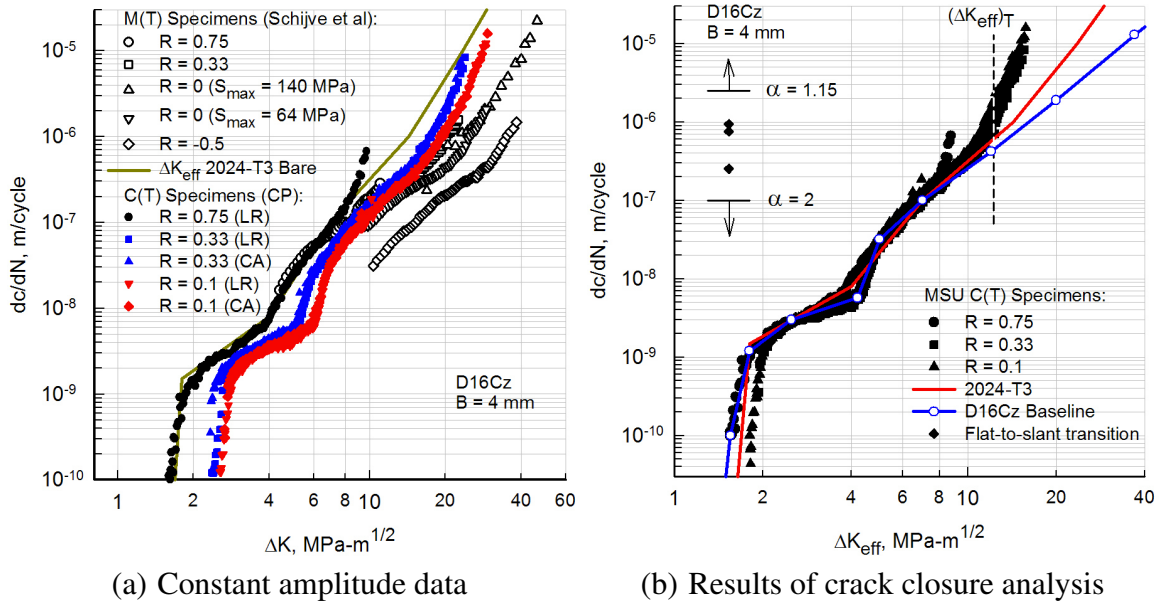
Figure 1.3

Fatigue crack growth data and crack closure analysis

1.4.2 Fracture

For most tests, fracture occurred when the crack length became long enough so that the cyclic load was sufficient to cause unstable tearing and failure. However, for some tests, the cyclic loading was stopped and a quasi-static load was applied until fracture. Using the stress-intensity factor at fracture (K_{Ie}) and crack length immediately before fracture, two fracture properties were determined: K_F, the elastic-plastic fracture toughness, and m, a configuration and material fracture parameter. These two parameters were used

during simulations to calculate the elastic critical stress-intensity factor for fracture (K_{Ie}), a parameter similar to K_{Ic} that accounts for the crack length and specimen geometry in the Two Parameter Fracture Criterion (TPFC) developed by Newman [48]. In Figure 1.4, the symbols represent the experimental fracture stress-intensity factor and normalized crack length data for D16Cz aluminum alloy. The curves are the calculated results from the TPFC for D16Cz and 2024-T3 aluminum alloys.
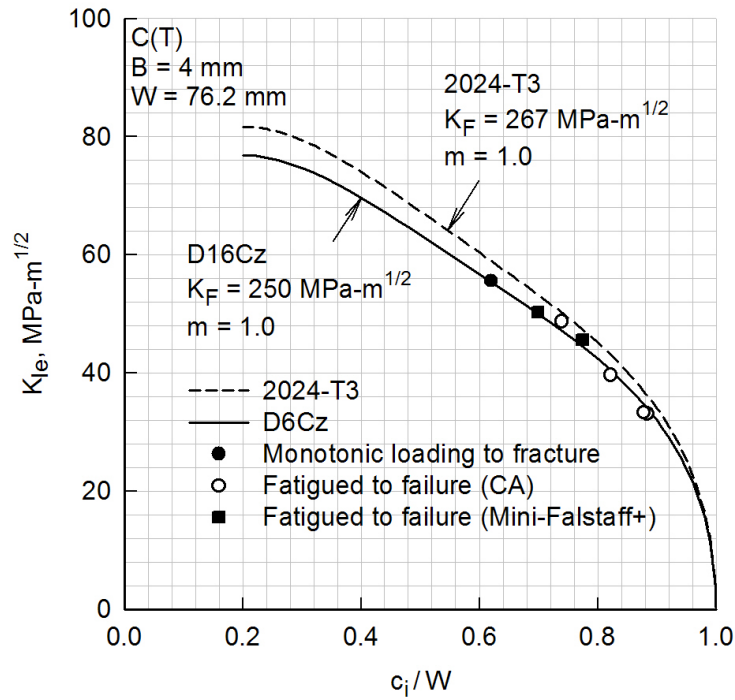
Figure 1.4

Experimental elastic fracture toughness data for D16Cz aluminum alloy and TPFC analyses

1.5 Research Objectives

FASTRAN fatigue crack growth software can model the crack growth in metals from the threshold regime up to complete fracture. In order to perform any FASTRAN predictions, it is necessary to gather accurate crack growth rate data over the complete range of crack growth and fracture. Surprisingly, a complete set of data can be gathered using a minimal number of specimens. It is a goal of this research to develop a complete and concise battery of tests, which can be used to sufficiently characterize four engineering metallic materials for FASTRAN simulations.

1.5.1 Fatigue and Crack Growth Data

When gathering crack growth rate data for material characterization in the field of fatigue or fatigue crack growth, loading history is very important. For this reason, tests need to be conducted such that the effects of load history were minimized. One method for reducing the effects of load history is CPCA testing — a notch is cyclically compressed to nucleate a crack, followed by constant amplitude cyclic loading until failure. CPCA testing can determine the approximate ΔK_{th} by using a trial-and-error procedure. To find ΔK_{th}, ASTM recommends the load shedding approach [41]; however, the load shedding approach requires initiating a crack from a notch at a tensile load, which may cause significant load history effects. CPLR testing can be used to determine an approximate ΔK_{th} more quickly than load shedding and with reduced load history effects. Performing a CPLR test gives an excellent approximation for where to begin a CPCA test. Unfortunately, it is impossible to completely remove the effects of loading history.

In order to calculate ΔK_{eff}, it is necessary to determine the stress-intensity factor at which the crack tip opens, K_{op}. As seen in Figure 1.5, ΔK_{eff} is the loading range during which the crack is open. For low load ratio ($R \approx 0.1$) tests, the information provided by the backface strain gage can be used determine K_{op} from ASTM E-647 [41]. For high-R tests, however, the backface strain gage is not sensitive enough to find a crack opening load. For these tests, a local strain gage, as described by Yamada [50], was sometimes used to find the crack opening loads for calculating the effective stress-intensity factors for each test. This research applied Yamada's findings to small-crack simulations.
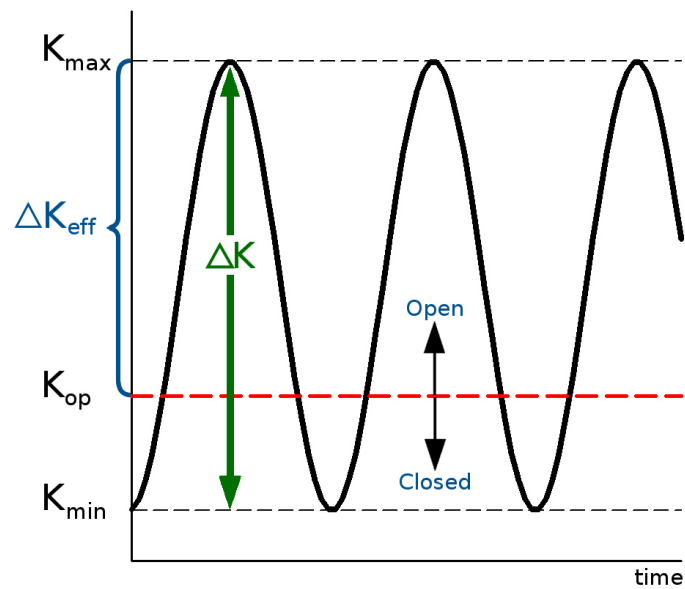
Figure 1.5

ΔK_{eff} is the stress-intensity factor ranging from K_{max} to K_{op}

The SEN(B) specimens were used to generate an S-N fatigue curve for the high-strength aluminum alloy and steel. In addition, the SEN(B) specimens were used to

generate crack length data for naturally initiated cracks. Stress-life and crack length data were compared to FASTRAN simulation results to determine the equivalent initial flaw size (EIFS), the average size of imperfections found in the material that may have lead to eventual fatigue failure, by trial-and-error. Large-crack growth rate data were analyzed for use in FASTRAN. Constant amplitude simulations were performed to confirm that FASTRAN simulations match measured crack lengths from CA and spike overload test data.

1.5.2 Fracture Data

The final load and crack length before fracture for each test, along with the material yield stress and ultimate tensile strength, were used to determine two fracture parameters, K_F and m, which encompass both material and configuration properties. These parameters were used to describe the relationship between the crack length to width ratio (c/w) and the elastic critical stress intensity factor K_{Ie}. The TPFC, which FASTRAN uses as a standard for failure, predicts fracture whenever the applied K_{max} exceeds K_{Ie}.

CHAPTER 2

TEST PREPARATIONS, METHODS, AND TOOLS

Although the present work involves the fatigue crack growth testing and analysis of four different metals using three different specimen types, there are some methods of preparation and testing that were applied to all test specimens. For example, all C(T) and ESE(T) specimens were manually polished to allow for optical crack-length measurements. For the same reason, many SEN(B) specimens were electro-chemically or mechanically polished, which provided the added benefit of relaxing the residual stresses that may have resulted from the machining process. Also, the pin holes in many of the specimens were beveled to improve the symmetry of the crack front during threshold testing. All large-crack specimens were compression precracked and all cracks were monitored optically; large-crack specimens were also monitored through the use of a backface strain gage.

2.1   Specimen Polishing

All large-crack fatigue crack growth tests required some way to measure crack length. These measurements were often made by correlating backface strains readings to a crack length. These measurements were periodically compared to optical measurements of the crack length on one side of the specimen made using a digital travelling microscope. To

aid in making accurate optical measurements, specimens were polished, either manually or electro-chemically. Through manual or electro-chemical polishing, a thin layer of material is removed and the specimen surface is left with a mirror finish. The process of manual polishing is consistent and cost effective but introduces surface residual stresses. For large-crack specimens, these residual stresses are negligible when compared to the applied loads; however, for small-crack fatigue tests, these residual stresses are far too large to be ignored. Electro-chemical polishing does not introduce residual stresses, making it a better method for polishing small-crack specimens.

2.1.1 Manual Polishing

Because the optical measurements will be performed on only one side of the specimen, only one side of the specimen is polished. The first phase of manual polishing process is sanding. Depending on the surface finish left by the machining process, the first step in the sanding phase was performed with sandpaper ranging from 250 grit to 400 grit with subsequent steps using 600 grit, 800 grit, 1000 grit, and 1500 grit. All sanding was performed with wet sandpaper that was rinsed regularly. The goal for each step in the sanding process was to remove the scratches from the previous step. For consistency, each step was broken down into three stages. During the first stage, sanding was performed in straight lines approximately 45 degrees from the mode I crack growth direction. When the entire area of potential crack growth bore scratches in only one direction, the second stage began and the direction of sanding was rotated 90 degrees. The third stage consisted of sanding perpendicular to the crack growth direction (Fig. 2.1). All three stages were

performed with sandpaper of the same coarseness. These three stages were repeated with

each step, each performed with a finer grit sandpaper. When sanding was complete, the

surface appeared to be almost scratch free to the naked eye, but when viewed through the

microscope, the surface was covered in scratches, most of them normal to the crack growth
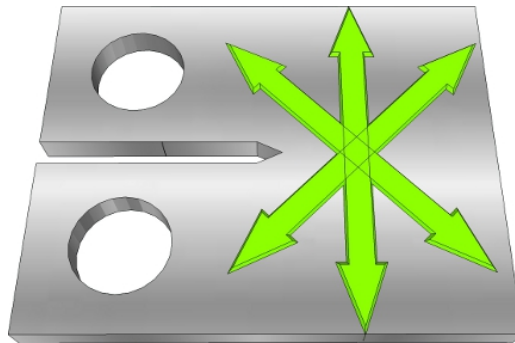
direction.

Figure 2.1

Specimen polishing directions included $\pm$ 45 degrees and 90 degrees from the crack
growth direction

After sanding, polishing was performed with a soft, non-abrasive, disposable cloth

or paper and diamond-impregnated paste. The first step in the polishing phase was per-

formed using a 15 micron diamond paste. Much like the sanding phase, each step in the

polishing phase consisted of three stages of different polishing direction. Between steps,

the specimen surface was gently and thoroughly cleaned. The final step in the polishing

phase was performed in the same manner with 1 micron diamond paste. After polishing

was complete, the specimen was gently cleaned to remove any diamond particles that may

have implanted into the surface.

2.1.2 Electro-chemical Polishing

Electro-chemical polishing was performed off-site on all 9310 Steel SEN(B) specimens. The process involves submerging the specimens in a chemical bath and applying an electrical current. The goal for the steel electro-chemical polishing was to remove a thin layer of material from the surface, relaxing the residual stresses introduced during machining and to generate a smooth and mirror-like surface. Unfortunately, after electro-chemical polishing many of the specimens contained irregular patterns of surface erosion and discoloration, found especially around the pin-holes and fatigue notch. Because of these undesirable surface irregularities, the Al7050 SEN(B) specimens were not electro-chemically polished.

2.2 Hole Beveling

Early fatigue crack growth test specimens showed a problem with asymmetric crack fronts. It was determined that this behavior was most likely caused by the specimen experiencing an out-of-plane bending load during the test. If pin-holes are not drilled precisely normal to the specimen surface for C(T), ESE(T), and SEN(B) specimens, one side of the specimen may be loaded slightly more than the other resulting in an unwanted out-of-plane bending moment. To minimize this bending moment, all the following specimen pin-holes were beveled either by hand using a circular file or as part of the machining process. Inspection of fatigue surfaces have shown that the process successfully removed most crack front asymmetry (Fig. 2.2).
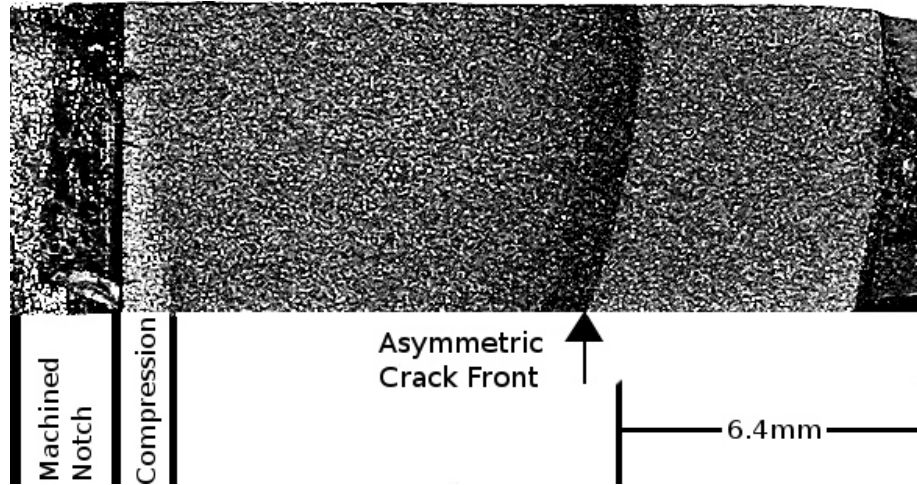
(a) Crack surface of A36 ESE(T) specimen with pin holes as drilled
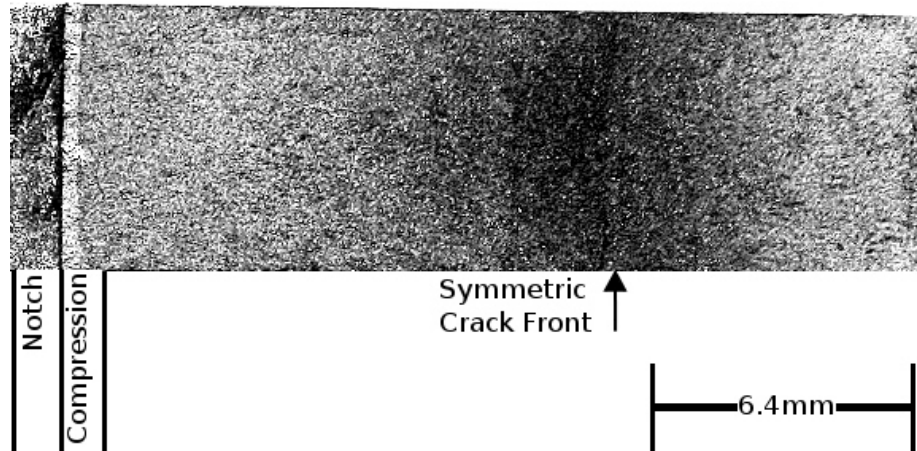
(b) Crack surface of A36 ESE(T) specimen with beveled pin holes

Figure 2.2

Early tests showed that beveling pin holes would result in a more symmetric crack fronts

2.3 Testing Methods

All tests were performed using servo-hydraulic test frames. During each test, it was necessary to gather data about crack length, crack opening load, and applied load. All large-crack specimens were compression precracked.

2.3.1 Crack Length Monitoring

For all the large-crack fatigue crack growth tests performed, it was important to have an accurate measurements, both digital and optical, of crack length at regular intervals. Optical measurements were performed manually using a traveling optical microscope. This method is accurate, but collecting data at regular intervals becomes impractical, especially for tests that last multiple days. Also, optical measurements represent the crack length at the surface, but cannot provide information about the crack length in the specimen interior. For this reason, all large-crack tests were monitored using a digital crack monitoring system, which actively measures strains at a constant location on the specimen and uses strain measurement calibrations to calculate a crack length. Most digital crack monitoring systems use one of two types of gages: crack mouth opening displacement (CMOD) gages and backface strain (BFS) gages.

CMOD gages are popular for being accurate and re-usable; however, the gage applies a small tensile load (around 40N) at the crack mouth. For tests in which the applied loads are small, the gage force has significant influence on the crack growth behavior, which must be accounted for during data analysis. For this reason, all fatigue crack growth tests used a digital crack monitoring system with a backface strain gage. Although each gage can be used only once, the gage has essentially no effects on the crack growth behavior.

In this work, all large-crack tests were monitored using a BFS gages. The crack length calculations based on these gage readings were regularly compared to optical measurements to ensure that the collected crack length measurements were accurate. For the small-crack tests, a BFS gage would have lacked the sensitivity to accurately calculate the size of small cracks. Therefore, all small-crack tests were paused at regular cyclic intervals (usually 10%–20% of the estimated fatigue life) to optically measure the surface length of each crack. Many small-crack specimens featured multiple initiation sites resulting in multiple cracks that would eventually coalesce into a single crack.

2.3.2 Monitoring Applied Loads

The loads applied by the servo-hydraulic test frame were monitored using a load cell, which is also the test frame feedback control. The choice of load cell for each test was based on the magnitude of the load being applied. Every load cell has a limit load and resolution. Cells with lower limit loads have a higher resolution. For this reason it is best to use a load cell with a limit as close as possible to the maximum expected load. For the testing described herein, either a 5kN or 25kN load cell was used.

2.3.3 Compression Precracking

All large-crack specimens have a machined notch, which is not representative of a crack. In order to induce a physical crack in the specimen, the notch must be precracked before the testing can begin. However, cyclic precracking loads can be much larger than the desired cyclic test load. One solution to this problem is to start the precracking with a load large enough to initiate a crack and then gradually reduce the load after the crack has formed. However, this results in a large plastic zone with compression residual stresses in front of the crack tip, which could potentially cause premature crack closure during testing and may result in inaccurate crack growth behavior measurements.

An alternative method is to precrack using cyclic compressive loads. Applying compressive loads to a machined notch can result in the initiation of a crack resulting from tensile residual stresses in the plastic zone at the notch as seen in Figure 2.3. These local tensile stresses will eventually initiate a crack even if the maximum applied load is compressive. After a crack is initiated, cyclic tensile loads can be applied to grow the crack. Once the crack has grown out of the influence of the precracking residual stress field, the crack growth rate data is valid.

Finite element analysis has shown the crack extension needed to grow out of the influence of precracking can be calculated using Equation (2.1) [51] with $\gamma = 2$, but to be more conservative, $\gamma = 3$ has been previously used in testing.

$$\Delta c = \gamma(1 - R)\rho_{cp} \tag{2.1}$$

where Δc is crack extension, R is the stress ratio, and ρ_{cp} is the compressive plastic zone size, which is calculated with Equation (2.2).

$$\rho_{cp} = \frac{\pi}{8}\left(\frac{K_{cp}}{\sigma_o}\right)^2 \tag{2.2}$$

for plane stress, where K_{cp} is the stress-intensity factor for the cyclic maximum compressive load and σ_o is the flow stress for the material (the average of ultimate strength, σ_u, and yield strength, σ_{ys}).
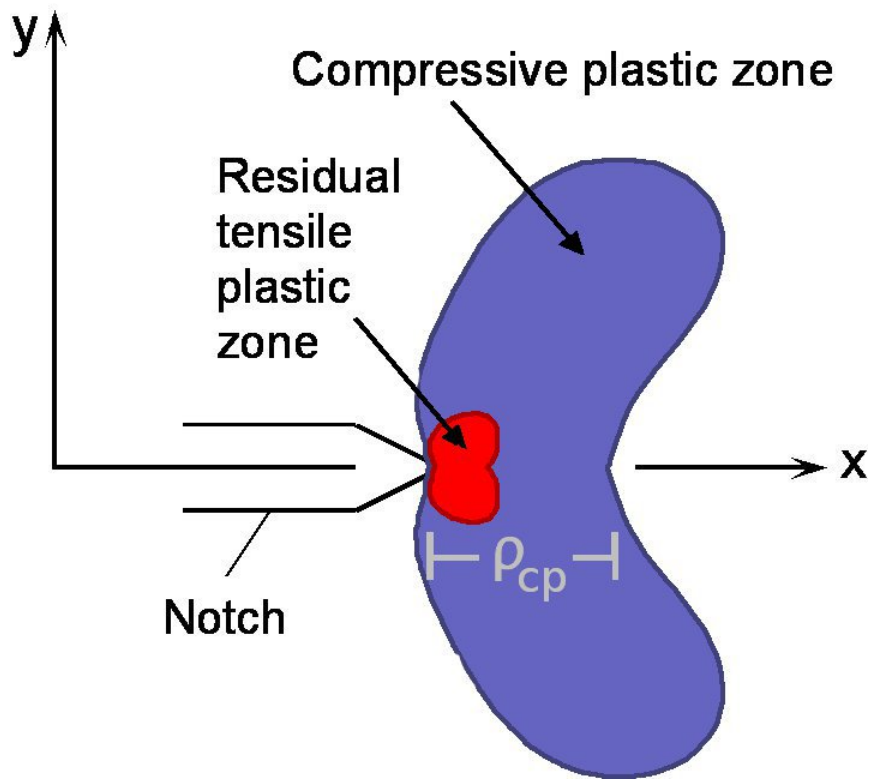
Figure 2.3

The plastic zone at the notch tip cause by cyclic compressive loading

All large-crack specimens were compression precracked with a maximum load of 450N compression to keep the specimen stationary and a minimum load calculated based on the equation $K_{cp}/E = 0.01\sqrt{mm}$ for the 9310 steel and Al 7050. A36 steel specimens were precracked with a minimum load calculated from the equation $K_{cp}/E = 0.005\sqrt{mm}$ to reduce the compressive load for safety reasons.

Compression precracking load reduction (CPLR) testing began with cyclic compressive loading, followed by constant amplitude tensile cyclic loading until the crack extension necessary to ensure stable fatigue crack growth was achieved, followed by load reduction (Fig. 2.4(a)). Compression precracking constant amplitude (CPCA) testing began with cyclic compressive loading, followed by constant amplitude tensile cyclic loading. In the event that the crack failed to grow at the applied tensile loading, the load was increased by about 5% (Fig. 2.4(b)).
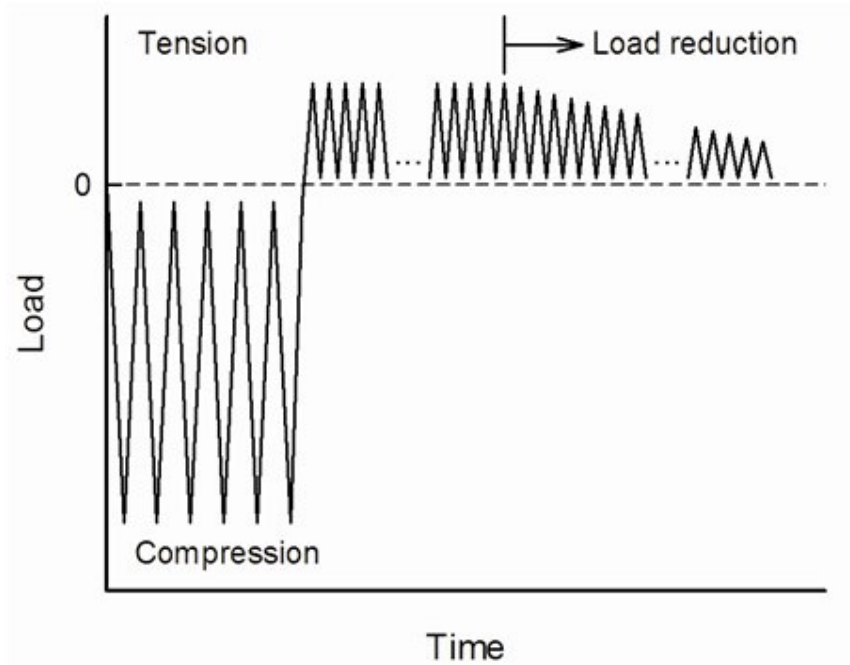
(a) Compression precracking load reduction (CPLR) loading sequence
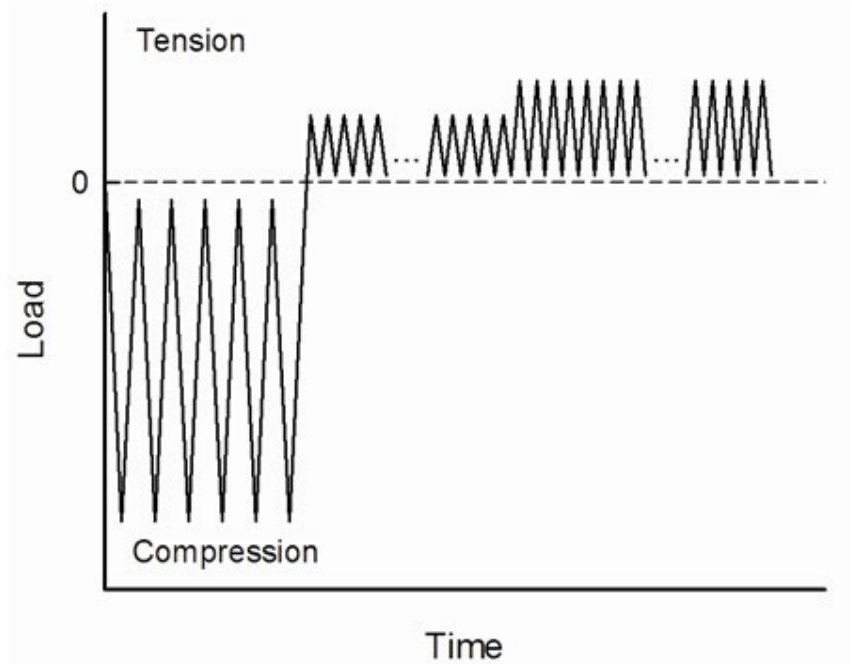
(b) Compression precracking constant amplitude (CPCA) loading sequence

Figure 2.4

Standard CPLR and CPCA load sequences

33

2.4 FASTRAN — Plasticity-Induced Crack-Closure Model

The plasticity-induced crack-closure model was developed for a central through crack and two-symmetric through cracks emanating from a circular hole in a finite-width plate subjected to uniform remote applied stress. The model was based on Elber's crack-closure concept [52] and the Dugdale strip-yield model [11], but modified to leave plastically deformed material in the wake of the crack. The details of the model are given elsewhere and will not be presented here (see Newman [45, 53]). One of the most important features of the model is the ability to model three-dimensional constraint effects. A constraint factor α is used to elevate the flow stress (σ_o) at the crack tip to account for the influence of stress state ($\alpha\sigma_o$) on plastic-zone sizes and crack-surface displacements. For plane stress conditions, α is equal to unity (original Dugdale model); and for simulated plane strain conditions, α is equal to 3.

2.4.1 Effective Stress-Intensity Factor Range

For most damage-tolerance and durability analyses, linear-elastic fatigue-crack-growth analyses have been found to be quite adequate. Thus, the effective stress-intensity factor range [52] is

$$\Delta K_{eff} = (S_{max} - S_o)\sqrt{\pi c}F \tag{2.3}$$

where S_{max} is the maximum stress, S_o is the crack-opening stress and F is the boundary-correction factor. The boundary-correction factor accounts for the effects of the configuration (boundaries, holes) on stress-intensity factors. In general, S_o is calculated from the

FASTRAN code [54], but for steady-state constant-amplitude loading, the crack-opening stress can be calculated from closed-form equations [53].

2.4.2 Constant-Amplitude Loading

Newman [53] developed steady-state crack-opening stress equations from the plasticity-induced crack-closure model for a middle-crack tension M(T) specimen subjected to constant-amplitude loading at various stress levels, stress ratios (R), and constraint factors (α). Crack-closure transients, before the crack-opening stresses stabilize under constant-amplitude loading, are not included in these equations. The FASTRAN model has to be exercised to determine these transient behaviors. Later, the FASTRAN model and the equations were modified to account for extreme crack-growth rates, such as those under high loads or proof testing. Equations were then fit to the crack opening load results from the model, which gave crack-opening stress (S_o) as a function of stress ratio (R), maximum stress level (S_{max}/σ_o), the constraint factor (α), and the amount of crack growth during a cycle normalized by the present crack length ($\Delta c/c$) [53, 55]. Since the crack-opening stress equation was developed for an M(T) specimen, K-analogy [56] is used to calculate the crack-opening stresses for other crack configurations, such as the C(T) specimen. K-analogy assume the crack opening force for a C(T) specimen is equivalent to the crack opening stress for the M(T) model when both loads yield the same stress-intensity factor for the same crack length. These equations are then used to correlate fatigue-crack-growth-rate data in terms of ΔK_{eff} on M(T) and C(T) specimens.

2.4.3 Constraint Effects

In general, the plastic-zone size at a crack front increases as a crack grows in a metallic material under cyclic loading (constant applied cyclic stresses). At low stress-intensity factor levels, plane-strain conditions should prevail, but as the plastic-zone size becomes large compared to thickness, a loss of constraint is expected. This constraint loss has been associated with the transition from flat-to-slant crack growth. Schijve [57] has shown that the transition occurs at nearly the same fatigue-crack-growth rate over a wide range of stress ratios for an aluminum alloy. Since Elber's concept [52] correlates fatigue-crack-growth rates, then the transition should also occur at the same ΔK_{eff}. This observation has been used to help select the constraint-loss regime. Newman [55] developed an expression to predict the full transition from flat-to-slant crack growth and the effective stress-intensity factor range at transition, $(\Delta K_{eff})_T$, is given by

$$(\Delta K_{eff})_T = 0.5\sigma_o\sqrt{B} \qquad (2.4)$$

where σ_o is the flow stress and B is the material thickness. The range of the constraint-loss regime, in terms of rate or ΔK_{eff}, is a function of thickness, but this relation has yet to be developed. Trial-and-error methods are currently used to establish the range in crack-growth rates where the constraint-loss regime will occur for a given material and thickness.

In the application of FASTRAN, the constraint-loss regime is controlled by crack-growth rates. For rates lower than a certain (input) value, the constraint factor is high (like plane strain), but if the rate is higher than another (input) rate, then the constraint

factor is low (like plane stress). For intermediate rates, a linear relation on log of rates is used to estimate the constraint factor between the upper and lower constraint values. The constraint factor only changes the forward plastic-zone size and crack-surface displacements under the current loading. The crack-growth model does not physically model the shear-lip or slant crack-growth process under either constant- or variable-amplitude loading. Obviously, the crack-growth process under variable-amplitude loading is quite complex and the FASTRAN model is a simple engineering approximation.

2.4.4 Crack-Growth-Rate Relation

The crack-growth relation used in FASTRAN is a multi-linear relation with terms to account for threshold and fracture, and is

$$\frac{dc}{dN} = C_{1i}(\Delta K_{eff})^{C_{2i}} \frac{\left[1 - \left(\frac{\Delta K_o}{\Delta K_{eff}}\right)^p\right]}{\left[1 - \left(\frac{K_{max}}{K_{Ie}}\right)^q\right]} \tag{2.5}$$

where C_{1i} and C_{2i} are the coefficient and power for each linear segment, ΔK_{eff} is the effective stress-intensity factor, ΔK_o is the effective stress-intensity factor range threshold, K_{max} is the maximum applied stress-intensity factor, K_{Ie} is the elastic fracture toughness (which is, generally, a function of crack length, specimen width, and specimen type), p and q are constants selected to fit test data in either the threshold or fracture regimes. Whenever the applied K_{max} value reached or exceeded K_{Ie} then the rate would go to infinity and the specimen or component would fail. The multi-linear table-lookup form is used instead of the sigmoidal form because many materials, especially aluminum alloys, show sharp changes in the crack-growth-rate curves at unique values of rates.

2.4.5 Two Parameter Fracture Criterion

Newman [58] proposed the Two-Parameter Fracture Criterion (TPFC) to correlate fracture data and to predict the elastic stress-intensity factor (K_{Ie}) at failure on cracked metallic materials. The TPFC equation is

$$K_F = \frac{K_{Ie}}{1 - m\frac{S_n}{S_u}} \text{ for } S_n < \sigma_{ys} \tag{2.6}$$

where K_F and m are the two fracture parameters, K_{Ie} is the elastic fracture toughness (elastic stress-intensity factor at failure), S_n is the net-section stress and S_u is the plastic-hinge stress based on the ultimate tensile strength. For example, for an M(T) specimen S_u is equal to σ_u, the ultimate tensile strength; for a pure bend specimen, $S_u = 1.5\sigma_u$; and for a C(T) specimen, $S_u \simeq 1.62\sigma_u$. A similar equation was derived for $S_n > \sigma_{ys}$, see [58]. The m-value is both a material and configuration parameter. It is a function of material, thickness, and, in general, specimen type (tension, bending, etc.). For brittle materials, m = 0 and the fracture toughness K_F is equal to the elastic stress-intensity at failure (like, K_{Ic}, the plane-strain fracture toughness). However, for very ductile materials, m = 1 and the fracture toughness K_F is the elastic-plastic fracture toughness, K_{Ie}; K_F is the largest limiting value for very large cracked panels and at very low failure stresses.

For $m = 1$ and a very large K_F value, Equation (2.6) reduces to a net-section-stress-equal-plastic-hinge-stress (limit-load) failure criterion based on the ultimate tensile strength. Once K_F and m are known for a material, thickness, and specimen configuration, then the K_{Ie} value can be calculated as

$$K_{Ie} = \frac{K_F}{1 - m(K_F/S_u\sqrt{\pi c}F_n)} \text{ for } S_n < \sigma_{ys} \tag{2.7}$$

for a given crack length and specimen width. (Note that F_n is the usual boundary-correction factor, F, on the stress-intensity factor with a net-to-gross section conversion [58], because the net-section stress is used in Equation (2.7).) For $S_n > \sigma_{ys}$, a more complicated equation is given in [58].

CHAPTER 3

A NEW SMALL-CRACK SPECIMEN

The single-edge notch bend (SEN(B)) specimen, Figure 3.1, was developed for performing small-crack testing using the equipment available in the Fatigue and Fracture Laboratory at Mississippi State University. Because all of the servo-hydraulic fatigue test frames use pin-loading clevises, a pin-loaded small-crack specimen was needed. The design of this specimen centered on modifying the single-edge notch tension (SEN(T)) specimen, which is a standard specimen used in the study of small cracks. One major advantage for the SEN(B) specimen is a larger stress concentration at the notch, $K_T = 11.8$, compared to $K_T = 3.17$ for the SEN(T) [59]. This makes it possible to run a test at the same local-stress level using a much lower applied load.
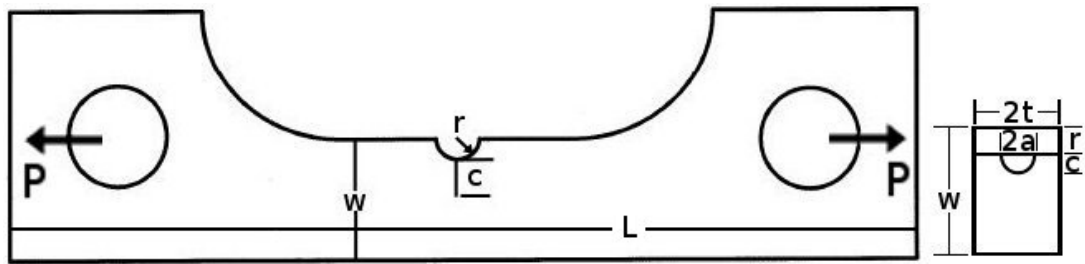
Figure 3.1

The single-edge notch bend specimen with simulated pin-loading

3.1 Designing a New Specimen

Because the SEN(B) specimen is used for testing the behavior of small surface-cracks, the specimen configuration must allow for easy access to the notch surface for both visual inspection and the application of crack surface replication material. For this reason, it was important to consider how the specimen configuration fits together with the test frame clevises. As seen in Figure 3.2, the SEN(B) configuration allows for easy access to the notch with no interference from the clevises.

The initial design for the SEN(B) specimen had a test section that was 25.4mm wide (w) and a total specimen length of 190mm (L). However, an opportunity arose for the SEN(B) specimen to be made from a 7050 aluminum alloy forging block, but the specimen length was limited to 140mm (L). In order to retain the specimen width, $w = 25.4$mm, the specimen geometry was altered including a change in total length and pin-hole diameter. These changes were made with the assumption that the changes would not alter the stress concentration at the notch or the stress-intensity factors (K-field) for a growing crack. Having two complete sets of machined SEN(B) specimens, it was necessary to perform elastic stress analysis for the new specimen with two different configurations.
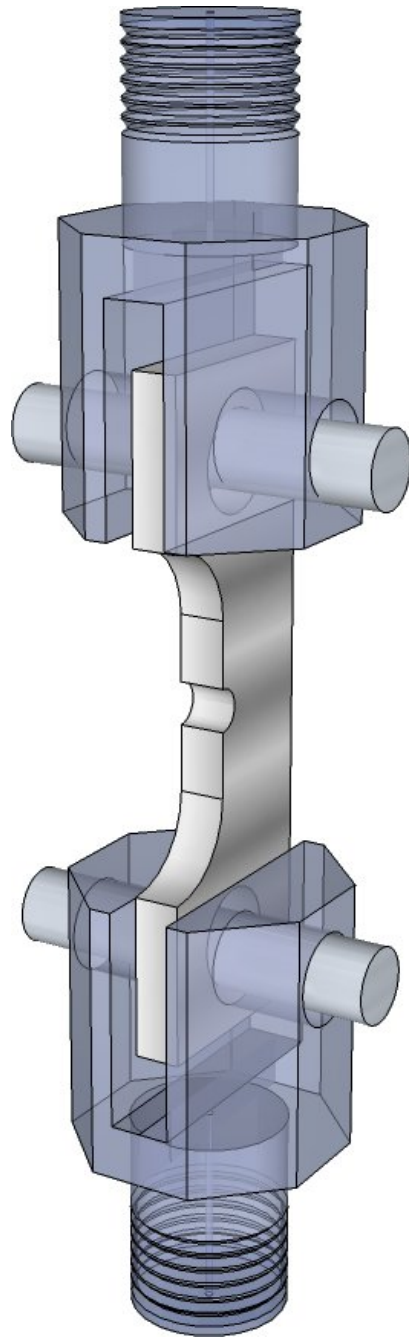
Figure 3.2

The SEN(B) specimen allows easy, unobstructed access to the notch even when pinned into a pair of clevises

3.2   Stress Analysis

In order to perform analysis on fatigue life and crack length data gathered from these new specimens, a two-dimensional elastic stress analysis of the SEN(B) geometry was performed. The goal of this analysis was to determine the stress-concentration factor for the single-edge notch and the stress-intensity factor, K, for different crack lengths (c) measured from the edge of the notch. Once the K values for multiple discreet crack lengths were determined, a polynomial was fitted to the normalized values to give a functional form for the stress-intensity factor. This functional form was based on the K-field function for the SEN(T) specimen developed by Newman et al [59].

Elastic stress analysis began with creating a full boundary element model for the larger specimen geometry (L = 190mm) using the boundary element code FADD2D. The initial model contained a very fine mesh of boundary elements around the notch since this region would have a large stress gradient. Analysis was performed with no crack to determine the stress concentration factor at the notch. Next, a crack boundary was added to the model and a stress-intensity factor was calculated for 18 different (mode I) crack lengths ranging from very small to 80% of the ligament width ($(r + c)/w$ = 0.8). This process was repeated for the smaller, L = 140mm, specimen configuration (both models can be seen in Fig. 3.3). Two-dimensional stress analysis showed that the difference between the stress concentration factors for the two specimen geometries was around $\pm 0.4\%$. Also, the stress-intensity factors for each crack length differ by less than $\pm 0.5\%$. Thus, the two configurations have nearly identical K-fields.
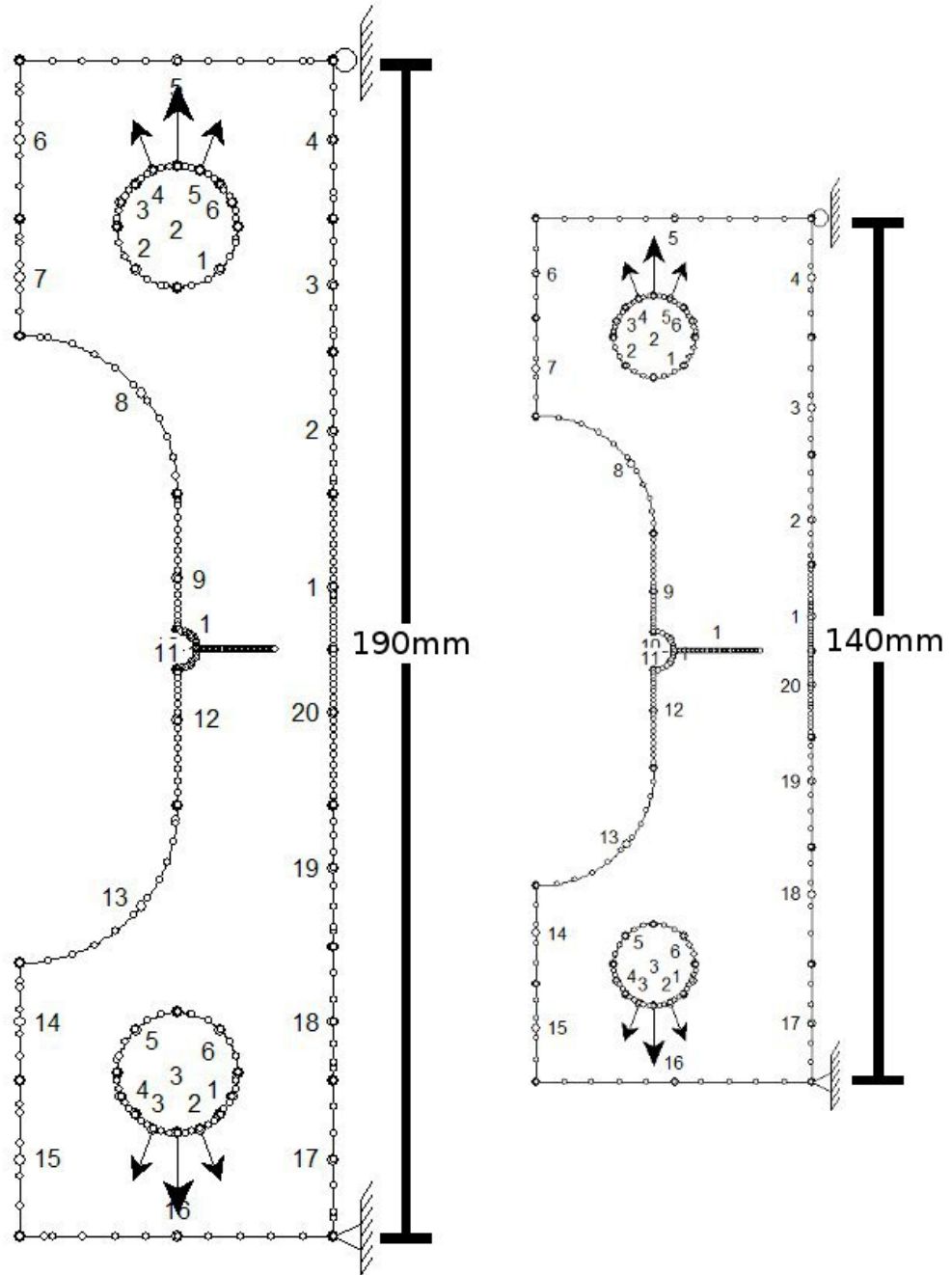
Figure 3.3

FADD2D models for two different SEN(B) geometries

Unfortunately, the boundary element model solution is most accurate when the crack-tip is not near another free surface. Since the longest crack was only 80% of the ligament width, the effects of the crack-tip approaching the backface were easily calculated; however, for very short cracks at the edge of the notch, the FADD2D results are less accurate. In order to accurately obtain the K solution for short cracks, a limiting solution was determined. In the limit as the crack length becomes extremely small, the crack should behave like an edge crack with remote loading equal to the concentrated stress and can be described by Irwin's solution for an edge crack in a semi-infinite plate [60]. To facilitate this calculation and make the curve fitting process easier, the stress-intensity, K, was normalized by the solution for a crack in an infinite plate, resulting in the boundary-correction factor, F.

$$K = S\sqrt{\pi c}F \tag{3.1}$$

where $S = P/w$ and P is load per unit thickness. For very short crack lengths,

$$K = S\sqrt{\pi c}F = 1.122\sigma\sqrt{\pi c} = 1.122SK_T\sqrt{\pi c} \tag{3.2}$$

Therefore, as the crack length approaches zero, $F = 1.122K_T$. This data point was added to the data set as the value of the boundary-correction factor at zero crack length. Figure 3.4 shows the calculated values of the boundary-correction factor, F, plotted against the normalized crack length.
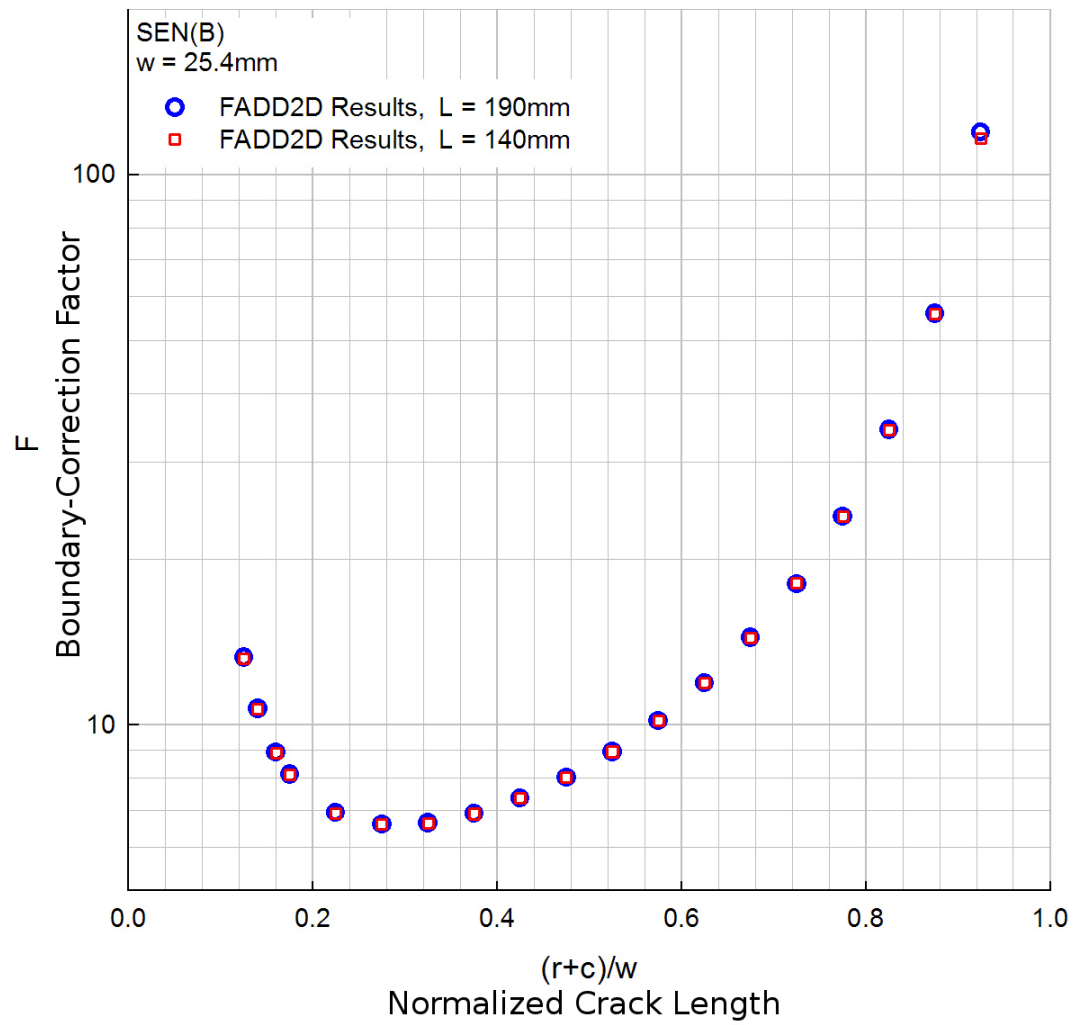
Figure 3.4

The FADD2D boundary-correction factor results for two specimen configurations

The polynomial curve fit for the boundary-correction factor was modeled after that of the SEN(T), which defines the boundary-correction factor as the product of three separate polynomials. However, because of the characteristic behavior of a bend specimen is different from a tension specimen, the boundary-correction for the SEN(B) is defined as the product of four polynomials (Equation (3.4)).

$$K_{2D_{SEN(B)}} = S\sqrt{\pi c}F \tag{3.3}$$

where

$$F\left(\frac{r}{w}, \frac{c}{w}, \frac{c}{r}\right) = f_1 g_4 f_b f_w \tag{3.4}$$

where f_1 and g_4 were taken directly from the SEN(T) specimen boundary-correction factor equation, f_b models the characteristic K-field behavior of bend specimens and was taken directly from the boundary-correction factor equation for the C(T) specimen, and f_w is a finite width correction.

Equation (3.5), f_1, and Equation (3.6), g_4, were taken directly from Newman et al [59]. These two polynomials model the behavior of short cracks from a circular notch in tension specimens. As the crack length, c, approaches zero, the product of these two functions is $1.122K_T$ and the product of the f_b and f_w must be unity.

$$f_1 = 1 + 0.358\lambda + 1.425\lambda^2 - 1.578\lambda^3 + 2.156\lambda^4 \tag{3.5}$$

$$g_4 = K_T(0.36 - 0.032\sqrt{\lambda}) \tag{3.6}$$

where $\lambda = (1 + (c/r))^{-1}$ and K_T = 11.8. Equation (3.7), f_b, models the K-field behavior of large-cracks in the bend specimens. Equation (3.8), f_w, was chosen to fit the F' data,

47

where $F' = F/(f_1 g_4 f_b)$. The finite width correction, f_w, was determined through a least-square error minimization fitting routine with the added constraint that the error be zero for a crack length of zero. Because this specimen was used to test small surface cracks, it was important that the finite width correction be accurate for very short cracks.

$$f_b = (1 - \gamma)^{-3/2} \tag{3.7}$$

$$f_w = 0.962 - 1.178\gamma + 1.307\gamma^2 - 0.554\gamma^3 \tag{3.8}$$

where $\gamma = (r + c)/w$ is the normalized crack length. The product of these four polynomials is a function that fits the FADD2D calculated boundary-correction factor results within $\pm$ 1%. In Figure 3.5, Equations (3.5)–(3.8) were plotted along with the boundary-correction factor results from the FADD2D analysis and found to yield excellent results, successfully matching both specimen geometries withing $\pm$ 1.5%.

3.3 Surface Crack in SEN(B) Specimen

Because the SEN(B) specimen was used to monitor the behavior of surface cracks, it was important to be able to calculate the stress intensity factor for surface cracks and not just through cracks. Traditionally, this would have required performing three-dimensional stress analyses for both specimen geometries over a range of crack sizes (both c and a). Instead, the concept of similitude was applied to estimate the three-dimensional stress intensity factors.
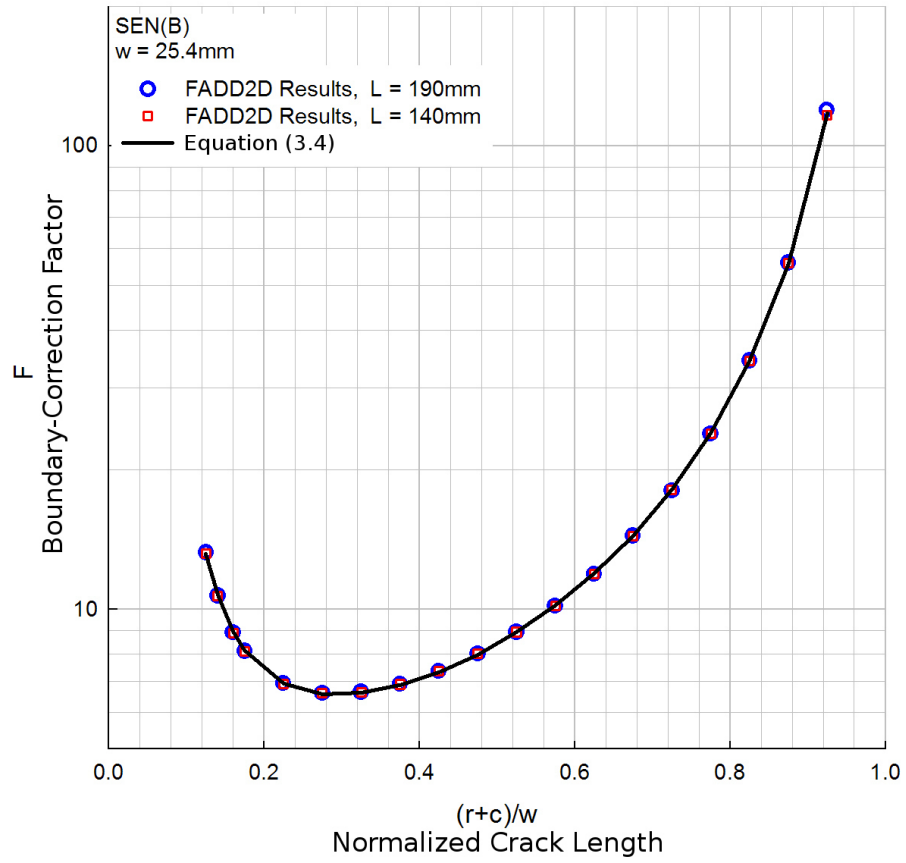
Figure 3.5

FADD2D boundary-correction factor results for through cracks with polynomial curve fit

A complete three-dimensional stress analysis was already available for the SEN(T) specimen, and the geometric similarities made it possible to use this information. Because surface cracks are only present for short crack lengths, the local stress fields for the tension and bending specimens could be assumed to be similar for surface cracks; the same local stress would produce the same three-dimensional stress intensity factor. Given the available equation for the three-dimensional boundary-correction factor for the SEN(T) specimen and the two-dimensional boundary-correction factor equations for both the SEN(B) and SEN(T) specimens, an equation was developed to calculate the three-dimensional behavior of the SEN(B) specimen (Equation (3.9)).

$$K_{3D_{SEN(B)}} = K_{3D_{SEN(T)}} \frac{K_{2D_{SEN(B)}}}{K_{2D_{SEN(T)}}} \tag{3.9}$$

For very short cracks, the equation simplifies to include the ratio of stress concentration factors.

$$K_{3D_{SEN(B)}} = K_{3D_{SEN(T)}} \frac{K_{T_{SEN(B)}}}{K_{T_{SEN(T)}}} \tag{3.10}$$

This similitude method was implemented inside the FASTRAN model for life predictions of SEN(B) specimens for both 7050 aluminum and 9310 steel. Once the model calculates that the crack has grown through the full thickness of the specimen ($a/t = 1$), the similitude is no longer necessary and the K calculations rely entirely on the equations derived from the two-dimensional (through crack) stress analysis.

3.3.1 Through Crack in SEN(T) Specimen

The two-dimensional boundary-correction factor equation for the SEN(T) speci-

men was taken from Newman et al [61] as is described by the following equations.

$$K_{2D_{SEN(T)}} = S\sqrt{\pi c} F_t \left(\frac{r}{w}, \frac{c}{w}, \frac{c}{r} \right) \tag{3.11}$$

where

$$F_t = f_1 g_4 f_w \tag{3.12}$$

with f_1 and g_4 are given by Equations 3.5 and 3.6 respectively with $K_T = 3.41$. For

uniform stress, the finite width correction, f_w was

$$f_w = 0.912 - 1.1\gamma + 3.83\gamma^2 - 4.98\gamma^3 + 2.28\gamma^4 \tag{3.13}$$

and $\gamma = (r + c)/w$ is the normalized crack length.

3.3.2 Surface Crack in SEN(T) Specimen

The three-dimensional boundary-correction factor equation for the SEN(T) speci-
men was taken from Newman et al [61] as is described by the following equations.

$$K_{3D_{SEN(T)}} = S \left(\frac{\pi a}{Q} \right)^{1/2} F_s \left(\frac{a}{c}, \frac{a}{t}, \frac{c}{r}, \frac{c}{w}, \frac{r}{t}, \frac{r}{w}, \varphi \right) \qquad (3.14)$$

where K is the stress intensity factor and t is one-half the full sheet thickness for surface
cracks and the full sheet thickness for corner cracks. The equations were developed for a
range of crack configuration parameters with $r/w = 1/8$ (the same notch-radius to width
ratio of the SEN(B) specimen).

The shape factor Q is given by

$$Q = 1 + 1.464 \left(\frac{a}{c} \right)^{1.65} \qquad \frac{a}{c} \leq 1 \qquad (3.15)$$

$$Q = 1 + 1.464 \left(\frac{c}{a} \right)^{1.65} \qquad \frac{a}{c} > 1 \qquad (3.16)$$

The boundary-correction factor equation for a semi-elliptical surface crack at the
center of a semicircular edge notch subjected to remote uniform stress or displacement is

$$F_s = \left[M_1 + M_2 \left(\frac{a}{t} \right)^2 + M_3 \left(\frac{a}{t} \right)^4 \right] g_1 g_2 g_3 g_4 g_5 f_\varphi f_w \qquad (3.17)$$

for $0.2 < a/c < 2.0$, $a/t < 1$, $1 < r/t < 3.5$, $(c+r)/w < 0.6$, $r/w = 1/8$, and
$-\pi/2 < \varphi < \pi/2$ (here t is defined as one-half the full sheet thickness.)

For $a/c \leq 1$,

$$M_1 = 1 \tag{3.18}$$

$$M_2 = \frac{0.05}{0.11 + \left(\frac{a}{c}\right)^{3/2}} \tag{3.19}$$

$$M_3 = \frac{0.29}{0.23 + \left(\frac{a}{c}\right)^{3/2}} \tag{3.20}$$

$$g_1 = 1 - \frac{\left(\frac{a}{t}\right)^4 \left(2.6 - \frac{2a}{t}\right)^{1/2}}{1 + \frac{4a}{c}} \cos(\varphi) \tag{3.21}$$

$$g_2 = \frac{1 + 0.358\lambda + 1.425\lambda^2 - 1.578\lambda^3 + 2.156\lambda^4}{1 + 0.08\lambda^2} \tag{3.22}$$

$$\lambda = \frac{1}{1 + \frac{c}{r}\cos(0.9\varphi)} \tag{3.23}$$

$$g_3 = 1 + 0.1(1 - \cos(\varphi))^2 \left(1 - \frac{a}{t}\right)^{10} \tag{3.24}$$

$$g_4 = K_T \left(0.36 - \frac{0.032}{\left(1 + \frac{c}{r}\right)^{1/2}}\right) \tag{3.25}$$

where K_T is the elastic stress concentration factor ($K_T = 3.41$ for uniform stress with

$r/w = 1/8$) at the semicircular notch, and

$$g_5 = 1 + \left(\frac{a}{c}\right)^{1/2} \left[0.0003 \left(\frac{r}{t}\right)^2 + 0.035 \left(\frac{r}{t}\right)(1 - \cos(\varphi))^3\right]$$
$$-0.35 \left(\frac{a}{t}\right)^2 \left(1 - \frac{a}{2c}\right)^3 \cos(\varphi) \tag{3.26}$$

For uniform stress, the correction f_w was

$$f_w = 0.912 - 1.1\gamma_{3D} + 3.83\gamma_{3D}^2 - 4.98\gamma_{3D}^3 + 2.28\gamma_{3D}^4 \tag{3.27}$$

and

$$\gamma_{3D} = \left(\frac{a}{t}\right)^{1/2}\frac{c}{w} + \frac{r}{c} \tag{3.28}$$

The a/t term was included in γ_{3D} to reflect the reduced influence of width on the finite-width correction for a surface and corner crack. The function f_φ is given by

$$f_\varphi = \left[\left(\frac{a}{c}\right)^2 cos^2(\varphi) + sin^2(\varphi)\right]^{1/4} \tag{3.29}$$

For $a/c > 1$,

$$M_1 = \left(\frac{a}{c}\right)^{1/2}\left(1.04 - \frac{0.4c}{a}\right) \tag{3.30}$$

The functions M_2, M_3, g_1, g_2, λ, g_3, g_4, g_5, and f_w are given by Equations (3.18)–(3.27), respectively, and f_φ is given by

$$f_\varphi = \left[\left(\frac{c}{a}\right)^2 cos^2(\varphi) + sin^2(\varphi)\right]^{1/4} \tag{3.31}$$

54

CHAPTER 4

A LOW-STRENGTH ALUMINUM ALLOY

In 2004, Schijve et al [42] presented the results of various fatigue-crack-growth-rate tests on the aluminum alloy D16Cz (clad) sheet, a Russian alloy considered to have crack-growth properties similar to the 2024-T3 alloy. Later, these test results were compared to calculations made with the NASGRO [62] life-prediction code by Skorupa et al [63]. The NASGRO model equations were similar to those developed in the FASTRAN life-prediction code [54], which are based on Elber's crack-closure concept [52] and the Dugdale strip-yield model [11]. The NASGRO code has two strip-yield model options: (1) variable constraint in the plastic-zone region, and (2) constant constraint in the plastic-zone region. Both options were used, and the article states that "No analysis option enabled to reproduce crack growth retardation observed after application of a single overload cycle. ... Improving the predictions for VA (variable-amplitude) loading would require choosing lower values of the fitting parameter (α) which, however, would worsen the predictions for CA (constant-amplitude) loading" [63]. The unexpected inconsistencies found in these comparisons and the emphasis on the constraint-loss regime has inspired the present work.

Using material provided by the research group in Poland (M. Skorupa and T. Machniewicz, University of Science and Technology), a series of fatigue-crack-growth tests were performed on compact, C(T), specimens machined from previously fractured middle-crack tension, M(T), specimens. Testing included constant-amplitude loading at several stress ratios (R) and a single-spike overload test. Test data generated under constant-amplitude loading on the C(T) specimens were combined with the test data by Schijve et al [42] on M(T) specimens to develop a multi-linear curve describing the relationship between crack-growth rate (dc/dN) and the effective stress-intensity factor (ΔK_{eff}) using proper constraint factors. The constraint factor models the elevation of the flow stress around a crack front due to the tri-axial stress state [45, 53]. The constraint factor (α) is a key parameter in the correlation of fatigue-crack-growth-rate data and the prediction of crack growth under variable-amplitude loading. It was determined many years ago that constant-amplitude test data was necessary, but not sufficient to establish the constraint factors [64, 65]. Single-spike or repeated-spike overload tests are needed to establish the proper constraint factors. Of course, the constant-amplitude tests at various stress ratios (R) may be used to estimate an initial value of the constraint factor. In addition, a constraint-loss regime (transition from plane strain to plane stress) [55] occurs as the plastic-zone size approaches the sheet thickness, which allows slip-bands to develop through the thickness, and the crack surfaces develop full slant (single shear) or double-shear fracture [57, 66].

4.1 Material

The material used was the Russian alloy D16CzATWH, which appears to be similar to the American alloy 2124. It is a high purity clad alloy. Tensile testing performed by Schijve et al [42] determined the mechanical properties to be σ_{ys} = 335 MPa, σ_u = 457 MPa and an elongation of 22%. The high elongation (as compared to 2024-T3) is likely explained by the low impurity content (Fe and Si) and the crack-growth properties are considered to be similar to the 2024-T3 alloy [42].

The material used in the current study was obtained from the research group in Poland (M. Skorupa and T. Machniewicz, University of Science and Technology). They had conducted crack-growth tests on M(T) specimens (Fig. 4.1(a)) made of the D16Cz alloy and have made the broken halves of eight specimens available. From these broken halves, nine C(T) specimens were machined, as shown in Figure 4.1(b).

Standard ASTM plan-form C(T) specimens were machined from the broken halves of a number of previously tested M(T) specimens in the as-received thickness. Most C(T) specimens came from only one half of an M(T) specimen, however, there were two C(T) specimens machined from one specimen. Due to the loss in luster experienced during the machining process, the specimens were once again polished to 1-micrometer to facilitate visual crack measurement. Specimens were polished on only one side causing a slight reduction in the thickness of the cladding layer on one side of the specimens. To initiate a crack, a 45° V-notch with a tip radius less than 0.1 mm was electrical-discharge-machined (EDM) into all C(T) specimens. Tests were conducted on the 76.2 mm C(T) specimens over a range of stress ratios (R) and a single-spike overload.
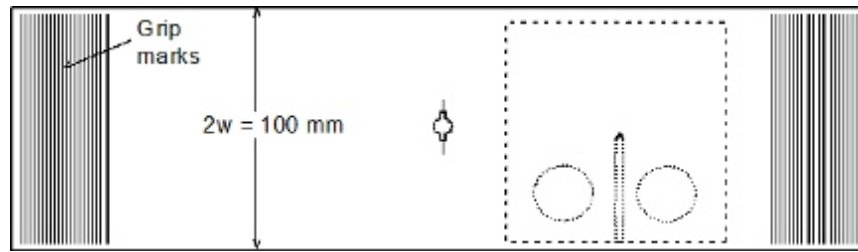
(a) Middle crack tension specimen
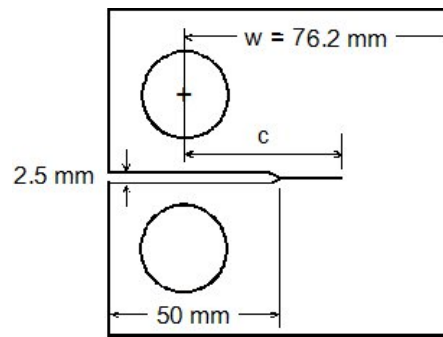
(b) Compact specimen

Figure 4.1

C(T) specimens machined from the broken halves of M(T) specimens

4.2   Testing

Fatigue-crack-growth-rate data under constant-amplitude loading were obtained from the literature on M(T) specimens made of the D16Cz alloy [42] . All C(T) tests were conducted at Mississippi State University on a 25 kN servo-hydraulic load frame operated through the aid of a steady-state and variable-amplitude fatigue-crack-growth software. Crack lengths were measured visually with a traveling microscope and with a backface strain gage. The backface strain gage was used with a compliance relation that enabled the software to automatically monitor crack lengths during the fatigue-crack-growth tests. D16 aluminum alloy testing was divided into two types — constant amplitude and single-spike overload.

58

4.2.1 Constant-Amplitude Loading

The CA tests on the M(T) specimens were performed by Schijve et al [42] at different stress ratios varying between R = -0.5 to 0.75. CA testing on the C(T) specimens was performed at a frequency of 18 Hz. Compression precracking threshold testing procedures [67, 68, 51, 69] were used to generate very low fatigue-crack-growth rates without possible load-history effects from using the current ASTM load-reduction procedure [41]. All specimens were subjected to compressive precracking. Three of the tests were compression precracked load reduction (CPLR) tests at R = 0.75, 0.33 and 0.1. After compression precracking, constant-amplitude loading was applied to grow the crack about 3 compressive plastic-zone sizes (see Equation (2.1)) at which point effects of tensile residual stresses due to compressive yielding would have dissipated and the crack-closure behavior would have stabilized [51]. At this point, it was possible to begin a load-reduction scheme, per ASTM E-647 procedures [41], that provided data at rates approaching threshold. In addition, two tests were conducted using the compression precracked constant-amplitude (CPCA) method at both R = 0.1 and 0.33. These tests involved starting with the compression precracked specimen and then applying very low ΔK values until the crack grew. When it became apparent that rates were slowing down and approaching a threshold, the load was slightly increased. This process continued until steady crack growth was achieved. The five tests produced crack-growth-rate data ranging from threshold to near fracture at stress ratios ranging from R = 0.1 to 0.75.

4.2.2 Single-Spike Overload

A single-spike overload (OL) test was performed on a C(T) specimen to help establish the constraint factors and to verify the ability of the FASTRAN code to account for crack-growth acceleration and delayed retardation after the OL. CA loading (R = 0.1) was applied until the crack length had reached 40 mm. Then an OL of twice P_{max} was manually applied. The OL was removed and the CA loading was applied until sufficient crack growth had occurred to ensure that the effects of the OL had dissipated. This specimen was then monotonically loaded to failure to gain information about the fracture toughness.

4.3 Data Analysis and Results

To make crack-growth predictions, ΔK_{eff} as a function of the crack-growth rate must be obtained over the widest possible range in rates (from threshold to fracture). Under constant-amplitude loading, the only unknown in the analysis is the constraint factor, α. Assuming that the $R = 0.75$ test is a fully-open crack, i.e. $\Delta K_{eff} = \Delta K$, the ΔK-rate data at the other R values can be used to find a constraint factor that would match the low- and high-R data on a ΔK_{eff} basis. A crack-opening ratio was found for each test data point (ΔK-rate for $dc/dN < 10^{-7}$ m/cycle) to match a best-fit curve to the high-R (0.75) data. These results are shown in Figure 4.2. Here the P_o/P_{max} ratio is plotted against the stress ratio. The solid symbols show the mean and scatter bands from several hundred data points at each R value. The solid curves are calculated result [53] for various constraint factors at a low applied stress; and the dashed curve at $S_{max}/\sigma_o = 0.3$ for $\alpha = 2$. For low rates,

a constraint factor of $\alpha = 2$ matches the average results quite well and will be used as the initial guess for the constraint factor. (A constraint factor of $\alpha = 2.85$ was previously used by Skorupa et al [63] in the evaluation of the NASGRO strip-yield model calculations. This value is very close to plane-strain conditions and would not cause as much crack-growth delay after an overload). But constant-amplitude data alone is not sufficient to establish the proper constraint factors. Single-spike overload and/or repeated spike overload tests have been used to help determine the proper constraint factors [64, 65] by trial-and-error procedures. In the following, the ΔK_{eff}-rate relation for the D16Cz aluminum alloy tested at room temperature was developed from the C(T) and M(T) specimen data.
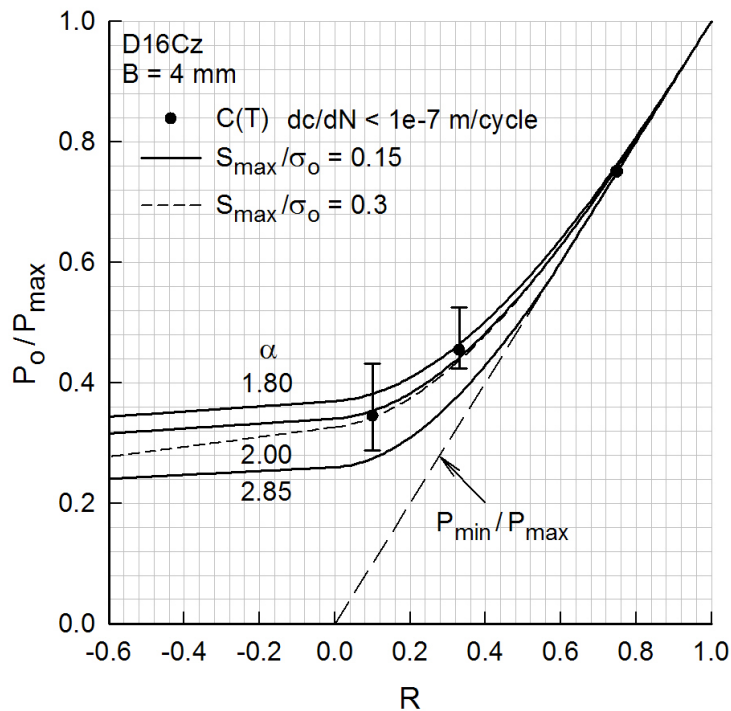

Figure 4.2

Crack-opening load ratio as a function of stress ratio from CA tests

61

4.3.1   Constant-Amplitude Loading

The ΔK-rate data from both C(T) and M(T) [42] specimens are shown in Figure 4.3 over a wide range of rates and stress ratios. (Note that ΔK is full range for the R = -0.5 test.) The solid curve is the ΔK_{eff}-rate relation for 2024-T3 bare aluminum alloy [55]. The C(T) and M(T) data at $R = 0.75$ agreed well with each other and also agreed with the 2024-T3 curve. Of concern was the rapid transition in the ΔK-rate data in the range of $dc/dN = 5 \cdot 10^{-9}$ to $5 \cdot 10^{-8}$ m/cycle for $R = 0.1$ and 0.33. Because of this behavior, two duplicate tests were conducted at the two low R ratios to verify the existence of the rapid transition.

The data shown in Figure 4.3 was analyzed with the FASTRAN crack-closure model and these results are shown in Figure 4.4 for the C(T) specimens. Elber's effective-stress-intensity-factor [52], ΔK_{eff}, is plotted against crack-growth rate. The crack-opening stresses from the crack-closure model, FASTRAN, were used to correlate these data [53]. As previously mentioned, the constraint-loss regime has been associated with the transition from flat-to-slant crack growth. The diamond symbols show rate measurements made on C(T) specimens where full-slant conditions were met. The dashed vertical line shows the calculated $(\Delta K_{eff})_T$ value from Equation (2.4) where the flat-to-slant crack-growth transition should occur for this sheet material. The rate location along the ΔK_{eff}-rate curve agreed well with the measured rates (diamond symbols). Currently, the selection of the constraint factors and their associated rates, during the constraint-loss regime, has to be obtained by trial-and-error. It is, however, suspected that the start of the slant-crack growth regime is independent of sheet thickness and occurs as the plastic zone at the free
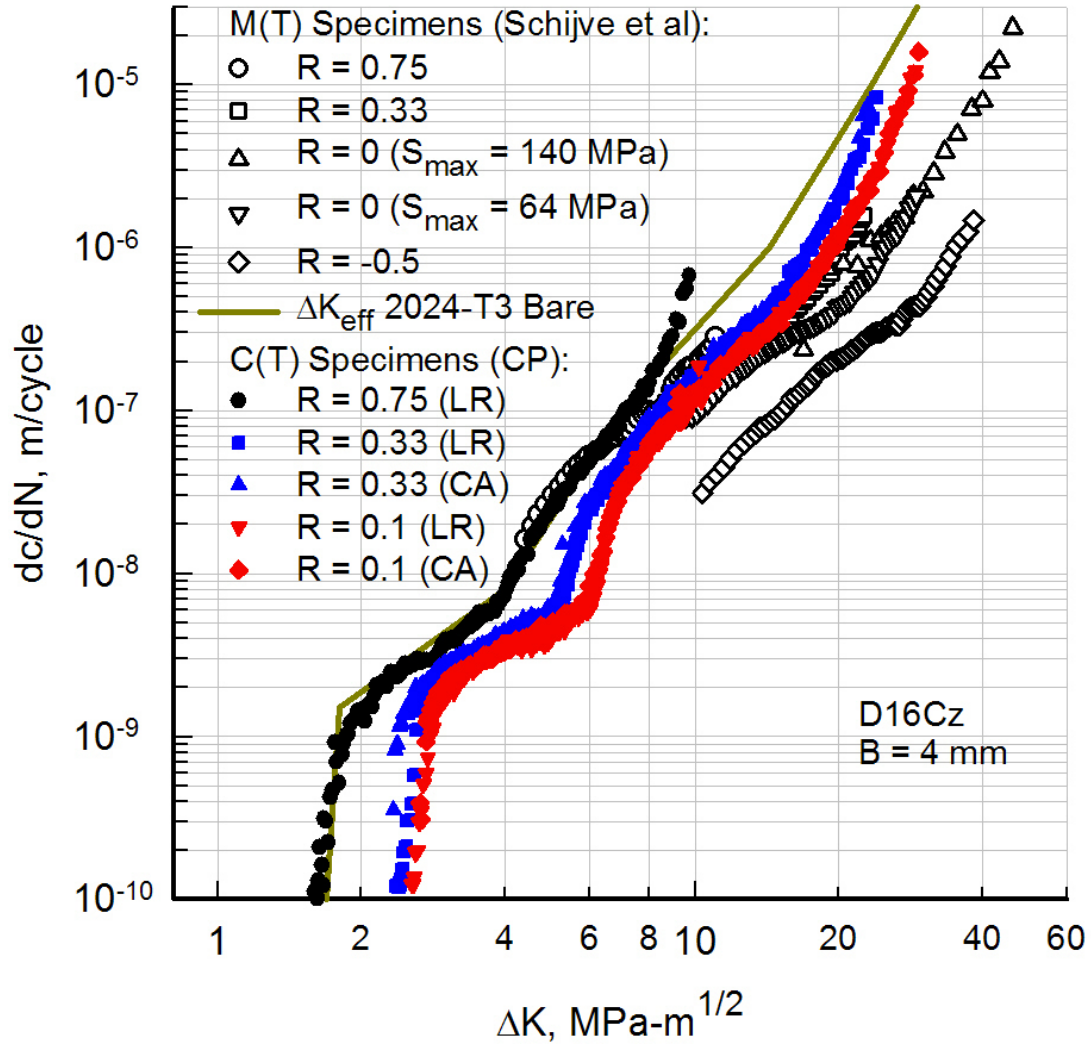
Figure 4.3

LEFM ΔK against rate for C(T) and M(T) [42] D16Cz specimens

surface begins to allow shear deformations. But the attainment of the fully slant-crack

growth (45°) is a function of the sheet thickness. For crack-growth rates less than 10^{-7}

m/cycle, a constraint factor, $\alpha_1 = 2.0$ was used, but above a rate of $2.5 \cdot 10^{-6}$ m/cycle, a

constraint factor, $\alpha_2 = 1.2$ was used. The compressive constraint factor, β, was assumed

to be unity because a closed crack has no singular behavior. The crack-closure model

correlated the fatigue-crack-growth rate data in a tight band over a wide range in rates. More scatter or variations were observed in the constraint-loss regime, near fracture, and in the near threshold regime. In Figure 4.4, the large open circles with the solid lines show the ΔK_{eff}-rate baseline relation chosen to fit these data and used as the table-lookup input, Equation (2.5), in the FASTRAN code.

Figure 4.4

Effective stress-intensity factor (ΔK_{eff}) against rate for C(T) specimens

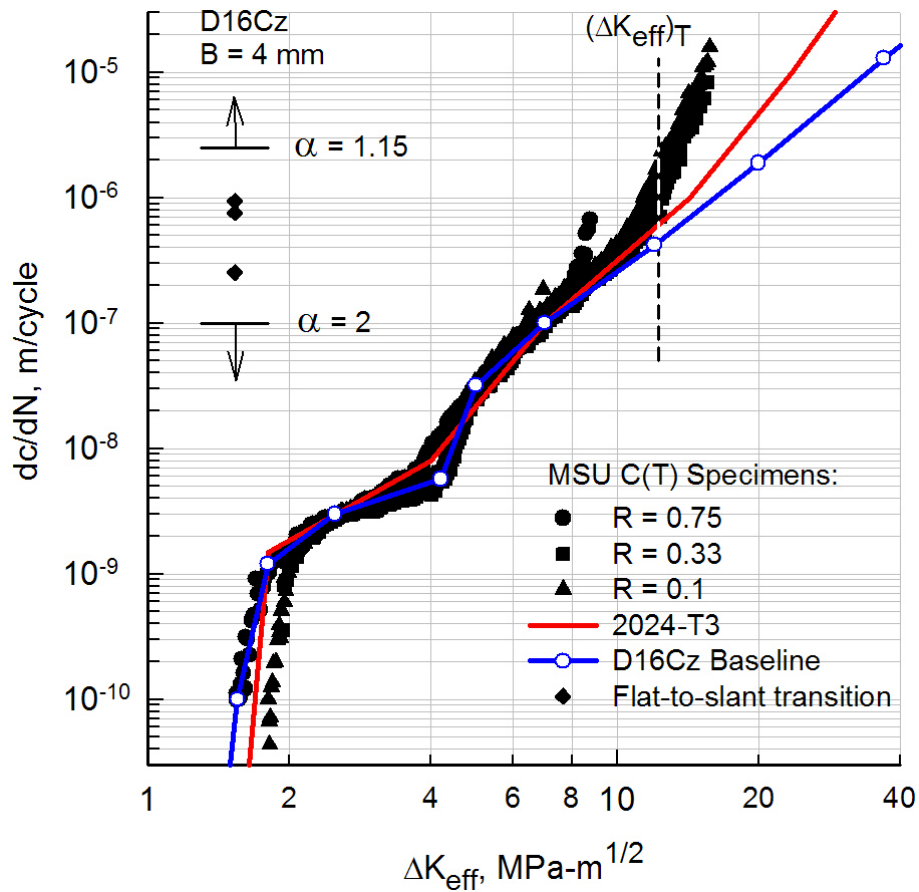Figure 4.5 shows K_{Ie} against crack-length-to-width (c_i/w) ratio for C(T) spec-imens. The symbols show the fracture test data on the D16Cz alloy. Most specimens were fatigued to failure, but one specimen was fatigued and then monotonically pulled to failure (solid circle). These results show that K_{Ie} is a function of crack length. Also, larger width specimens produce larger K_{Ie} values at failure for the same crack-length-to-width ratio (not shown), and the K_{Ie} values approach zero as the crack length approaches the specimen width. The fracture toughness, K_F was found to be 250 MPam$^{1/2}$. and $m = 1.0$ for the D16Cz alloy. The TPFC (solid curve) fit the test data very well for the C(T) specimens. The dashed curve shows the calculated K_{Ie} values for the 2024-T3 alloy [58]. For years, the transferability of fracture properties from bend- to tension-loaded crack configurations has been a concern of the fracture community. For the 2024-T3 alloy, the same values of K_F and m have been used to predict failure on M(T) specimens [58].

A comparison of calculated crack-length-against-cycles for the C(T) specimens subjected to constant-amplitude loading are shown in Figure 4.6. The test data are shown as symbols and the FASTRAN calculations are shown as curves. For clarity, the test data and curves have been offset in cycles to separate the curves. The sharp knees in the C(T) curves correspond to the rapid change in rate behavior around 1e-8 m/cycle (see Fig. 4.4) on the ΔK_{eff}-rate curve. The agreement between the tests and model calculations was within about $\pm 25\%$.
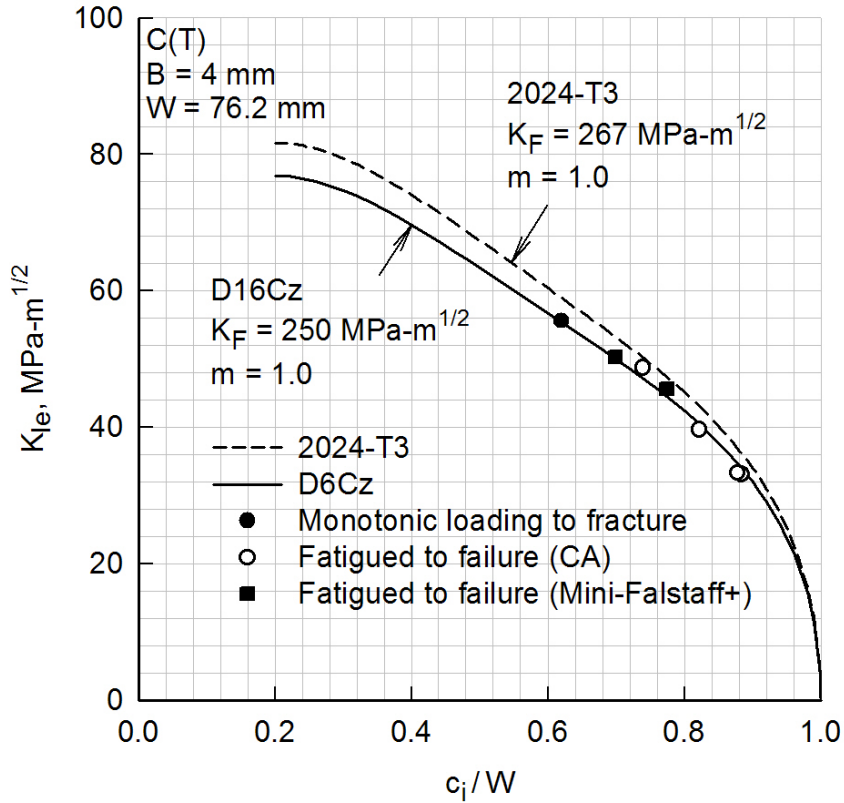
Figure 4.5

Elastic stress-intensity factor at failure on C(T) specimens

4.3.2 Single-Spike Overload

A single-spike overload (OL) test on a C(T) specimen was used to help substantiate the selection of the constraint factors (α, β) in the crack-closure model. Figure 4.7 shows a comparison between the OL test results and model calculations. For the C(T) specimen, the model predicted the CA portion very well, but slightly over predicted the retardation. But the agreement between the model and test data was within 10% and demonstrated that the delayed retardation could be modeled very well, if the proper constraint factors are used.

66

Figure 4.6

Crack length against cycles for C(T) specimens and model calculations under CA loading

Figure 4.7

Crack length against cycles for a C(T) specimen and model calculations for a single-spike overload

4.4   Conclusions

The test program conducted by Schijve et al. [42] on the D16Cz clad aluminum alloy, and used by Skorupa et al [63] to assess the NASGRO strip-yield model options, produced results that were primarily in the constraint-loss regime, which is a difficult region because of the uncertainties in the constraint factors and the pro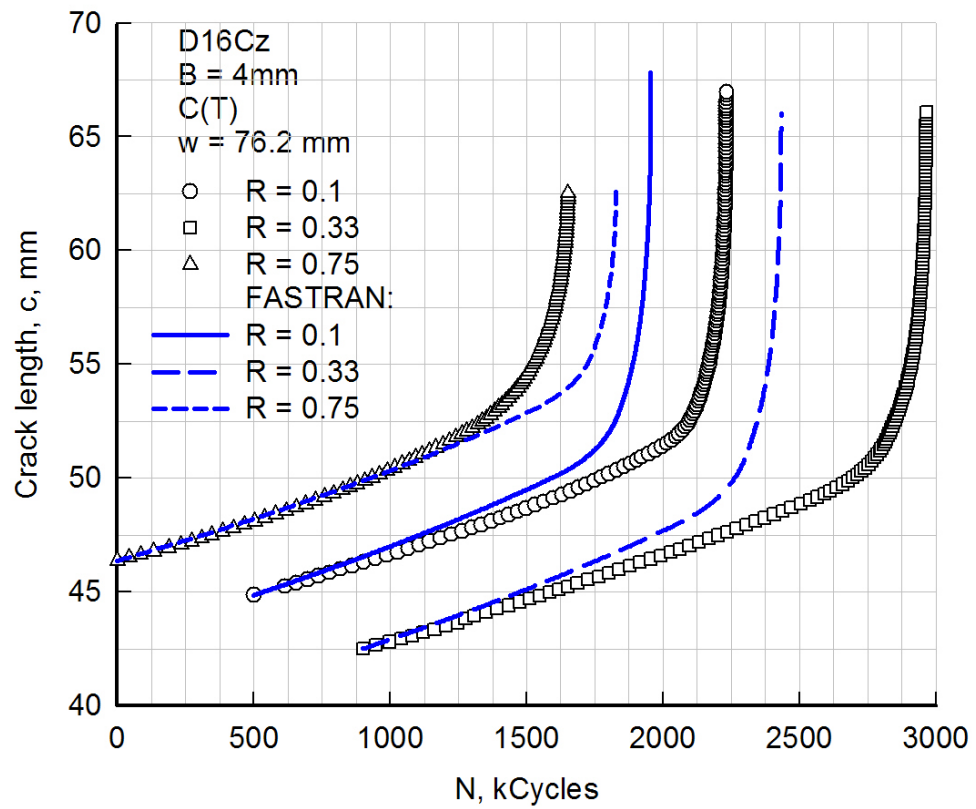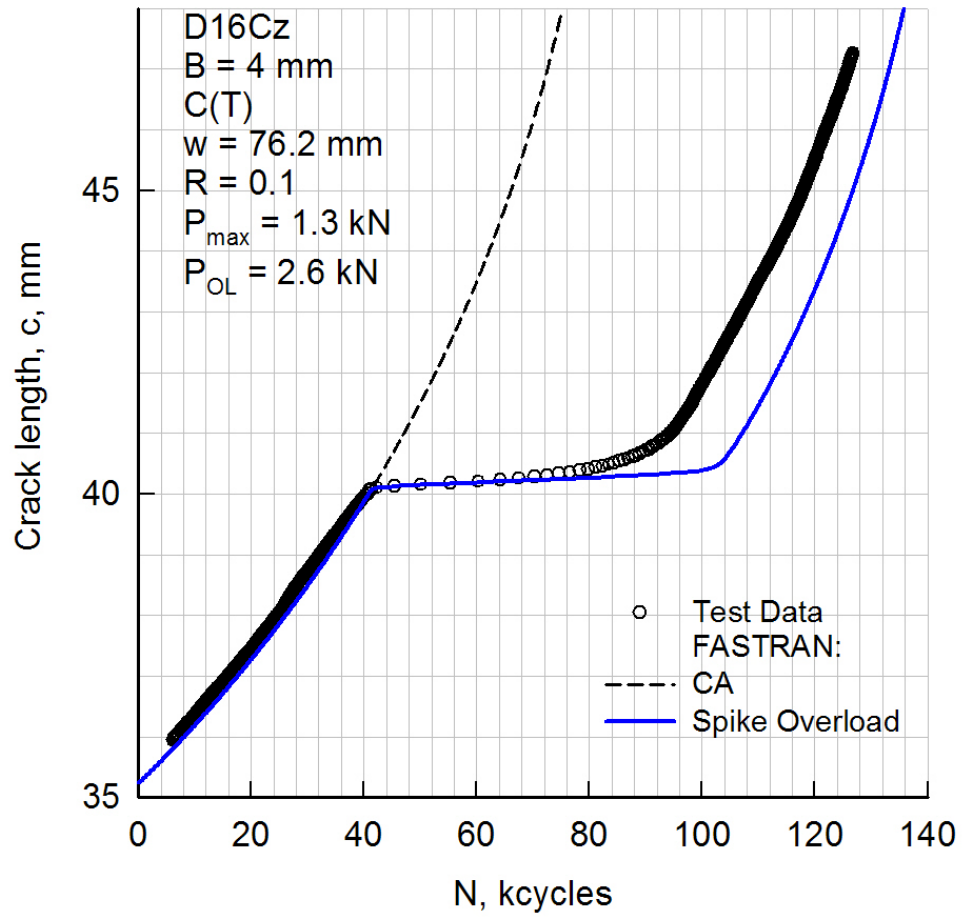ximity of fracture conditions. The test program conducted herein on C(T) specimens made of the same exact material generated fatigue-crack-growth-rate data from threshold to near fracture for stress ratios of 0.1, 0.33 and 0.75. The CA test data from the M(T) and C(T) specimens for the same stress ratio agreed very well. Some differences were observed in the fracture region because the linear-elastic stress-intensity-factor does not correlate fracture conditions. Thus, a Two-Parameter Fracture Criterion (TPFC) was used to help model fatigue-crack growth as the cracks grew to failure. The TPFC worked well on both specimen types (tension and bending) using the same fracture constants (K_F and m).

As the cracks grew to failure under cyclic loading, it was observed that the higher R ratio tests tended to show more double-shear fatigue surfaces than the low-R tests, which tended to develop single shear (slant) fatigue surfaces. This change in failure mode has also been associated with the constraint-loss regime. In other studies, it had also been observed that double-shear failure modes promote slower crack growth and higher fracture toughness. This may explain some of the under predictions made with the strip-yield model for high-R loading.

A rapid rise in rate behavior was observed between the lower and upper plateaus around 10^{-8} m/cycle. A few data points in the early stages of fatigue-crack growth in the M(T) specimens tended to match the rapid-rise region observed in the C(T) specimens. The slope of the data in this region appeared to be the same for the two low R-values (4 tests), but the R = 0.75 results (one test) exhibited a slightly lower slope. A difference was also observed in the threshold region for the ΔK_{eff}-rate data with the two low-R results agreeing and producing a slightly higher threshold (17%) than the R = 0.75 test results. However, the high-R results were selected in the table-lookup method to model the threshold behavior. Overall, the constant-amplitude data correlated very well between both specimen types over a wide range in rates and stress ratios.

The single-spike overload test demonstrated that retardation and acceleration behavior could be accurately modeled with the strip-yield model once proper constraint factors were selected and the constraint-loss regime established. Using the FASTRAN life-prediction code (strip-yield model), crack-growth behavior was calculated for CA and OL cases. Model prediction under the single-spike overload test on the C(T) specimen was well within 10% of the test data.

CHAPTER 5

A HIGH-STRENGTH ALUMINUM ALLOY

The high-strength aluminum alloy (7050) is a common material to be found as part of a number of aircraft structures experiencing higher static and cyclic loads. It is for this reason that analytical models need to be available to the design industry. Also, because some parts may be nearly impossible to inspect properly, the maintenance community is in need of an accurate model for high-strength aluminum alloy, especially as many aircraft today are reaching their design life and passenger safety stands in the balance.

Large- and small-crack testing was performed on a high-strength aluminum alloy, Al 7050-T7451. The data collected was used to generate a material model for use in the FASTRAN strip-yield model. The purpose of this suite of tests and the following analysis was to generate the data required to accurately model the fatigue crack growth behavior of this engineering material. To help support the findings, additional small-crack data was found in the literature. After testing and analysis was completed, the tests were simulated using FASTRAN to validate that the model could, within acceptable accuracy, duplicate the test results for fatigue life and fatigue crack growth.

5.1 Material

Compact, C(T), specimens (B = 6.35mm) were used to generate fatigue crack growth rate data on the 7050-T7451 aluminum alloy. The yield stress was σ_{ys} = 470MPa, the ultimate tensile strength was σ_u = 525MPa, and the modulus of elasticity was 76 GPa. C(T) specimens had a width w = 50.8mm. The specimens did not have the standard V-notch, but had an EDM (electrical-discharge machine) rectangular notch 10mm long, measured from the pin-hole centerline, with a total notch height of 0.25mm. In addition, the edges of the pin holes in the specimens were beveled to avoid or minimize undesired out-of-plane bending moments (pins forced to contact near mid-thickness of specimen).

5.2 Testing

All C(T) and SEN(B) tests were conducted at Mississippi State University on a 5 kN servo-hydraulic load frame operated through the aid of a steady-state and variable-amplitude fatigue-crack-growth software. Crack lengths were measured visually with a traveling microscope and with a backface strain gage. The backface strain gage was used with a compliance relation that enabled the software to automatically monitor crack lengths during the fatigue-crack-growth tests. The testing of 7050 aluminum alloy was divided into two regimes: large-crack and small-crack testing. The large-crack testing procedure, which consisted of continuous digital data collection, yielded fatigue crack growth information. Alternatively, the small-crack testing procedure yielded mostly fatigue life information. The combined data from these two regimes was necessary to properly characterize the behavior of this high-strength aluminum alloy.

5.2.1 Large-Crack Testing

All large-crack testing for Al7050 was performed using w = 50.8mm compact (C(T)) specimens and servo-hydraulic test frames. The pin-holes of all Al7050 C(T) specimens were beveled manually as a way to reduce out-of-plane bending. The C(T) specimens were manually polished to 1 micron to facilitate optical crack measurements. These optical measurements, performed with a travelling microscope, were used to verify the accuracy of crack lengths calculated through the use of a backface strain (BFS) gage. All C(T) specimens were compression precracked. Large-crack testing included several compression precracked constant amplitude (CPCA) and compression precracked load reduction (CPLR) tests over a wide range of load ratios (R) . All large-crack tests were monitored using the BFS gage and fatigue crack growth monitoring software. The software recorded stress intensity factor (K), crack length (c), and fatigue crack growth rate (dc/dN) information at regular crack growth intervals. The tests were performed at a frequency of 18Hz and ended when the specimen fractured into two separate pieces; some specimens were fatigued until fracture occurred, while other specimens were statically fractured. By statically fracturing some specimens, data could be gathered pertaining to the fracture behavior of shorter cracks, which is necessary data for fracture data analysis.

5.2.2 Small-Crack Testing

All small-crack tests were performed using single-edge notch bend (SEN(B)) specimens and servo-hydraulic test frames. The pin-holes of all SEN(B) specimens were manually beveled as a way to reduce out-of-plane bending. Specimens were mechanically

polished as part of the machining process. The tests were monitored optically and were stopped at regular intervals for inspection. All small-crack tests were constant amplitude tests performed at a load ratio or R = 0.1. The test ended when the specimen fractured into two separate pieces. Tests were performed at a frequency, ranging between 10 and 18Hz (higher stress level tests were performed at a lower frequency). Data collected during the tests included cycles to specimen failure (N_f) and maximum local notch stress (σ_{max}).

5.3 Data Analysis and Results

During the large-crack constant amplitude tests, ΔK and dc/dN information was collected over a wide range of stress ratios ($R = 0.1$ to 0.95) at fatigue crack growth rates ranging from threshold to fracture.

5.3.1 Constant-Amplitude Loading

CA crack growth rate results can be seen in Figure 5.1. As expected, the data showed a slight spread with a change in stress ratio. Using this data, it was determined that the constraint factor, should not be variable, but set to a constant of $\alpha = 1.3$ for use in the FASTRAN model. Calculations show the $(\Delta K_{eff})_T$ for these specimens is very near fracture, meaning that modeling the fatigue crack growth as constant constraint may not be inappropriate; however, the alarming low constraint factor is of concern, but is expected to be a result of fatigue crack surface roughness.
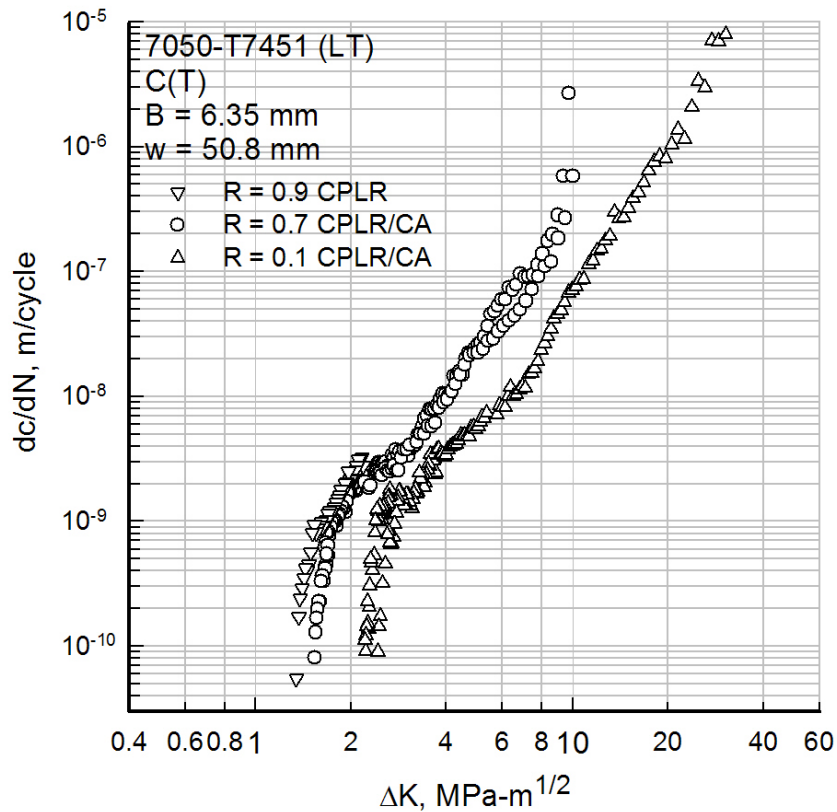
Figure 5.1

ΔK-rate data for the Al7050 C(T) specimens

Using the fatigue crack growth rate information described above, it was possible to collapse the five ΔK-rate curves into one ΔK_{eff}-rate curve and fit a baseline multi-linear curve for use in the FASTRAN model. Local crack closure measurements completed by Yamada [50] have shown that this material shows significant signs of high-R closure, possibly as a result of crack surface roughness. In Figure 5.2, open symbols represent CA test data, which has been adjusted for closure through the typical FASTRAN analysis process; however, the closed symbols represent data adjusted using closure measurements. The

closure measurements resulted in a much lower ΔK values. For this reason the FASTRAN

baseline was fitted to the "closure-free," more conservative curve, which resulted in higher

growth rates and, perhaps, would more accurately model the threshold growth rates found

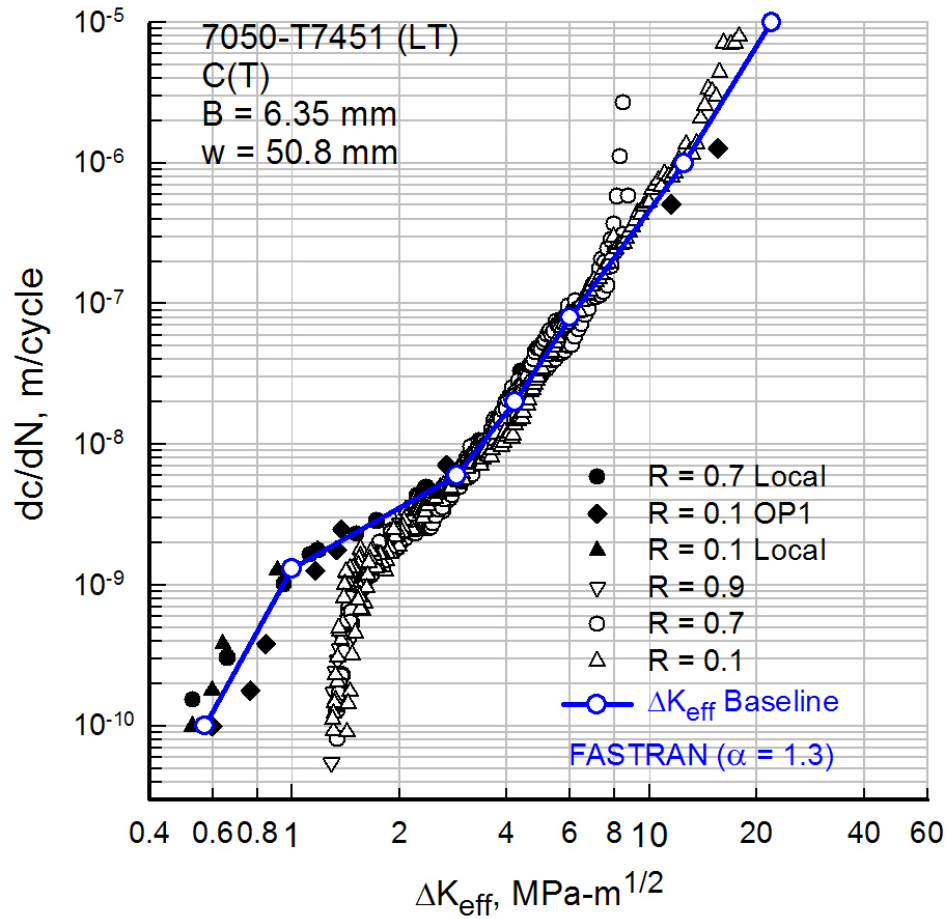in small cracks, where the effects of surface roughness may be minimal.

Figure 5.2

ΔK_{eff}-rate data for the Al7050 C(T) specimens

5.3.2 Small-Crack Results

A common method for expressing the results for small-crack fatigue testing is a stress-life (or S-N) diagram. This type of plot composed of data points each representing the maximum stress applied (in this case the stress at the notch) and the number of cycles the specimen withstood before failure. It was the goal of this work to simulate the small-crack test results with the FASTRAN model using the material characteristics determined from the large-crack tests. The modeling of small, naturally initiated cracks is often modelled in two steps: initiation and propagation. For the sake of the FASTRAN simulation, it was assumed that the number of cycles to crack initiation was negligibly small and, therefore, was not calculated. Instead, the specimens were assumed to contain cracks or initial flaws approximately the size of discontinuities typical of Al7050. Figure 5.3 is a plot of the discontinuity sizes and distribution from Barter et al. [70]. From these discontinuity size results, three equivalent initial flaw sizes (EIFS) were chosen: 4 microns, 12 microns, and 30 microns. FASTRAN fatigue crack growth simulations were performed for each EIFS.
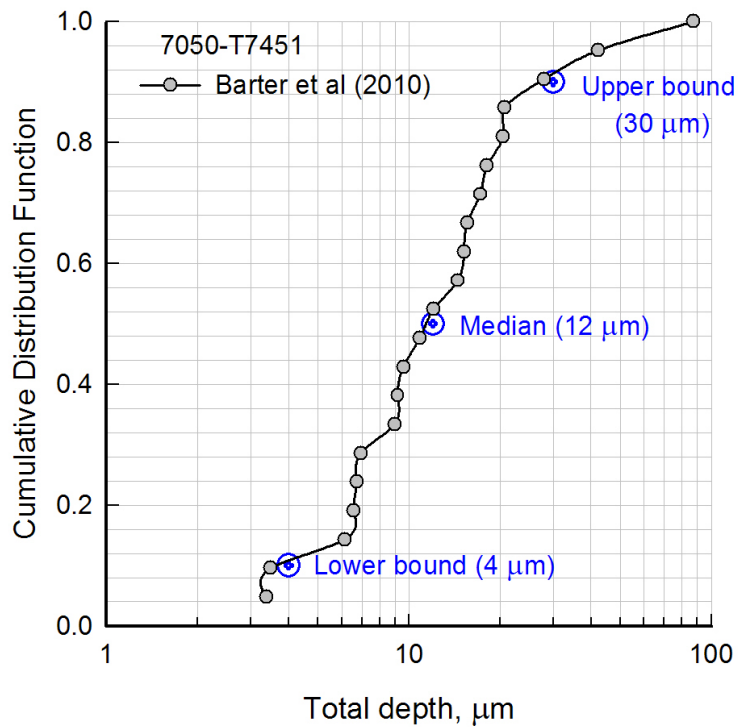
Figure 5.3

7050-T7451 Distribution of Discontinuities in High K_T Specimens [70]

Figure 5.4 shows that FASTRAN simulations using the previously determined EIFS values as initial crack sizes models the CA small-crack fatigue test results quite accurately. The simulation is most accurate for shorter life tests and becomes progressively more conservative as the applied stress decreases. This implies that FASTRAN predicts faster crack growth at lower stresses. This may be a result of having chosen to fit the FASTRAN baseline to the more conservative ("closure-free") data or, perhaps, some mechanism (like debris or roughness) may be slowing the growth rates at lower stress levels.
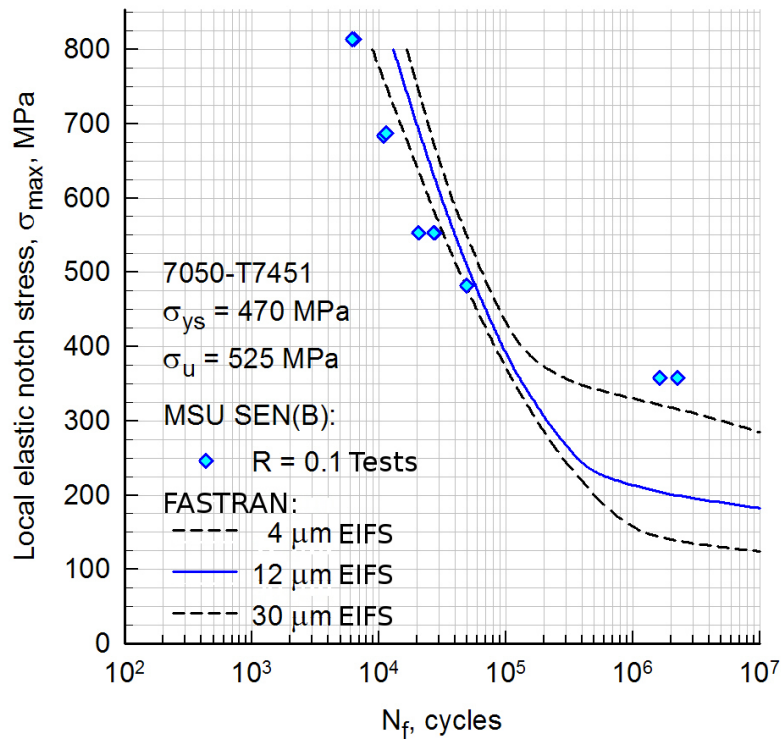
Figure 5.4

Fatigue life results for small-crack tests and FASTRAN fatigue crack growth simulations

To support these findings, fatigue life test data was also acquired from MMPDS [43]. These data were generated open circular hole (K_T = 3.47) specimens and can be found in Figure 5.5 along with the the FASTRAN simulations. These results support the finding that the FASTRAN strip-yield model can accurately model the fatigue life of open hole specimens. Also, because FASTRAN simulations bounded the data set when initial crack sizes were chosen based the distribution of discontinuities [70], it can be inferred that these discontinuities are the sources of crack initiation.
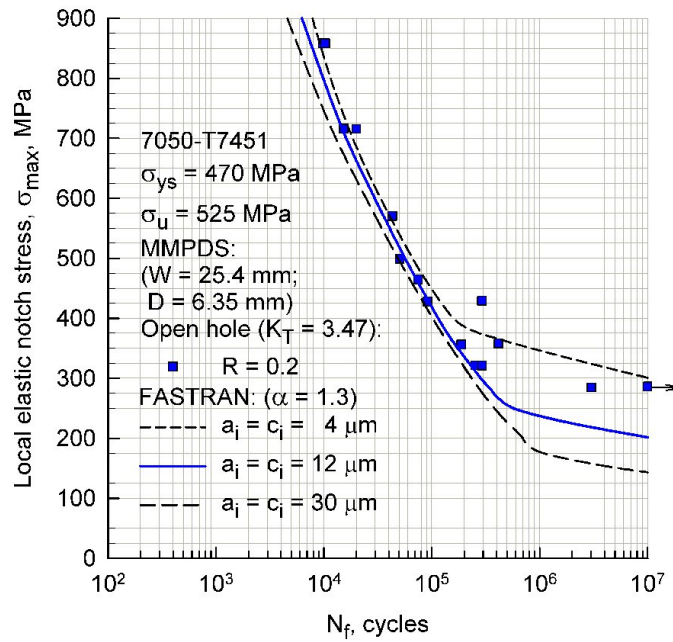
(a) Open hole specimen test with load ratio, R=0.2
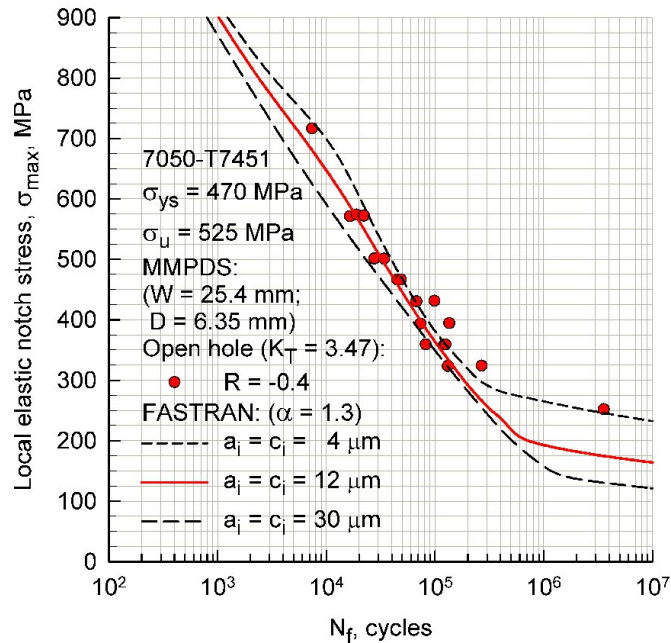
(b) Open hole specimen test with load ratio, R=0.4

Figure 5.5

FASTRAN simulations of open hole specimens

5.4 Conclusions

Large-crack fatigue crack growth testing, small-crack fatigue life testing, and fatigue crack growth analysis performed on Al7050-T7451 has shown that the FASTRAN strip-yield model, using data collected from constant amplitude large-crack tests, can be used to accurately simulate fatigue test results using large-crack data and typical EIFS values. These simulations were based on measured potential crack initiation sites and this practice has been shown to accurately bound most of the scatter associated with fatigue testing.

CHAPTER 6

A LOW-STRENGTH STEEL

Low-strength steel is a common material used for anything from building construction to large construction equipment to shipping containers. Most low-strength steels are characterized by a relatively low yield-stress ($<$400MPa) with a large amount of strain hardening. This characteristic is very desirable in structures where ductile failure provides more safety and the weight of the structure is not a limiting design factor. Many common applications of low-strength steel can be susceptible to failure due to fatigue. Traditionally, fatigue crack growth testing performed on low-strength steel have shown signs of fanning, lower load ratio (R) tests yield lower fatigue crack growth rates for the same effective stress intensity factor range ΔK, in the threshold regime resulting in higher threshold stress intensity factor ranges ΔK_{th} for lower R tests. It has been hypothesized that the cause of this fanning behavior may be found in the standard load reduction test method. In order to test this hypothesis, fatigue crack growth tests were performed in A36 steel at both high and low load ratios.

6.1 Testing

All A36-steel fatigue crack growth tests were performed using the eccentrically loaded, single-edge-notch tension (ESE(T)) specimen monitored using a backface strain (BFS) gage. Although ASTM E-647 [41] provides equations to correlate BFS, K, and crack length (c), the crack monitoring software did not allow the use of these equations. A newly developed (software compatible) equation for correlating backface strain and crack length for the ESE(T) specimen was received via a private communication with Johnston [71]. This equation has the same functional form as the BFS equation for the C(T) specimen with different coefficients and is

$$\frac{c}{w} = A_0 + A_1 U + A_2 U^2 + A_3 U^3 + A_4 U^4 + A_5 U^5 \quad \text{for } 0.1 < c/w < 0.95 \quad (6.1)$$

where c is crack length, w is specimen width, A_0 = 1.007, A_1 = -2.171, A_2 = 1.537, A_3 = -7.615, A_4 = 22.181, and A_5 = -20.745. U is defined as

$$U = \left(\left| \frac{\varepsilon E B w}{P} \right| + 1 \right)^{-1} \quad (6.2)$$

where ε is the backface strain, E is the modulus of elasticity, B is the specimen thickness and P is the applied load. The results of the Johnston [71] equation and results of the ASTM [41] equation can be seen in Figure 6.1(a).

Based on a FADD2D stress analysis of the ESE(T) specimen, a new equation was also developed to correlate K and c. This equation has the same functional form as the K equation for the C(T) specimen with different coefficients and is

$$K = \frac{P}{B\sqrt{w}} \frac{2+\eta}{(1-\eta)^{3/2}} G \tag{6.3}$$

where $\eta = c/w$ and G is

$$G = C_0 + C_1\eta + C_2\eta^2 + C_3\eta^3 + C_4\eta^4 + C_5\eta^5 \qquad \text{for } 0.1 < \eta < 1 \tag{6.4}$$

with $C_0 = 0.5$, $C_1 = 2.643$, $C_2 = $ -6.3, $C_3 = 8.25$, $C_4 = $ -5.6, and $C_5 = 1.59$. Equation results along with the ASTM [41] equation results and Piascik-Newman [72] equation results can be seen in Figure 6.1(b).
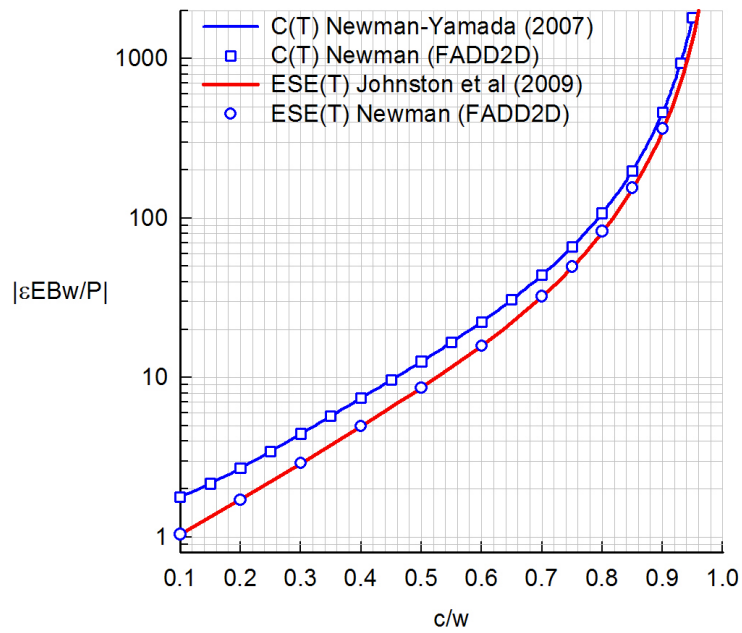
(a) Normalized backface strain equation received via private communication
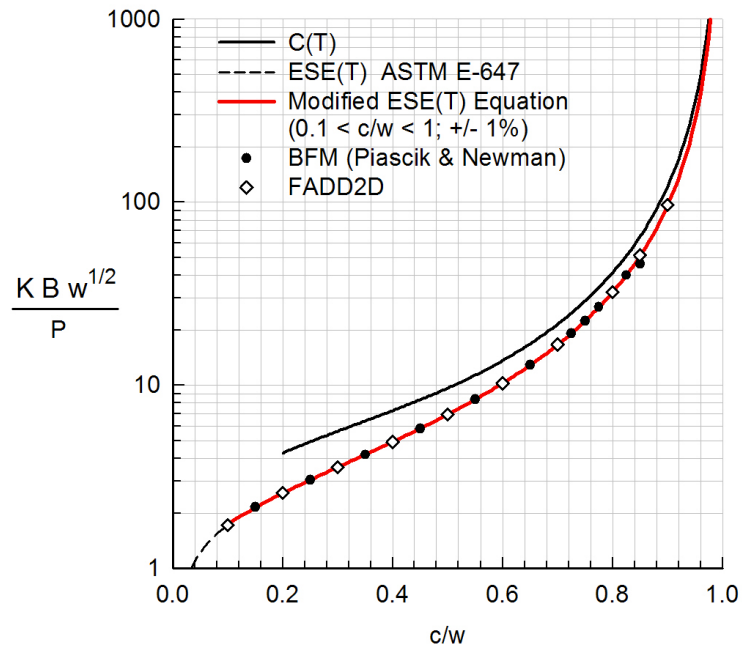
(b) FADD2D results for normalized stress intensity factor were fitted with a new equation

Figure 6.1

Modified stress intensity factor and backface strain equations

All ESE(T) specimens were compression precracked using pin-loading (Fig. 6.2). Because the pins used for loading would be subjected to larger stresses than standard testing loads, hardened steel pins were used for precracking. Before precracking, pin holes were beveled as discussed in Chapter 2 to ensure that the compressive loads induced a minimal bending moment. Normally, the maximum compression load is determined using $K_{cp}/E = 0.01\sqrt{mm}$ [51]; however, because this would have resulted in a very large compressive load (near -17.8kN), which was a safety concern, the equation was modified to $K_{cp}/E = 0.005\sqrt{mm}$. Using the modified equation, the maximum compressive load was determined to be P_{min} = -8900N. The minimum compression load was chosen to be P_{max} = -450N to ensure that the specimen would not move at the minimum load. Specimens were compression precracked for 10,000 cycles at a frequency of 10Hz.

Figure 6.2

The ESE(T) specimens were compression precracked using the pin holes

Two High-R tests were performed at a load ratio of R = 0.7: one CPLR and one CPCA. The remainder of testing was performed at a load ratio of R = 0.1 and consisted of one load shedding test (CPLR) and multiple CPCA tests. Fatigue crack growth rates of these tests were compared to rates from a similar low-strength steel used in the construction of railway tank cars, TC-128B, taken from McKeighan et al. [73].

6.2 Results

The data collected during the high-R tests shows that the standard load shedding procedure and the CPCA procedure yield nearly identical results. When compared with TC-128, a low-strength steel used in the construction of railway tank cars, the A36 high-R test results agreed well with both high-R load shedding and K_{max} test results. Based on the common assumption that the high-R test result is equivalent to the ΔK_{eff} growth curve, FASTRAN was used to predict the threshold behavior of the low-R tests without the effects of threshold fanning. As seen in Figure 6.3, plotting the FASTRAN fatigue crack growth rate results with the low-R load shedding growth rate results from both A36 and TC-128B showed an agreement between the two materials for the high-R tests.

Low-R CPCA testing, however, does not show agreement between crack growth rates from the FASTRAN simulation and the test. The first two CPCA tests show a clear tendency toward a lower threshold and appear to be fitting the FASTRAN prediction. Unfortunately, the third CPCA test yielded strange results (Fig. 6.4). Although the third CPCA test results still display a lower threshold value, the results do not agree with the first two CPCA tests. Further investigation found that a piece of cellophane tape had been accidentally left on one side of the specimen. Although it is most likely safe to assume that the cellophane tape did not carry enough load to alter the test results, the piece of tape had a significant influence on crack growth rates.
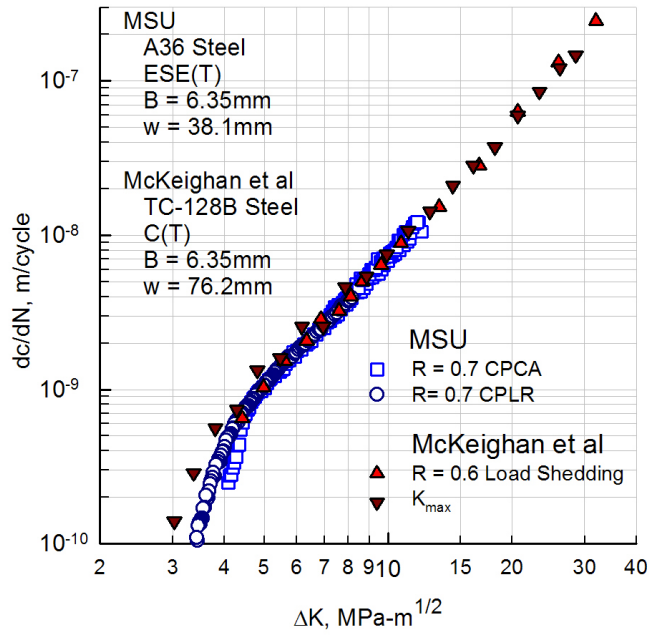
(a) High-R CPCA and ASTM standard load
shedding tests
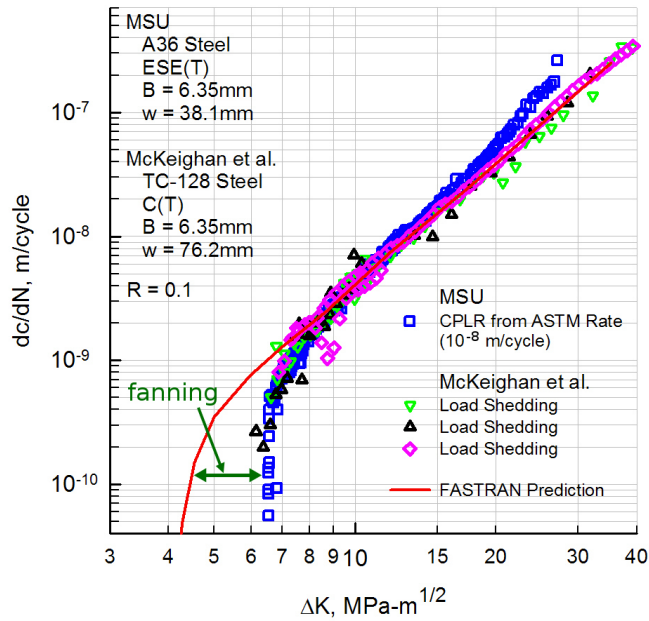
(b) Low-R CPCA and ASTM standard load
shedding tests

Figure 6.3

Large-crack testing fatigue crack growth rate results for A36 Steel
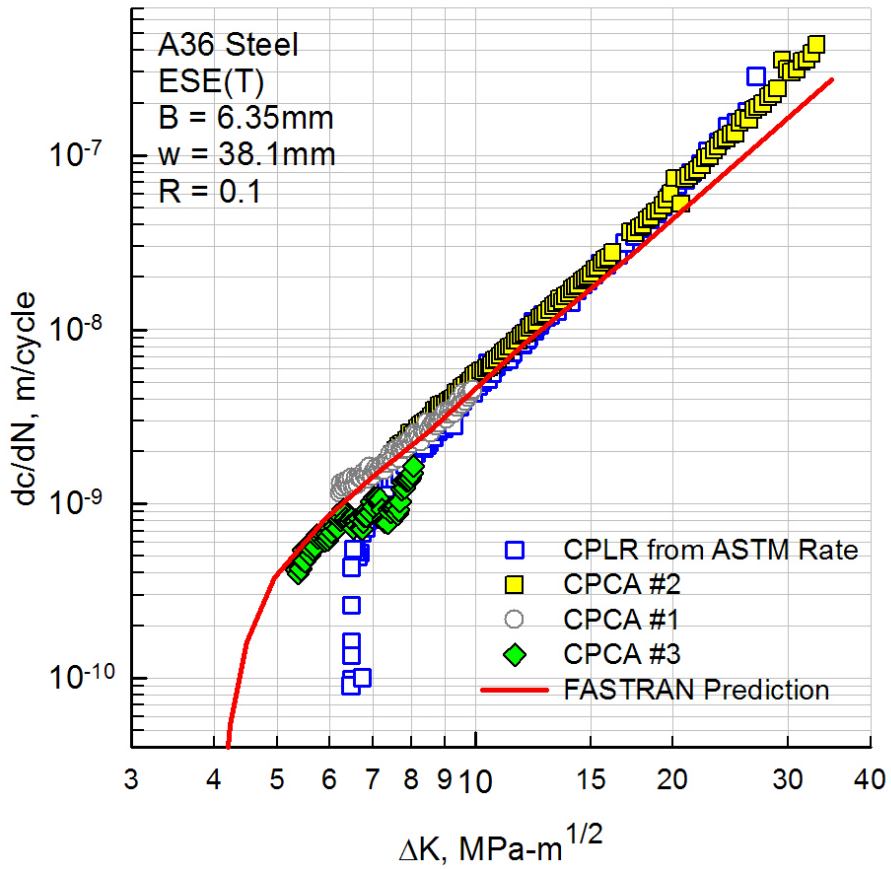
Figure 6.4

Low-R CPCA and standard load reduction test results for A36 Steel

Based on inspection of the fatigue surfaces, oxide debris appears to have built-up in the wake of the crack. Specimens tested without cellophane tape, show very little debris for CPCA tests. Any debris on the fatigue surface of these specimens, collected symmetrically through the specimen thickness. However, the fatigue surface of the specimen tested with the cellophane tape showed a significant build-up of debris on the side of the specimen where the cellophane tape had been left. It has been concluded that the tape-free side allowed debris to exit the crack, but the taped side retained all the debris created during the

crack growth process. As seen in Figure 6.5, the asymmetric presence of debris resulted

in asymmetric crack growth rates through the thickness of the specimen. This gradient in

crack growth rates allowed the crack to grow more quickly on the tape free edge of the

specimen and more slowly on the taped side. Before final plastic collapse, the crack front

had rotated nearly 45 degrees.

(a) A piece of cellophane tape was left on one face of the third
CPCA specimen
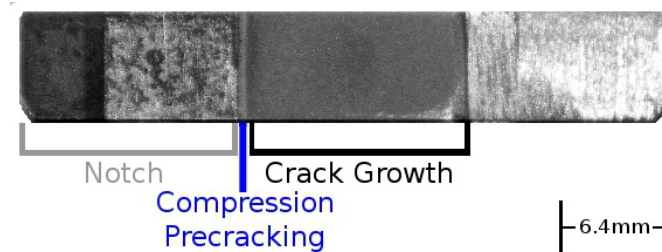
(b) CPCA test performed without cellophane tape
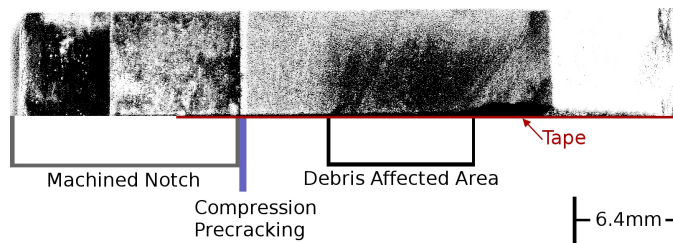
(c) CPCA test performed with cellophane tape left
on one side

Figure 6.5

Effects of debris on fatigue crack growth in A36 Steel

Figure 6.5(b) is a photograph of a low-R CPCA specimen crack surface; the surface is clear of most debris and the crack front is symmetric through the specimen thickness. Figure 6.5(c), however, is a photograph of the crack surface of the specimen that was tested with the tape still attached. The surface is significantly darkened by the presence of debris and the crack front is noticeably asymmetric through the specimen thickness. Figure 6.6 shows a comparison of how the presence of debris on the fatigue surface affects fatigue crack growth rates. The relationship between crack length and crack growth rate for a clean fatigue surface is nearly linear (log scale), while the debris ridden surface shows notable deviations from this linearity. Moreover, the drastic changes in behavior seem to coincide with or follow closely after the noticeable appearance of surface debris. Test number three was repeated (without the tape) and crack growth rate results can be seen in Figure 6.7. The test without cellophane tape yielded higher fatigue crack growth rates for the same ΔK.
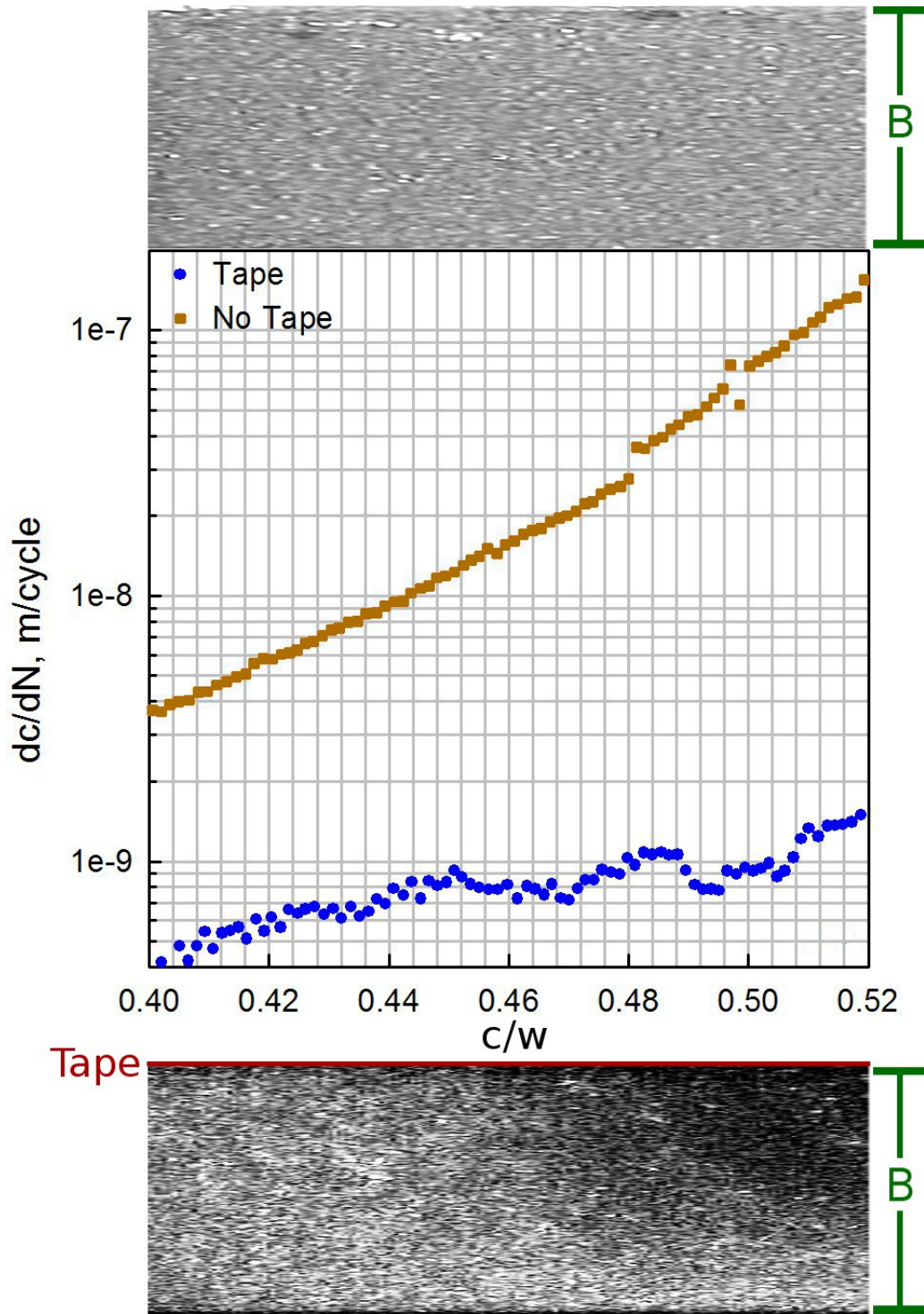
Figure 6.6

The presence of debris on the crack surface corresponds to differences in fatigue crack growth rates
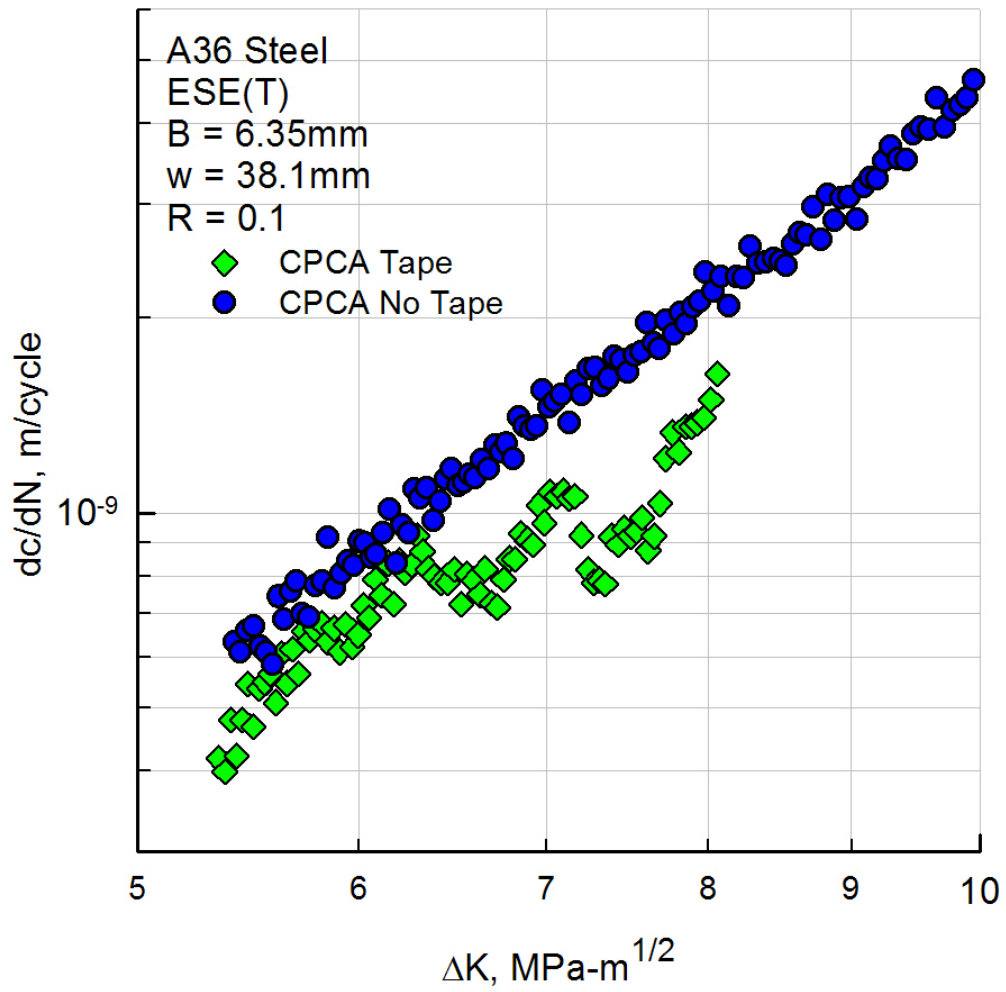
Figure 6.7

Repeated CPCA test without cellophane tape has higher fatigue crack growth rates

Although it seems unlikely that the accumulation of debris on a crack surface could have a significant effect on crack growth behavior, the evidence seems to support the claim. A crack in an ideal elastic body (Fig. 6.8(a)) will close only when the accumulation of debris is excessive (Fig. 6.8(b)), more than will occur in lab air. However, metals are not strictly elastic materials, and therefore, a crack in a metal specimen or structure leaves a region of plasticly deformed material in its wake (Fig. 6.8(c)). In some cases, this wake may cause surface contacts at loads above the minimum applied cyclic load (crack closure). For tests with a load ratio greater than 0.7 ($R > 0.7$), the plasticly deformed material does not lead to surface contacts, but reaches an equilibrium point at which the surface contact load is just below the minimum applied cyclic load. Under this circumstance, the addition of a thin layer of debris may be enough to cause the crack to close, as seen in Figure 6.8(d). For test with lower load ratios, $R = 0.1$ as is the case here, the thin layer of debris causes the surface contact to occur sooner. The asymmetric distribution of debris found on the taped specimen led to asymmetric closure and crack growth rates.
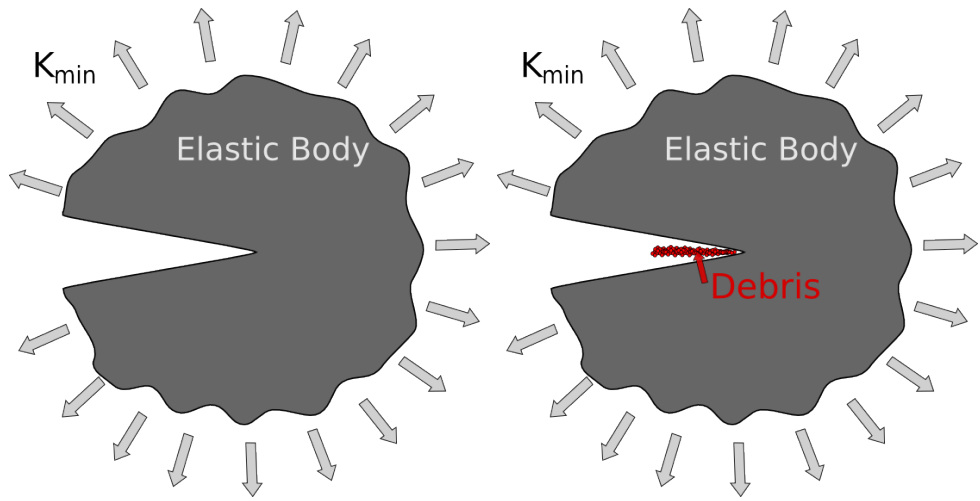
(a) Elastic body alone does not close

(b) Elastic body with debris does not close
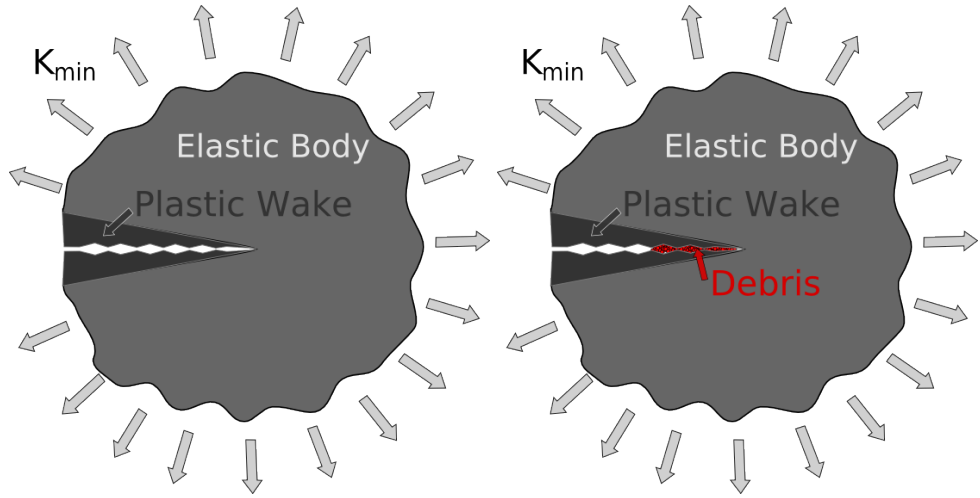
(c) Elastic body with plastic wake does not close for high load ratios

(d) Elastic body with plastic wake and debris may close even for high load ratios

Figure 6.8

Debris on the crack surface can cause crack closure

6.3 Conclusions

The tests performed indicate that there is a fanning behavior found in the threshold region of low-R load reduction tests, which cannot be explained through plasticity alone. Also, this behavior is significantly less prevalent, sometimes non-existent, in K-increasing tests (CPCA). Finally, this material was found to accumulate debris on the crack surface, which can lead to premature surface contacts and reduced growth rates or even arrest crack growth. Although most of this debris is removed from the crack surface by the cyclic action of the specimen, more debris appears to accumulate in K-decreasing tests (CPLR). It can, therefore, be concluded that one potential cause for the fanning behavior is the presence of debris.

Because models like FASTRAN are based entirely on plasticity theory and ignore the effects of debris, this phenomenon cannot be properly predicted. It is for this reason that research needs to be done on the subject of debris accumulation, and the current models should be adjusted to determine the effects of debris build-up. The tendency for some tests to promote the accumulation of debris can result in inflated threshold stress intensity values (ΔK_{th}) and unsafe structures. If debris accumulation is a result of crack surface oxidation, structures with interior crack initiations will exhibit much lower threshold values and much higher crack growth rates and may lead to unexpected fatigue failures.

CHAPTER 7

A HIGH-STRENGTH STEEL

Although it is common to think of aircraft as being built with aluminum alloys, high-strength steel, because of its relatively high modulus of elasticity and yield stress, is often found in aircraft structural components that will experience high stresses. For example, components in landing gear are often constructed of high-strength steel. The elevated hardness of heat treated steels make them even more appropriate for high-stress aircraft components; however, an unfortunate side effect of an increase in hardness is a decrease in toughness. It is important, therefore, to be familiar with the fatigue and fracture characteristics of high-strength steels, especially those used in components that are difficult to inspect regularly.

Large- and small-crack testing was performed on a high-strength steel, 9310. The data collected was used to generate a material model for use in the FASTRAN strip-yield model. The purpose of this suite of tests and the following analysis was to generate the data required to accurately model the fatigue crack growth behavior of this engineering material. To help support the findings, additional small-crack data was found in the literature. After testing and analysis were completed, the tests were simulated using FASTRAN to validate that the model could, within acceptable accuracy, duplicate the test results for fatigue life and fatigue crack growth.

7.1 Material

9310 steel is a heat-treated, hardened, high-strength steel. The process of heat treating the material is elaborate and includes annealing at very high temperatures (above 830° C) followed by room air cooling and then extreme cold exposure (below -80° C). After treatment and tempering, the material has a ultimate strength of σ_u = 1070MPa, a yield strength of σ_{ys} = 896 MPa, and an elongation at failure of 15%. This heat treated material was machined into w = 76.2mm compact (C(T)) specimens and w = 25.4mm single edge notch bend (SEN(B)) specimens for testing.

7.2 Testing

All tests were conducted at Mississippi State University on a 25 kN servo-hydraulic load frame operated through the aid of a steady-state and variable-amplitude fatigue-crack-growth software. Crack lengths were measured visually with a traveling microscope and digitally with a backface strain (BFS) gage. The testing of 9310 Steel was divided into two regimes: large-crack and small-crack testing. The large-crack testing procedure yielded fatigue crack growth and fracture information. Alternatively, the small-crack testing procedure yielded crack initiation, crack length, and fatigue life information.

7.2.1 Large-Crack Testing

All large-crack testing for 9310 steel was performed using w = 76.2mm compact (C(T)) specimens. The pin-holes of all steel C(T) specimens were beveled as part of the machining process. The C(T) specimens were manually polished to 1 micron to facilitate

optical crack measurements. These optical measurements were used to verify the accuracy of crack lengths calculated through the use of a BFS gage. All 9310 steel C(T) specimens were compression precracked. Large-crack testing included compression precracked load reduction (CPLR) tests over a wide range of load ratios (R) and one spike overload (OL) test. All large-crack tests were monitored using the BFS gage and fatigue crack growth software. The software recorded stress intensity factor (K) and fatigue crack growth rate (dc/dN) information at regular crack growth intervals. The tests were performed at a frequency of 18Hz and ended when the specimen fractured into two separate pieces; some specimens were fatigued until fracture occurred, while other specimens were statically fractured.

Spike OL testing was an integral part of the large-crack testing battery. The spike OL test began as a CPCA test and was stopped at a given crack length, at which time a load greater than the cyclic maximum was applied. The test was then returned to constant amplitude loading; this process was repeated throughout the life of the specimen. After the OL was applied, dc/dN momentarily increased and then decreased drastically because of the region of plastic deformation in front of the crack tip. Characterizing this behavior was necessary for creating an accurate material model and determining the proper constraint factor, α.

7.2.2 Small-Crack Testing

All small-crack tests were performed using single-edge notch bend (SEN(B)) specimens and servo-hydraulic test frames. The pin-holes of all steel SEN(B) specimens were

manually beveled as a way to reduce out-of-plane bending. Specimens were electro-chemically polished as an attempt to relieve residual stresses introduced during the machining process. Unfortunately, as a result of the electro-chemical polishing, some specimens became discolored and streaked; however, the notches themselves showed no marks or streaks as a result of the electro-chemical polishing. The tests were monitored optically and were stopped at regular intervals for inspection. All small-crack tests were constant amplitude tests performed at a load ratio of $R = 0.1$. The test ended when the specimen fractured into two separate pieces. Tests were performed at a frequency, ranging between 10 and 18Hz (higher stress level tests were performed at a lower frequency).

The definition of "small crack" is often a topic of argument among fatigue professionals. However, most agree that small cracks are about the size of the grains for the given material. These cracks are very small and are often measured using a replica method: the test is stopped at regular intervals and replica is made of the notch. These replicas can be inspected through a microscope and the imprints of cracks can be measured. The replica compounds that are available for this type of data gathering can be expensive, difficult, and time consuming; also, the compounds typically have a shelf life of only a few weeks. For this work, however, it was decided that the replica method would not be used due to time constraints and cost. Instead, the tests were stopped at regular intervals and the notch surface was inspected using a travelling microscope. As a result, the data collected during tests did not include measured crack sizes that could be called "small." However, because the cracks were naturally initiated, the tests results do reflect the overall growth behavior of small cracks.

7.3 Data Analysis and Results

During the large-crack CA tests, ΔK and dc/dN information was collected over a wide range of stress ratios (R = 0.1 to 0.95) at fatigue crack growth rates ranging from threshold to fracture. Using this data, it was possible to calculate an appropriate constraint values, α_1 and α_2, for use in the FASTRAN model. As stated previously, CA testing is not sufficient for determining constraint values. For this reason a multiple-spike OL test was performed. OL test data was used to better determine the constraint values for the model.

7.3.1 Constant-Amplitude Loading

CA test results can be seen in Figure 7.1. As expected, the data showed a consistent spread with a change in stress ratio. Using spike OL results combined with CA results, it was determined that for rates below 10^{-7} m/cycle, $\alpha_1 = 2.5$ and for rates above 10^{-5} m/cycle, $\alpha_2 = 1.15$. For growth rates between 10^{-7} and 10^{-5} m/cycle, a log relationship is used to calculate α. These values match the characteristically high constraint factors often used when modeling steels.
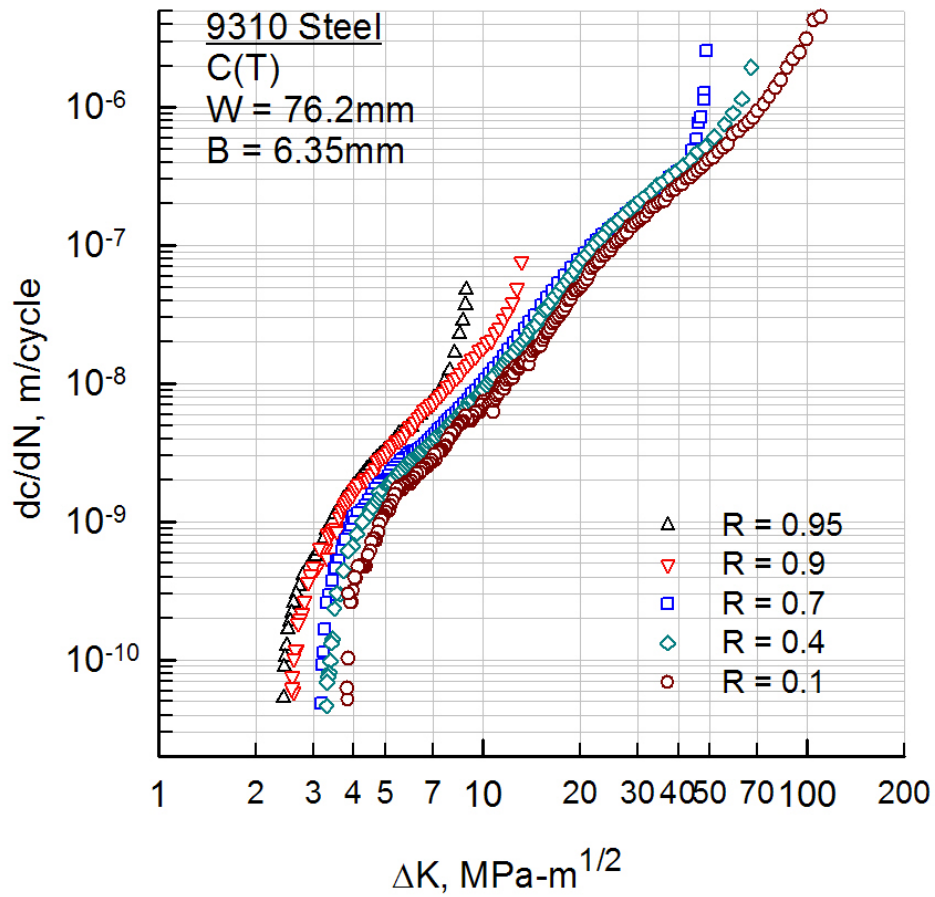
Figure 7.1

ΔK-rate data for the 9310 steel C(T) specimens

Using this information, it was possible to collapse the five ΔK-rate curves into one ΔK_{eff}-rate curve and fit a baseline multi-linear curve for use in the FASTRAN model (Fig. 7.2). Because the threshold region of the ΔK_{eff}-rate curve showed a noticeable spread, the FASTRAN baseline was fitted to the more conservative curve, which matched the data from the higher stress ratio tests and resulted in more conservative growth rates.

Figure 7.2

ΔK_{eff}-rate data for the 9310 steel C(T) specimens

7.3.2 Spike Overload

The multiple-spike OL test served two purposes: (1) a source of information necessary for determining the proper constraint values and (2) as a way to validate the FASTRAN model for large cracks. As seen in Figure 7.3, using the FASTRAN model with the previously discussed baseline curve and variable constraint factors, it was possible
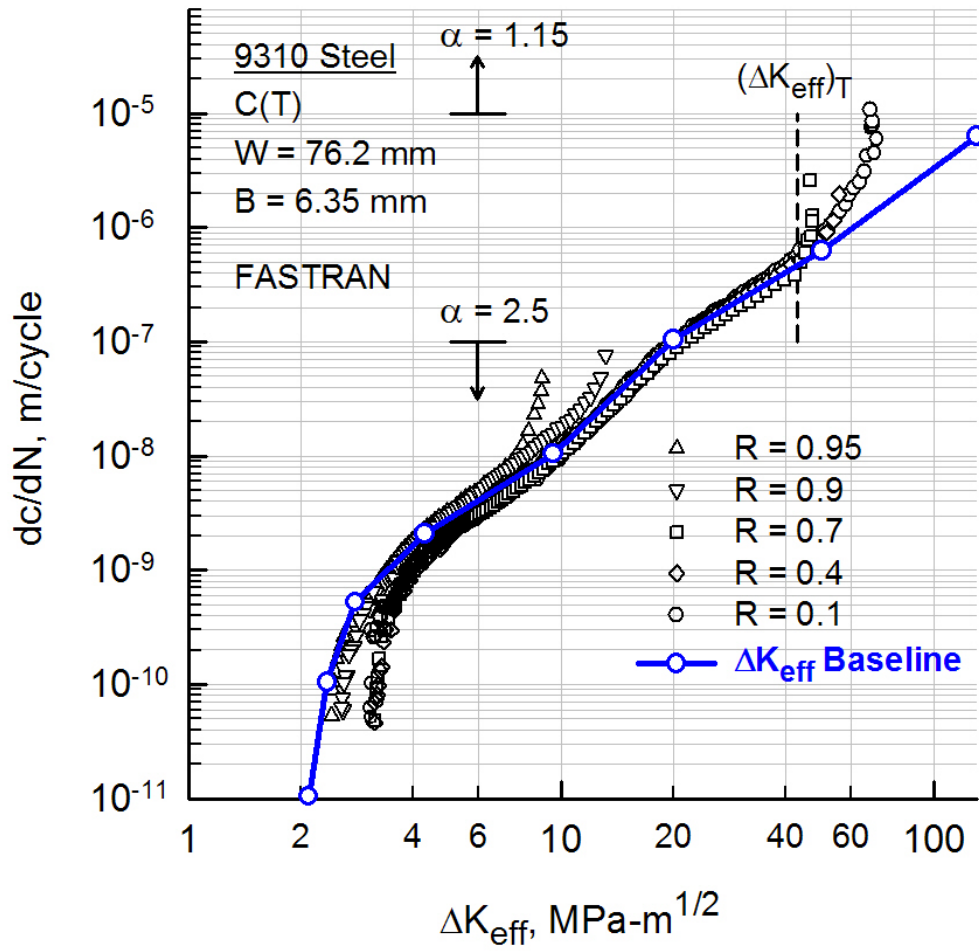
to simulate the acceleration and retardation of crack growth rate resulting from each OL. Figure 7.4 shows the rates calculated by FASTRAN during the multiple-spike OL test. This indicates that the FASTRAN results are accurate when modeling the cause of growth rate changes and not just the effects.
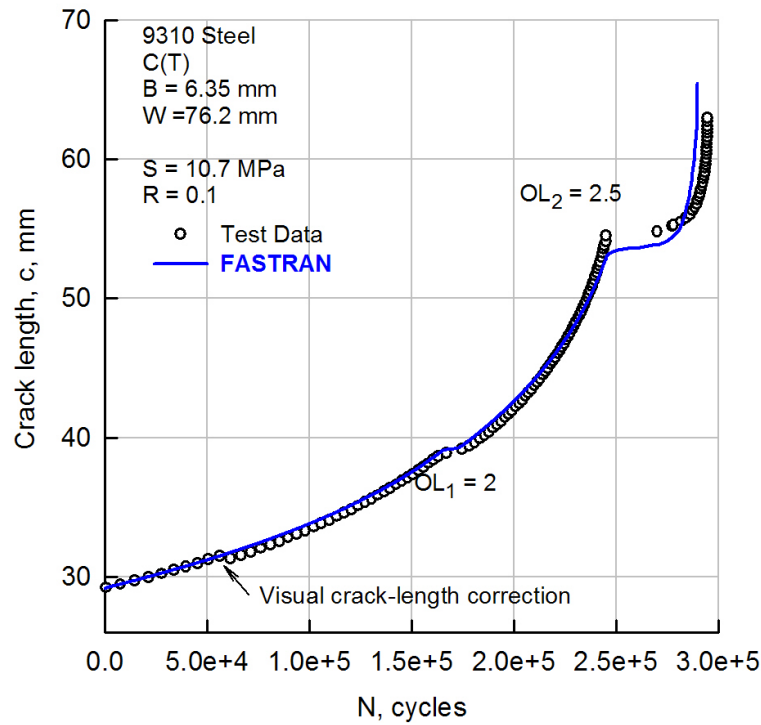

Figure 7.3

Crack length results from multiple-spike overload test on 9310 steel C(T) specimen

7.3.3 Small-Crack Results

A common method for expressing the results for small-crack fatigue testing is a stress-life diagram. This type of plot is composed of data points each representing the
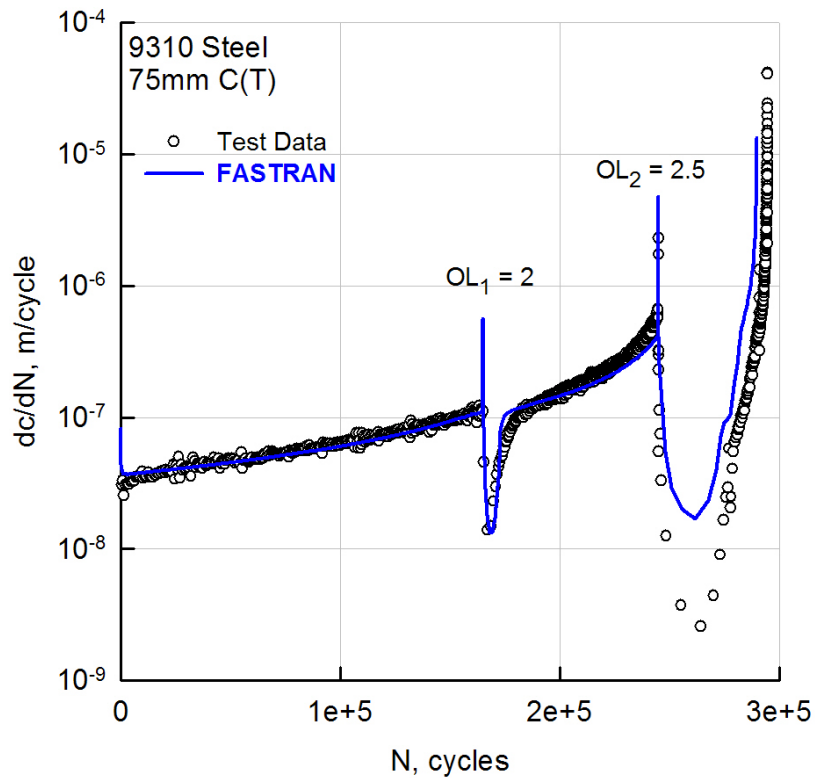
Figure 7.4

Crack growth rates from multiple-spike overload test on a 9310 steel C(T) specimen

maximum stress (in this case the stress at the notch, σ_{max}) and the number of cycles the

specimen withstood before failure. It was the goal of this work to simulate the small-crack

test results in such a format with the FASTRAN model using the material characteristics

determined from the large-crack tests. The modeling of small, naturally initiated cracks is

often modelled in two stages: initiation and propagation. For the sake of the FASTRAN

simulation, it was assumed that the number of cycles to crack initiation was negligibly

small and, therefore, was not calculated. Instead, the FASTRAN model used assumed an

equivalent initial flaw size (EIFS) in the material determined through trial-and-error.

To determine the appropriate EIFS, stress-life data was also acquired from Liu et al [44]. This stress-life data was generated using single edge notch tension (SEN(T)) specimens and can be found in Figure 7.5 along with the FASTRAN simulation for the SEN(T) specimens. These results show that using an EIFS of 6 microns (i.e. $6 \cdot 10^{-6}$ m) models the test results quite accurately. The calculation is most accurate for shorter life tests and becomes progressively more conservative as the applied stress decreases. This implies that FASTRAN predicts faster crack growth near the endurance limit region. This region corresponds to the threshold region on a ΔK_{eff}-rate basis. This may be a results of having chosen to fit the FASTRAN baseline to the more conservative data or, perhaps, some mechanism (like debris) may be slowing the growth rates at lower stress ratio levels (see Fig. 7.2). The same 6 micron EIFS was applied for the simulation of SEN(B) small-cracks. Stress-life results from the FASTRAN simulation can be found in Figure 7.6. The FASTRAN simulation yields more accurate results for higher load tests, but simulation results for lower load tests predict early fracture.
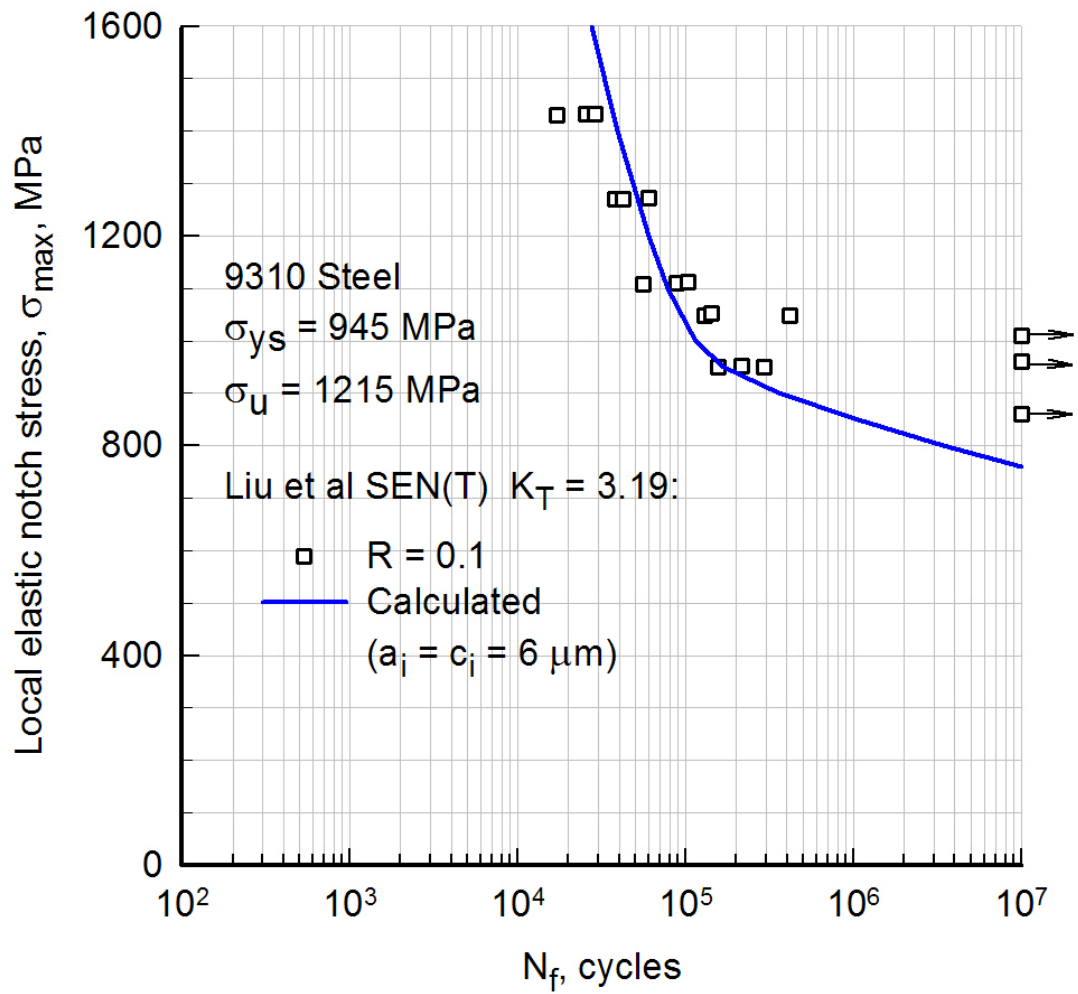
Figure 7.5

SEN(T) stress-life results and FASTRAN model results for 9310 steel small-cracks
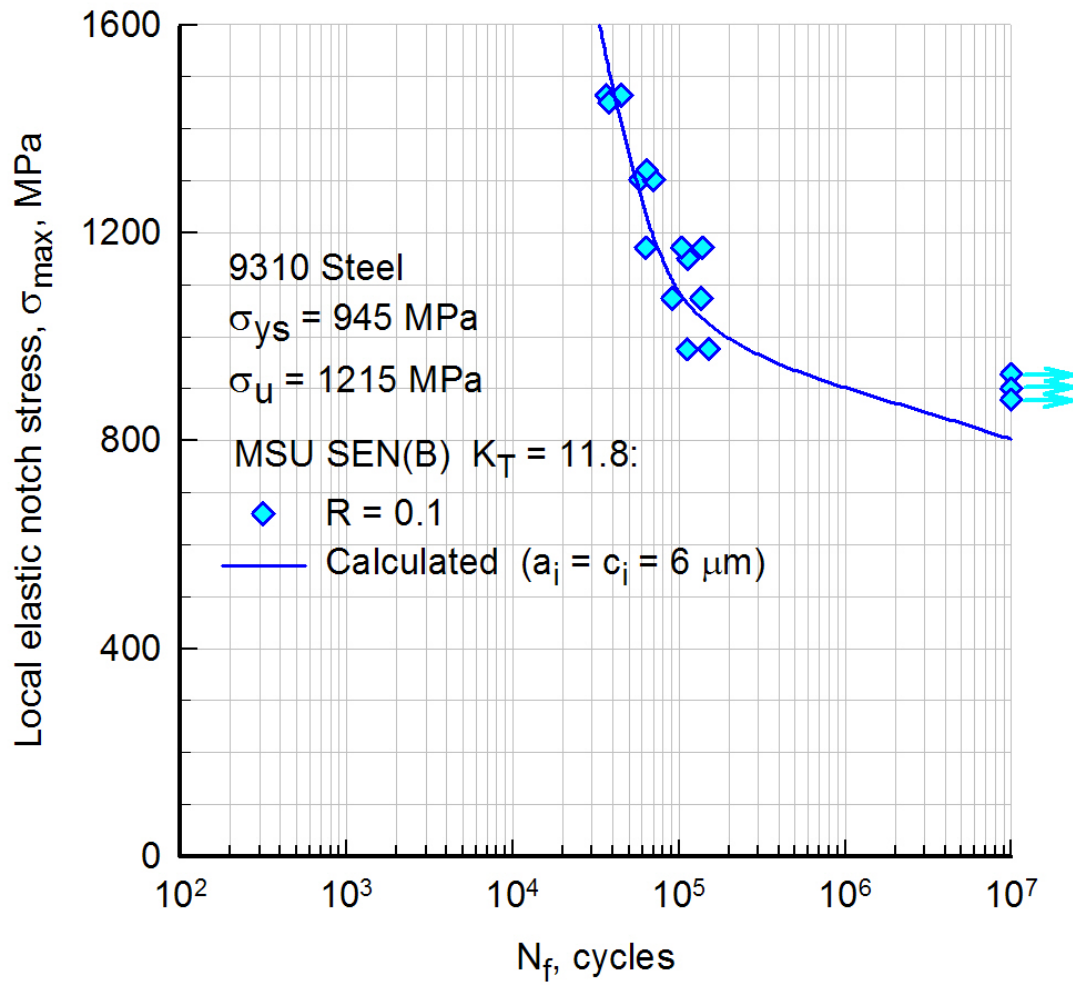
Figure 7.6

SEN(B) stress-life results and FASTRAN model results for 9310 steel small-cracks

These results support the finding that the FASTRAN strip-yield model can accurately model the fatigue life of small-crack specimens; however, it was of interest to know if the FASTRAN model accurately simulates crack lengths against cycles. During some of the small-crack tests, the test was stopped at regular intervals and the notch was inspected under mean load for any cracks that may have initiated along the surface. When found, these cracks would be monitored and their surface crack lengths would be measured. FASTRAN was then used to model the growth of a crack starting from the previously mentioned 6 microns under constant amplitude loads. The normalized crack length $(2a/B)$ results of these simulations and test results can be found in Figure 7.7. The FASTRAN simulation most accurately modeled the crack growth behavior for the highest applied load (σ_{max} = 1464MPa). For other applied loads, the simulation modeled crack growth behavior very well with the lowest load test (σ_{max} = 1464MPa) having the greatest error, around 40%.
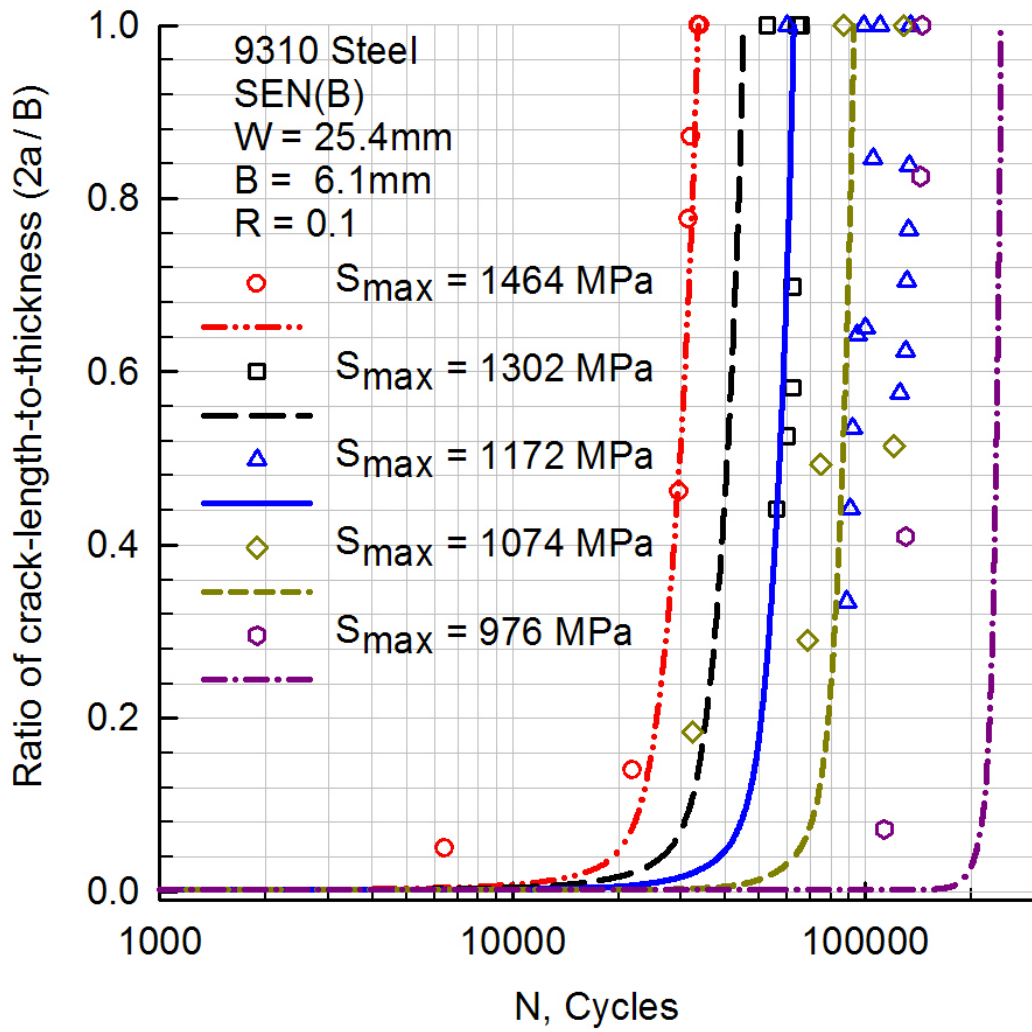
Figure 7.7

Surface crack lengths measured through optical inspections of SEN(B) small-crack tests

7.4   Conclusions

Testing and analysis has shown that the FASTRAN strip-yield model, using data collected from constant amplitude and spike OL tests, can be used to accurately simulate multiple-spike OL fatigue crack growth testing in a high-strength steel, 9310. Also, the data collected has been used to model high- and low-cycle fatigue as fatigue crack growth on the SEN(B) and SEN(T) small-crack specimens with FASTRAN. The small-crack simulation results have been shown to be exceptionally accurate for both fatigue life and crack size determination.

CHAPTER 8

CLOSING REMARKS

In summary, this work describes the efforts to test and characterize four engineering materials — a low-strength aluminum alloy, a high-strength aluminum alloy, a low-strength steel, and a high-strength steel. Testing performed included large-crack and small-crack testing using SEN(B), ESE(T), and C(T) specimens. Much of the fatigue crack growth test data was used to develop a material description sufficient to model the fatigue and fracture behavior of the material using FASTRAN, a strip-yield model based on the modified Dugdale model. To facilitate the testing and analysis, two-dimensional stress analysis was also performed on multiple specimen configurations to determine equations for correlation of crack length (c), stress intensity factor (K), and backface strain (BFS) equations.

8.1 Conclusions

The FASTRAN fatigue crack growth model can be used to accurately simulate fatigue crack growth rates and crack lengths for large-crack constant amplitude and spike overload tests. Moreover, FASTRAN can be used to accurately simulate fatigue life for small-crack constant amplitude tests, a regime of fatigue often relegated to empirical models. For the 9310 steel small-cracks, FASTRAN has been shown to accurately simulate crack lengths against cycles for small-crack tests. By assuming that engineering materials

contain flaws or discontinuities, often the result of particles purposely included in the material for some benefit like stiffness or hardness, it can be assumed that crack initiation occurs within the first few cycles. Assuming that the initial crack size is the particle or flaw size, FASTRAN can be used to predict fatigue life.

In order to create accurate material models for the FASTRAN simulations, it was necessary to collect accurate data. Unfortunately, some testing techniques yield data that suggests drastically different crack growth behavior when compared with than other test techniques. It has been shown that the present standard for threshold testing yields data that is less conservative and less consistent than the data yielded through CPCA and CPLR tests. This is not to say that CPLR is a perfect test or that CPCA cannot be improperly applied and result in a data set that is even less conservative than the ASTM standard load shedding test. For this reason, the CPCA and CPLR testing techniques should be added to the ASTM standard.

The effects of surface debris cannot be ignored. It has been shown that the presence of debris on a crack surface can result in significant changes in crack growth rate, crack-front geometry, and even the validity of test data. Also, the beveling of pin holes to reduce any out-of-plane bending is considerably influential on the crack-front geometry and should become a standard procedure. This would be best carried out during the machining process to ensure consistency.

8.2 Future Work

Although FASTRAN appears to accurately simulate the behavior of most constant amplitude tests and some simple variable amplitude tests, it is important to realize that very few actual engineering structures experience such simplified cyclic loads in application. For this reason, it is important that this work be continued with investigations into spectrum loading sequences. The ability to accurately and consistently predict the fatigue behavior of specimens exposed to a standard spectrum of cyclic loads is limited to only a few spectra and a few materials.

In order to better understand the effects of spectrum loading, it is important to clearly understand the behavior of a given material in the threshold regime. This understanding is presently limited by the absence of information on the effect that debris has on the growth of cracks in metals. Models such as FASTRAN need to be adapted to account for the added complexity of surface debris. Highly reactive materials, like A36 steel, and materials that often produce rough fracture surfaces, like 7050 aluminum alloy, are an excellent place to start the study of crack growth behavior not governed by plasticity only.

REFERENCES

[1] Anderson, T. L., *Fracture Mechanics: Fundamentals and Applications*, CRC Press, Boca Raton, FL, 3rd ed., 2005.

[2] Inglis, C. E., "Stresses in a Plate due to the Presence of Cracks and Sharp Corners," Institution of Naval Architects, 1913.

[3] Griffith, A. A., "The Phenomena of Rupture and Flow in Solids," *Philosophical Transactions, Series A*, Vol. 221, 1920, pp. 163–241.

[4] Irwin, G. R., "Fracture Dynamics," *Fracturing of Metals*, American Society for Metals, Cleveland, OH, 1948, pp. 147–166.

[5] Westergaard, H. M., "Bearing Pressures and Cracks," *Journal of Applied Mechanics*, Vol. 6, 1939, pp. 49–53.

[6] Irwin, G. R., "Analysis of Stresses and Strains near the End of a Crack," *Journal of Applied Mechanics*, Vol. 24, 1957, pp. 361–364.

[7] Williams, M. L., "The Bending Stress Distribution at the Base of a Stationary Crack," *Journal of Applied Mechanics*, Vol. 24, No. 1, 1957, pp. 109–114, Translated ASME.

[8] Wells, A. A., "The Conditions of Fast Fracture in Aluminum Alloys with Particular Reference to Comet Failures," Report, British Welding Research Association, April 1955.

[9] Winne, D. H. and Wundt, B. M., "Application of the Griffith-Irwin Theory of Crack Propagation to the Bursting Behavior of Disks, Including Analytical and Experimental Studies," *Transactions of the American Society of Mechanical Engineers*, Vol. 80, 1958, pp. 1643–1655.

[10] Irwin, G. R., "Plastic Zones Near a Crack and Fracture Toughness," *Sagamore Research Conference Proceedings*, Vol. 4, Syracuse University Research Institute, Syracuse, NY, 1961, pp. 63–75.

[11] Dugdale, D. S., "Yielding in Steel Sheets Containing Slits," *Journal of the Mechanics and Physics of Solids*, Vol. 8, 1960, pp. 100–104.

[12] Barenblatt, G. I., "The Mathematical Theory of Equilibrium in Brittle Fracture," *Advances in Applied Mechanics*, Vol. VII, Academic Press, 1962, pp. 55–129.

[13] Wells, A. A., "Unstable Crack Propagation in Metals: Cleavage and Fast Fracture," *Proceedings of the Crack Propagation Symposium*, Vol. 1, Paper 84, Cranfield, UK, 1961.

[14] Rice, J. R., "A Path Independent Integral and the Approximate Analysis of Strain Concentration by Notches and Cracks," *Journal of Applied Mechanics*, Vol. 35, 1968, pp. 379–386.

[15] Hutchinson, J. W., "Singular Behavior at the End of a Tensile Crack Tip in a Hardening Material," *Journal of Mechanics and Physics of Solids*, Vol. 16, 1968, pp. 13–31.

[16] Rice, J. R. and Rosengren, G. F., "Plane Strain Deformation near a Crack Tip in a Power-Law Hardening Material," *Journal of Mechanics and Physics of Solids*, Vol. 16, 1968, pp. 1–12.

[17] Shih, C. F. and Hutchinson, J. W., "Fully Plastic Solutions and Large-Scale Yielding Estimates for the Plane Stress Crack Problems," *Journal of Engineering Materials and Technology*, Vol. 98, 1976, pp. 289–295.

[18] Kumar, V., German, M. D., and Shih, C. F., "An Engineering Approach for Elastic-Plastic Fracture Analysis," EPRI Report NP-1931, Electric Power Research Institute, Palo Alto, CA, 1981.

[19] Burdekin, F. M. and Dawes, M. G., "Practical Use of Linear Elastic and Yielding Fracture Mechanics with Particular Reference to Pressure Vessels," *Proceedings of the Institute of Mechanical Engineers Conference*, London, UK, May 1971, pp. 28–37.

[20] Peterson, R. E., "Discussion of a Century Ago Concerning the Nature of Fatigue and a Review of Some of the Subsequent Researches Concerning the Mechanism of Fatigue," *ASTM Bulletin No. 164*, 1950, pp. 50–56.

[21] Stephens, R. I., Fatemi, A., Stephens, R. R., and Fuchs, H. O., *Metal Fatigue in Engineering*, John Wiley and Sons, Inc., 2nd ed., 2001.

[22] "Wohler's Experiments on the Strength of Metals," *Engineering*, August 1867, pp. 160–161.

[23] Bauschinger, J., "On the Change of the Position of the Elastic Limit of Iron and Steel Under Cyclic Variations of Stress," *Mitt. Mech.-Tech. Lab., Munich*, Vol. 13, No. 1, 1886.

[24] Ewing, J. A. and Humphrey, J. C. W., "The Fracture of Metals Under Repeated Alterations of Stress," *Phil. Trans. Roy. Soc., London*, Vol. CC, 1903, pp. 241–250.

[25] Basquin, O. H., "The Experimental Law of Endurance Tests," *Proceedings*, Vol. 10, Part II, ASTM, 1910, pp. 625–630.

[26] Gough, H. J., *The Fatigue of Metals*, Scott, Greenwood and Son, London, 1924.

[27] Moore, H. F. and Kommers, J. B., *The Fatigue of Metals*, McGraw-Hill Book Co., New York, 1927.

[28] Haigh, B. P., "The Relative Safety of Mild and High-Tensile Alloy Steels Under Alternating and Pulsating Stresses," *Proceedings*, Vol. 24, Institute for Automobile Engineering, 1929/1930, pp. 320–347.

[29] Almen, J. O. and Black, P. H., *Residual Stresses and Fatigue in Metals*, McGraw-Hill Book Co., New York, 1963.

[30] Horger, O. J. and Maulbetsch, T. I., "Increasing the Fatigue Strength of Press Fitted Axle Assemblies by Cold Rolling," *Trans. ASME*, Vol. 58, 1936, pp. A91.

[31] Miner, M. A., "Cumulative Damage in Fatigue," *Trans. ASME, Journal of Applied Mechanics*, Vol. 67, 1945, pp. A159–A164.

[32] Peterson, R. E., *Notch Sensitivity*, Metal Fatigue, ed. G. Sines and J. L. Waisman, McGraw-Hill Book Co., New York, 1959, pp. 293–306.

[33] Peterson, R. E., *Stress Concentration Design Factors*, John Wiley and Sons, New York, 1953.

[34] Peterson, R. E., *Stress Concentration Factors*, John Wiley and Sons, New York, 1974.

[35] Weibull, W., "A Statistical Distribution Function of Wide Applicability," *Journal of Applied Mechanics*, September 1951, pp. 293–297.

[36] Paris, P. C., Gomez, M. P., and Anderson, W. F., "A Rational Analytical Theory of Fatigue," *Trend. Eng.*, Vol. 13, No. 9, 1961, pp. 9–14.

[37] Schijve, J. and Broek, D., "Crack Propagation Tests Based on a Gust Spectrum with Variable Amplitude Loading," *Aircraft Engineering*, Vol. 34, 1962, pp. 314–316.

[38] Elber, W., "Fatigue Crack Closure under Cyclic Tension," *Engineering Fracture Mechanics*, Vol. 2, 1970, pp. 37–45.

[39] Paris, P. C., "Testing for Very Slow Growth of Fatigue Cracks," *Closed Loop*, Vol. 2, No. 5, 1970.

[40] Schmidt, R. A. and Paris, P. C., *Threshold for Fatigue Crack Propagation and the Effects of Load Ratio and Frequency*, ASTM STP 536, Philadelphia, PA, 1973, pp. 79–94.

[41] *ASTM-647 — Standard Test Method for Measurement of Fatigue Crack Growth Rates*, Annual Book of ASTM Standards, American Society of Testing and Materials, West Conshohocken, PA, 2008.

[42] Schijve, J., Skorupa, M., Skorupa, A., Machniewicz, T., and Gruszczynski, P., "Fatigue Crack Growth in the Aluminum Alloy D16 under Constant and Variable Amplitude Loading," *international Journal of Fatigue*, Vol. 26, 2004, pp. 1–15.

[43] *Metallic Materials Properties Development and Standardization*, Office of Aviation Research, Washington, DC 20591, January 2003.

[44] Liu, J. Z., Wu, X. R., Ding, C. F., Hu, B. R., Wang, L. F., Annigeri, B., Vestergaard, L. H., Romanowski, A., Scheider, G. J., and Forth, S. C., "Crack Growth Behavior and Fatigue-Life Prediction Based on Worst-Case Near-Threshold Data of a Large Crack for 9310 Steel," *Fatigue and Fracture of Engineering Materials and Structures*, Vol. 25, 2002, pp. 467–480.

[45] Newman, Jr., J. C., *A Crack-Closure Model for Predicting Fatigue Crack Growth under Aircraft Spectrum Loading*, ASTM STP 748, Philadelphia, PA, 1981, pp. 53–84.

[46] Newman, Jr., J. C., *Prediction of Fatigue Crack Growth under Variable-Amplitude and Spectrum Loading*, ASTM STP 761, Philadelphia, PA, 1982, pp. 255–277.

[47] Newman, Jr., J. C., *FASTRAN – A Fatigue Crack Growth Life-Prediction Code Based on the Crack-Closure Concept, Version 5.3*, Southwest Research Institute, September 2009.

[48] Newman, Jr., J. C., *Fracture Analysis of Various Cracked Configurations in Sheet and Plate Materials*, ASTM STP 605, Philadelphia, PA, 1981, pp. 104–123.

[49] Ziegler, B., Yamada, Y., and Newman, Jr., J. C., "Crack Growth Predictions Using a Strip-yield Model for Variable-amplitude and Spectrum Loaidng," *Materialwissenschaft und Werkstofftechnik*, Vol. 39, No. 10, October 2008.

[50] Yamada, Y., *Experimental Investigations on Near Threshold Events on Fatigue Crack Growth*, Ph.D. thesis, Mississippi State University, Mississippi State, Mississippi, December 2009.

[51] Yamada, Y., Newman, III, J. C., and Newman, Jr., J. C., "Elastic-Plastic Finite-Element Analyses of Compression Precracking and Its Influence on Subsequent Fatigue-Crack Growth," *Journal of ASTM International*, Vol. 5, No. 8, 2008.

[52] Elber, W., *The Significance of Fatigue Crack Closure*, ASTM STP 486, 1971, pp. 230–242.

[53] Newman Jr., J. C., "A Crack Opening Stress Equation for Fatigue Crack Growth," *International Journal of Fatigue*, Vol. 24, 1984, pp. R131–R135.

[54] Newman, Jr., J. C., "FASTRAN-II — A Fatigue Crack Growth Structural Analysis Program," NASA TM 104159, 1992.

[55] Newman, Jr., J. C., *Effects of Constraint on Crack Growth under Aircraft Spectrum Loading*, Delft University Press, 1992, pp. 83–109.

[56] McClung, R. C., "Finite-Element Analysis of Specimen Geometry Effects on Fatigue Crack Closure," *Fatigue and Fracture of Engineering Materials and Structures*, Vol. 17, 1994, pp. 861–872.

[57] Schijve, J., *Significance of Fatigue Cracks in Micro-Range and Macro-Range*, ASTM STP 415, Philadelphia, PA, 1967, pp. 415–459.

[58] Newman, Jr., J. C., *Fracture Analysis of Various Cracked Configurations in Sheet and Plate Materials*, ASTM STP 605, Philadelphia, PA, 1976, pp. 104–123.

[59] Newman, Jr., J. C., Wu, X. R., Venneri, S. L., and Li, C. G., "Small-Crack Effects in High-Strength Aluminum Alloys," NASA Reference Publication 1309, NASA/CAE Cooperative Program, May 1994.

[60] Tada, H., Paris, P. C., and Irwin, G. R., *The Stress Analysis of Cracks Handbook*, The American Society of Mechanical Engineers, 3rd ed., 2000, p. 52.

[61] Newman, Jr., J. C., Wu, X. R., Venneri, S. L., and Li, C. G., "Small-Crack Effects in High-Strength Aluminum Alloys," *NASA Reference Publication 1309*, May 1994.

[62] *NASGRO Reference Manual (version 4.02)*, Southwest Research Institute and NASA Johnson Space Center, 2002.

[63] Skorupa, M., Machniewicz, T., Schijve, J., and Skorupa, A., "Application of the Strip-Yield Model from the NASGRO Software to Predict Fatigue Crack Growth in Aluminum Alloys under Constant and Variable Amplitude Loading," *Engineering Fracture Mechanics*, Vol. 74, 2007, pp. 291–313.

[64] Newman, Jr., J. C. and Dawicke, D. S., "Prediction of Fatigue Crack Growth in a High-Strength Aluminum Alloy under Variable-Amplitude Loading," *Advances in Fracture Research*, ICF-7, 1989, pp. 945–952.

[65] Newman, Jr., J. C., "Prediction of Crack Growth under Variable-Amplitude Loading in Various Materials," *International Conference on Engineering Against Fatigue*, Sheffield, United Kingdom, 1997, pp. 261–268.

[66] Schijve, J., "Lips on Fatigue Fractures in Aluminum Sheet Material," *Engineering Fracture Mechanics*, Vol. 14, 1981, pp. 789–800.

[67] Newman, Jr., J. C., Schneider, J., Daniel, A., and McKnight, D., "Compression Pre-cracking to Generate near Threshold Fatigue-Crack-Growth Rates in Two Aluminum Alloys, International Journal of Fatigue," *International Journal of Fatigue*, Vol. 27, 2005, pp. 1432–1440.

[68] Ruschau, J. J. and Newman, Jr., J. C., "Compression Precracking to Generate Near Threshold Fatigue-Crack-Growth Rates in an Aluminum and Titanium Alloy," *Journal of ASTM International*, Vol. 5, No. 7, 2008.

[69] Newman, Jr., J. C. and Yamada, Y., "Compression Precracking Methods to Generate Near-Threshold Fatigue-Crack-Growth-Rate Data," *International Journal of Fatigue*, Vol. 32, 2010, pp. 879–885.

[70] Barter, S. A., Sharp, P. K., Holden, G., and Clark, G., "Iniation and Early Growth of Fatigue Cracks in an Aerospace Aluminum Alloy," *Fatigue and Fracture of Engineering Materials and Structures*, Vol. 25, 2002, pp. 111–125.

[71] Johnston, W., Personal Communication, NASA Langley Research Center, Hampton, VA, 2008.

[72] Piascik, R. S. and Newman, Jr., J. C., "An Extended Compact Tension Specimen for Fatigue Crack Growth and Fracture Testing," *International Journal of Fracture*, Vol. 76, 1996, pp. R43–R48.

[73] McKeighan, P. C., Feiger, J. H., and Riddell, W. T., "Fatigue Crack Growth Rate Behavior of the Tank Car Steel TC-128B," *Iron & Steelmaker*, Vol. 2, No. 5, May 2002, pp. 73–78.